ANALYTICAL AND EXPERIMENTAL STUDY
OF STRATIFICATION AND LIQUID-ULLAGE COUPLING

Prepared for

NATIONAL AERONAUTICS AND SPACE ADMINISTRATION

GEORGE C. MARSHALL SPACE FLIGHT CENTER

Huntsville, Alabama

N67 13109

(ACCESSION NUMBER)

_156_
(PAGES)

CR-80478
(NASA CR OR TMX OR AD NUMBER)

(THRU)

/
(CODE)

33
(CATEGORY)

FACILITY FORM 602

Lockheed

MISSILES & SPACE COMPANY

A GROUP DIVISION OF LOCKHEED AIRCRAFT CORPORATION

SUNNYVALE, CALIFORNIA

ANALYTICAL AND EXPERIMENTAL STUDY OF STRATIFICATION AND LIQUID-ULLAGE COUPLING

Contributors

J. H. Chin
E. Y. Harper
F. L. Hines
S. E. Hurd
G. C. Vliet

Contract NAS 8-11525

Approved: *A. M. Levy*
A. M. Levy, Study Leader
Launch and Entry Thermodynamics

Approved: *A. M. Levy*
D. M. Tellep, Manager *for*
Launch and Entry Thermodynamics

FOREWORD

This report was prepared by Launch and Entry Thermodynamics of the Flight Technology — Engineering organization, Research and Development Division, Lockheed Missiles & Space Company, for the George C. Marshall Space Flight Center (MSFC) of the National Aeronautics and Space Administration (NASA).

The work was performed under NASA Contract NAS 8-11525, "Theoretical and Experimental Studies of Zero-G Heat-Transfer Modes." The contract was under the technical supervision of Gordon K. Platt and Frank E. Swalley, Fluid Mechanics and Thermodynamics Branch, Propulsion Division, Propulsion and Vehicle Engineering Laboratory, NASA/MSFC.

The report summarizes the principal results obtained during the period from 1 June 1964 through 31 May 1965.

PRECEDING PAGE BLANK NOT FILMED.

LOCKHEED MISSILES & SPACE COMPANY

CONTENTS

LOCKHEED MISSILES & SPACE COMPANY

ILLUSTRATIONS

LOCKHEED MISSILES & SPACE COMPANY

LOCKHEED MISSILES & SPACE COMPANY

TABLES

LOCKHEED MISSILES & SPACE COMPANY

NOMENCLATURE

A	area, ft^2
c_p	specific heat at constant pressure, $\text{Btu/lb}_m\,^\circ\text{R}$
c_v	specific heat at constant volume, $\text{Btu/lb}_m\,^\circ\text{R}$
Gr_H^*	modified Grashof number based on H, $g\beta q_w H^4/k\nu^2$
Gr_x^*	modified Grashof number based on x, $g\beta q_w x^4/k\nu^2$
g	local acceleration, ft/sec^2
g_c	conversion factor, $32.2\ \text{ft-lb}_m/\text{sec}^2\text{-lb}_f$
H	heated liquid height, ft
H'	equivalent liquid height, ft
h	heat transfer coefficient, $\text{Btu/ft}^2\text{-sec-}^\circ\text{F}$; enthalpy, Btu/lb_m
h_L	liquid film heat transfer coefficient, $\text{Btu/ft}^2\text{-sec-}^\circ\text{F}$
h_v	vapor film heat transfer coefficient, $\text{Btu/ft}^2\text{-sec-}^\circ\text{F}$
I	energy integral, $\displaystyle\int_0^1 \left(\frac{T-T_0}{T_S-T_0}\right) d\left(\frac{z}{\Delta}\right)$
I^*	energy integral, $\displaystyle\int_0^1 \left(\frac{T-T_B}{T_S-T_B}\right) d\left(\frac{z}{\Delta_2}\right)$
J	mechanical equivalent of heat, $778\ \text{ft-lb}_f/\text{Btu}$
k	thermal conductivity, $\text{Btu/ft-sec-}^\circ\text{F}$
L	ullage height, ft
ℓ	initial half-width of free jet, ft
M	mass, lb_m
M_v	vapor mass per unit area, lb_m/ft^2
ΔM_v	change in ullage mass, lb_m
$\dot{m}$	mass transfer rate per unit area, $\text{lb}_m/\text{ft}^2\text{-sec}$
$\dot{m}_{BL}$	boundary layer mass flow rate, $\text{lb}_m/\text{ft-sec}$
$\dot{m}_p$	ullage vapor mass flow rate, $\text{lb}_m/\text{ft}^2\text{-sec}$
p	pressure, lb_f/ft^2
ΔP	change in pressure, psi
Pr	Prandtl number, $\mu c_p/k$
Q	total heat transfer, Btu

$\dot{Q}$	total heat rate, Btu/sec
q	heat added per unit mass, Btu/lb$_m$
q_B	bottom heat flux, Btu/ft^2-sec
q'_B	equivalent bottom heat flux, Btu/ft^2-sec
q_L	heat flux to interface from liquid film, Btu/ft^2-sec
q_u	heat flux to ullage, Btu/ft^2-sec
q_v	heat flux to vapor film from interface, Btu/ft^2-sec
q_{vap}	vaporization heat flux, Btu/ft^2-sec
q_w	sidewall heat flux to liquid, Btu/ft^2-sec
R	tank radius, ft
$\mathcal{R}$	gas constant, Btu/lb$_m$ °R
Ra^*_H	modified Rayleigh number based on H, Gr^*_H Pr
Ra^*_x	modified Rayleigh number based on x, Gr^*_x Pr
S	defined in Eq. (3.15)
T	temperature, °F, °R
ΔT	change in temperature, °F
ΔT_{crit}	superheat required for nucleate boiling inception at wall, $T_w - T_{sat}$, °R
t	time, sec
t_s	time for stratified layer to reach steady state, sec
u	boundary-layer velocity, ft/sec
u_1	characteristic boundary-layer velocity, ft/sec
u_{ave}	average boundary-layer liquid velocity, ft/sec
u_c	centerline velocity of free jet, ft/sec
u_s	source velocity of free jet, ft/sec
u^*	slip velocity, u_v/u_L
V	volume, ft^3
v	specific volume, ft^3/lb$_m$
X	axial height, in.
x	coordinate parallel to tank wall, measured from start of boundary layer
y	coordinate perpendicular to tank wall, measured from tank wall
z	coordinate parallel to tank wall, measured from liquid surface
α	vapor fraction; quantity defined by Eq. (2.7) or Eq. (7.14)
$\overline{\alpha}$	average vapor fraction

α_0 defined by Eq. (6.4)

β coefficient of volumetric expansion, $1/°R$

Δ stratified layer thickness, ft

Δ_1 mass stratified layer thickness, ft

Δ_2 thermal stratified layer thickness, ft

Δ_{2-s} steady state stratified layer thickness, ft

δ boundary-layer thickness, ft

δ_L liquid film thickness, ft

δ_v vapor film thickness, ft

ζ azimuth angle, radians

θ temperature difference between point in boundary layer and bulk liquid outside boundary layer, $°F$

θ_S temperature difference across boundary layer, $°F$

λ latent heat of vaporization, Btu/lb_m

μ dynamic viscosity, $lb_m/ft\text{-}sec$

ν kinematic viscosity, ft^2/sec

ρ density, lb_m/ft^3

ρ^* density ratio, ρ_v/ρ_L

σ constant in Eq. (3.10)

τ_0 difference between vapor and liquid specific internal energy at absolute zero temperature, Btu/lb_m

τ_w wall shear stress, lb_f/ft^2

ϕ_H dimensionless time, $\nu t/H^2$

ϕ_{Ha} dimensionless time at which mass stratified layer reaches tank bottom, $\nu t_a/H^2$

ψ defined by Eq. (2.19)

Subscripts

B bottom

b boiling

c free-convection

f interface

g ullage gas

L liquid

m at time t_m

N	surface layer, n = N
n	layer n
0	initial
p	constant pressure
R	center of liquid surface
S	liquid surface
sat	saturation
T	constant temperature
TR	transitional
u	ullage
v	vapor
w	liquid sidewall
∞	bulk liquid

Section 1
INTRODUCTION AND SUMMARY

Stratification is defined as the development of temperature gradients in a contained fluid as a result of external heating. Stratification occurs because the free-convection boundary layer at the wall carries the heated fluid to the top of a container (e. g. , a propellant tank) forming a growing layer of stratified liquid which is at a higher temperature than the bulk of the tank's contents. If the liquid is near saturation, mass and energy transfer may occur at the liquid-vapor interface and can influence the pressure and temperature in the ullage.

These phenomena are of particular importance in cryogenic propellant tanks and may have a significant effect on vehicle design and operation. Specifically, the design of venting devices, pressurization systems, insulation methods, propellant feed pumps, and tank structures may be substantially influenced by these phenomena. In order to ensure reliable designs, and to avoid excessive penalties due to conservatism in prediction methods, a sound analytical model and experimental data applicable to the conditions of interest are required.

This document presents the results of the analytical and experimental work carried out by the Lockheed Missiles & Space Company (LMSC) for the NASA-George C. Marshall Space Flight Center on the problem of propellant stratification and liquid-ullage coupling, under Phase II of a contract entitled "Theoretical and Experimental Studies of Zero-G Heat Transfer Modes." The work reported was conducted over a 12-month period. The results of Phase I of the study were reported in Ref. 1.

The major objective of the study has been to perform theoretical analyses of the heat-transfer phenomena occurring in cryogenic liquids and to derive an analytical model for predicting temperature stratification and ullage pressure in cryogenic tanks. An auxiliary objective has been to conduct stratification experiments in noncryogenic

fluids to demonstrate the validity of scaling laws for stratification and to check the analytical models developed.

The highlights of Phase II of the study are summarized below.

1.1 STRATIFICATION ANALYSES

Theoretical work carried out during Phase I of the study resulted in a closed-form solution for predicting stratification of subcooled fluids in cylindrical containers sub-jected to uniform sidewall heating. This solution has been extended to consider com-bined uniform sidewall and bottom heating as well as asymmetric sidewall heating with or without bottom heating. The closed-form solution is based on the assumption of time-invariant dimensionless temperature profiles in the thermal stratified layer.

For stratification in a liquid near saturation, an analytical model has been developed which includes the coupling between liquid and ullage vapor. The model is based on the closed-form solution for subcooled stratification but considers mass and energy transfer at the liquid-vapor interface. A computer program has been written which solves the basic equations to give the ullage pressure and temperature and the liquid temperatures. The program incorporates options for self-pressurization or several modes of venting in the ullage.

The effect of nucleate boiling at the wall on stratification has also been investigated. A solution was obtained for a boiling free-convection boundary layer on a vertical flat plate based on a continuum analysis utilizing integral boundary layer equations. The results of the boundary layer solution were then used in the stratification pre-diction.

1.2 STRATIFICATION EXPERIMENTS

In Phase I of the study, stratification experiments with uniform sidewall heating were conducted in three different vessels with six different noncryogenic fluids.

1-2

These experiments demonstrated the utility and applicability of noncryogenic experiments in the study of propellant stratification. Additional experiments have been conducted in Phase II with combined uniform sidewall and bottom heating. The experimental results verified the predictions based on the analytic solution.

The experiments demonstrated that the dimensionless temperature profiles in the stratified layer were also time-invariant with bottom heating. The shape of the dimensionless temperature profile determines a parameter defined as the energy integral which is a key quantity in the analytic solution for predicting temperature stratification. The values of the energy integral with uniform sidewall and bottom heating were in agreement with the correlation established in Phase I with the data for uniform sidewall heating alone. For modified Grashof numbers greater than 10^{13}, some effect of bottom heating on the energy integral was indicated.

Stratification experiments with asymmetric sidewall heating and with and without bottom heating were also conducted. Radially uniform temperatures were obtained in the stratified layer, and the data were in very good agreement with the predictions. The asymmetric sidewall heating had no influence on the values of the energy integral.

All the stratification data and the correlation of the energy integral with modified Grashof number were obtained with an aspect ratio of 2.3 (ratio of liquid height to tank radius). In order to determine the effect of aspect ratio, stratification data were obtained with an aspect ratio of 4.7. No effect of aspect ratio on the energy integral or on the agreement between predictions and experimental data was apparent.

An experimental program to study stratification with liquid-ullage coupling was initiated. The limited data obtained to date support the approach used in the liquid-ullage coupling model.

Data on a boiling free-convection boundary layer were obtained in experiments with water. The results confirmed the increased mass flow rate with boiling predicted by the boundary-layer solution. Data from preliminary stratification experiments with a boiling boundary layer were in good agreement with the prediction.

1.3 CORRELATION OF CRYOGENIC STRATIFICATION DATA

The analytical techniques developed in the present study for predicting stratification have been used to correlate stratification data from four different series of liquid hydrogen tests conducted in tanks ranging from 40 in. in diameter to a full-scale S-IV tank. By means of mass and energy balances, the validity and repeatability of the heat flux boundary conditions were evaluated. Considering the uncertainties in the boundary conditions and in the determination of the inception of nucleate boiling, good correlation was obtained between the stratification analysis and the cryogenic data.

1.4 FUTURE WORK

In the continuation of the present study, effort will be devoted to an experimental program to obtain stratification data with liquid-ullage coupling. Venting, self-pressurization, and active pressurization will be included in the program. The experimental results will be used to establish the validity of the analytic model and to correlate the various parameters to enable general application of the model.

Experiments will also be conducted with boundary conditions resulting in nucleate boiling at the wall. The data will be compared to the analytical predictions of boiling effects.

An analytical and experimental investigation will also be conducted of the possible breakthrough at the liquid surface under low axial acceleration of the free-convection boundary layer developed at the wall. The analytical investigation will utilize a computer program developed during Phase I of the study for predicting the liquid surface configuration with surface velocity. The experimental program will be conducted in the LMSC drop-tower facility.

Section 2

STRATIFICATION WITH UNIFORM SIDEWALL AND BOTTOM HEATING

The method for predicting subcooled liquid stratification in a cylindrical tank with sidewall heating only, developed during the previous Phase of the study (Ref. 1), has been extended to the case of a cylindrical tank with both sidewall and bottom heating. In this section, the extended analysis, also based on an integral technique, will be outlined. Experiments to verify the analysis have been conducted with noncryogenic fluids using a facility and techniques previously established (Ref. 1). The results from these experiments will be presented and compared to the analytical predictions.

2.1 ANALYSIS

Two analytical models have been postulated to describe stratification with both side-wall and bottom heating. The geometry used for these models is shown in Fig. 2-1. A cylindrical tank is assumed to accelerate along its longitudinal axis as the liquid is subjected to uniform and time-independent sidewall and bottom heat fluxes. For a subcooled liquid, the energy transfer at the free surface is negligible. As shown in Fig. 2-1, two stratified layers are defined for the case with bottom heating. The mass stratified layer, designated by $\Delta_1(t)$, contains a mass of liquid equivalent to that which has passed through the free-convection boundary layer at the wall. The thermal stratified layer, designated by $\Delta_2(t)$, is the portion of liquid in the mass stratified layer which extends from the liquid surface to the location at which the temperature becomes uniform. In the thermal stratified layer, the temperatures are independent of radial and azimuthal location. With sidewall heating only, the thermal and mass stratified layers are identical.

2.1.1 Model I

The first analytical model considered is based on the following additional assumptions:

LOCKHEED MISSILES & SPACE COMPANY
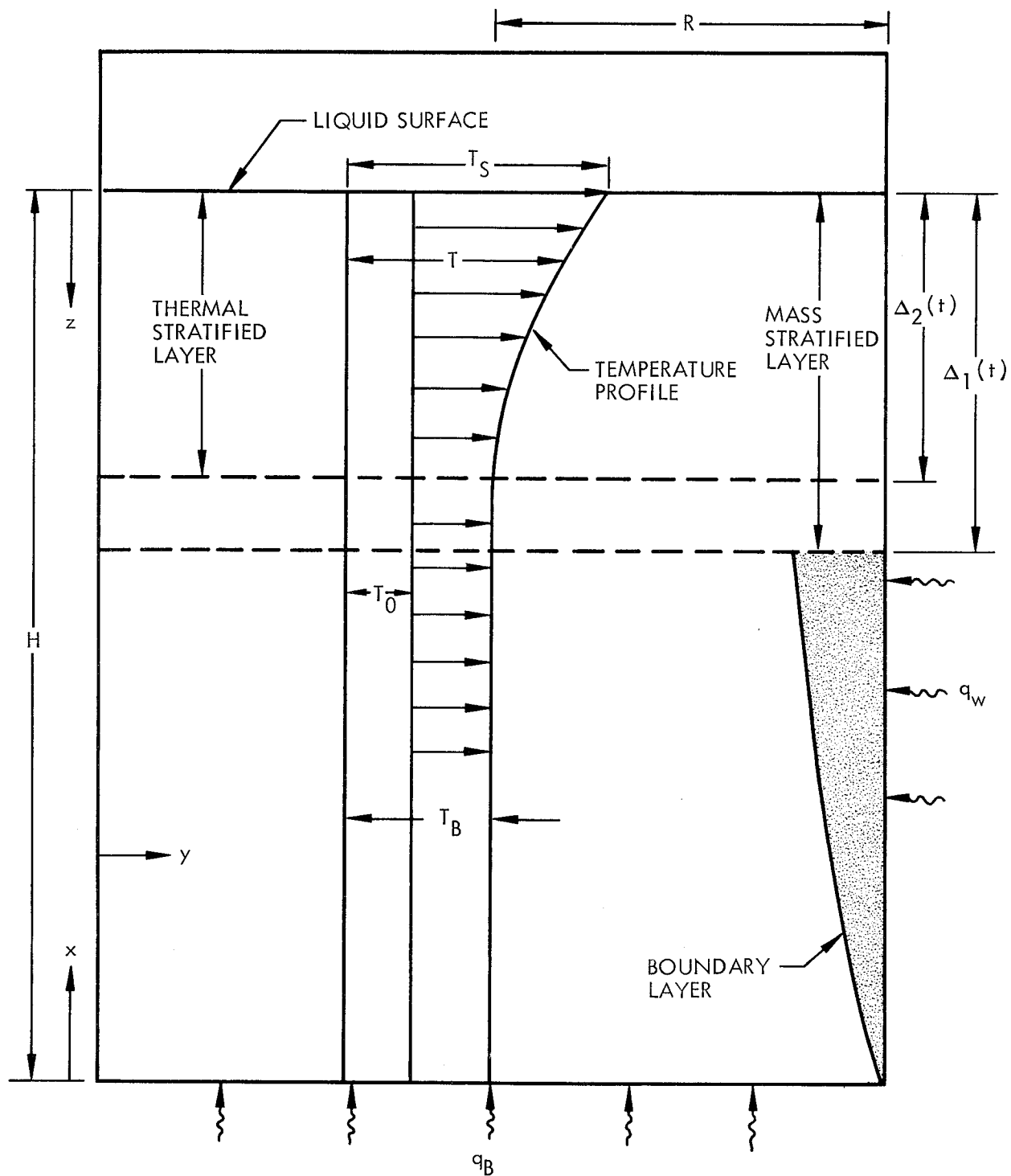
Fig. 2-1 Geometry Used for Analysis of Stratification With
Sidewall and Bottom Heating

- The boundary-layer development on the wall with sidewall and bottom heating is the same as with sidewall heating alone.

- The surface temperature rise is the same as that with sidewall heating alone.

- All the energy which enters through the bottom remains in the fluid below the thermal stratified layer and uniformly increases the bottom temperature T_B.

- The temperature profiles in the thermal stratified layer are similar (i.e., dimensionless temperature profiles are time-invariant). The value of the energy integral based on the thermal stratified layer,

$$I^* \equiv \int_0^1 \left[(T - T_B)/(T_S - T_B) \right] d\left(z/\Delta_2 (t) \right)$$

is the same as that based on the mass stratified layer

$$I \equiv \int_0^1 \left[(T - T_0)/(T_S - T_0) \right] d\left(z/\Delta(t) \right)$$

in the absence of bottom heating.

- When the bottom temperature exceeds the surface temperature, the temperature profiles become uniformly mixed.

The depth of the mass stratified layer $\Delta_1(t)$, and the surface temperature rise T_S, are determined from the stratification prediction for sidewall heating only (Ref. 1). The two new unknowns are the bottom temperature T_B, and the depth of the thermal stratified layer $\Delta_2(t)$. Two energy balances can be made. From an overall energy balance

$$\frac{1}{\rho c_p} \left(q_B + 2 \frac{H}{R} q_w \right) t = (T_B - T_0) H + (T_S - T_B) I^* \Delta_2 (t) \qquad (2.1)$$

From an energy balance on the fluid below the thermal stratified layer

$$\frac{q_B t}{\rho c_p} = (T_B - T_0) [H - \Delta_2 (t)] \qquad (2.2)$$

2-3

Combining Eqs. (2.1) and (2.2) an expression for $\Delta_2(t)$ in terms of $(T_S - T_0)$ is obtained:

$$\frac{\Delta_2(t)}{H} = \frac{1}{2} + \frac{\left[(1-I)\left(\frac{q_B H}{k}\right) + 2\left(\frac{H}{R}\right)\left(\frac{q_w H}{k}\right)\right]\phi_H}{2I\,Pr\,(T_S - T_0)}$$

$$- \left\{\left[\frac{1}{2} + \frac{\left[(1-I)\left(\frac{q_B H}{k}\right) + 2\left(\frac{H}{R}\right)\left(\frac{q_w H}{k}\right)\right]\phi_H}{2I\,Pr\,(T_S - T_0)}\right]^2 - \frac{2\left(\frac{H}{R}\right)\left(\frac{q_w H}{k}\right)\phi_H}{I\,Pr\,(T_S - T_0)}\right\}^{1/2}$$

$$(2.3)$$

For times before the mass stratified layer has reached the tank bottom, the surface temperature rise from Ref. 1 is given by

$$\frac{T_S - T_0}{\frac{q_w H}{k}} = \frac{2\left(\frac{H}{R}\right)\phi_H}{I\,Pr\,\frac{\Delta_1(t)}{H}} \qquad (2.4)$$

or

$$T_S - T_0 = \frac{2\left(\frac{H}{R}\right)q_w t}{\rho c_p I\Delta_1(t)} \qquad (2.5)$$

where an appropriate expression for $\Delta_1(t)$ is used, depending on whether the boundary layer is laminar or turbulent (Ref. 1).

Substituting Eq. (2.5) in Eq. (2.3) yields

$$\frac{\Delta_2(t)}{H} = \frac{1}{2}\left\{1 + \alpha\frac{\Delta_1(t)}{H} - \sqrt{\left[1 + \alpha\frac{\Delta_1(t)}{H}\right]^2 - \frac{4\Delta_1(t)}{H}}\right\} \qquad (2.6)$$

where

$$\alpha = 1 + \frac{q_B (1 - I)}{2 q_w (H/R)} \qquad (2.7)$$

Once $\Delta_2 (t)$ is known, the bottom temperature is obtained from Eq. (2.2), or its dimensionless form

$$\frac{T_B - T_0}{(q_B H)/k} = \frac{\phi_H}{Pr \left[1 - \dfrac{\Delta_2 (t)}{H} \right]} \qquad (2.8)$$

The time at which the mass stratified layer reaches the tank bottom (from Ref. 1) is given by

$$\phi_{H_a} \bigg|_{Laminar} = 1.59 \frac{Pr^{0.388}}{(H/R) \left(Gr_H^* \right)^{1/5}} \qquad (2.9)$$

$$\phi_{H_a} \bigg|_{Turbulent} = \frac{5.75 \, Pr^{2/3}}{(H/R)} \left(\frac{1 + 0.443 \, Pr^{2/3}}{Gr_H^*} \right)^{2/7} \qquad (2.10)$$

For subsequent times, an empirical correlation (Ref. 1) is used to obtain the surface temperature rise. For a laminar boundary layer

$$\frac{T_S - T_0}{(q_w H)/k} = 2 \left(\frac{H}{R} \right) \frac{\phi_H}{Pr} + \frac{3.18 (1 - I)}{I \left(Gr_H^* \right)^{1/5} Pr^{0.612}} \qquad (2.11)$$

and for a turbulent boundary layer

$$\frac{T_S - T_0}{(q_w H)/k} = 2 \left(\frac{H}{R} \right) \frac{\phi_H}{Pr} + \frac{11.50}{Pr^{1/3}} \left(\frac{1 + 0.443 \, Pr^{2/3}}{Gr_H^*} \right)^{2/7} \left(\frac{1 - I}{I} \right) \qquad (2.12)$$

2-5

Either Eq. (2.11) or (2.12) is used with Eqs. (2.3) and (2.2) to obtain appropriate values for $\Delta_2(t)$ and T_B for times after the mass stratified layer has reached the tank bottom.

2.1.2 Model II

In order to provide an upper bound on the surface temperature rise, a second analytical model was developed to describe stratification with sidewall and bottom heating. With this model the maximum possible contribution of bottom heating to the energy in the thermal stratified layer is obtained. In addition to assumptions 1, 4, and 5 used for the first model, the following assumptions describe the second model:

- The thermal stratified layer reaches a steady state depth, Δ_{2-s}, at a finite time t_s.
- For times less than t_s (unsteady phase), the thermal and mass stratified layer depths are equal.
- The surface temperature and its derivative with respect to time are continuous functions of time.

During the unsteady phase, energy balances on the stratified layer and the unstratified portion of the liquid give

$$\frac{T_S - T_0}{(q_w H)/k} = \frac{T_B - T_0}{(q_w H)/k} + \frac{2(H/R)\phi_H}{I^* \, Pr(\Delta(t)/H)} \qquad (2.13)$$

and

$$\frac{T_B - T_0}{(q_w H)/k} = \frac{\phi_H}{(q_w/q_B) \, Pr} \qquad (2.14)$$

During the steady state phase, similar energy balances yield

$$\left(\frac{dT_S}{dt}\right)_{t \geq t_s} = \frac{2Hq_w}{\rho c_p RI^* \Delta_{2-s}} - \frac{(1 - I^*)}{I^*} \frac{dT_B}{dt} \qquad (2.15)$$

and

$$\left(\frac{dT_B}{dt}\right)_{t \geq t_s} = \frac{q_B}{\rho c_p (H - \Delta_{2-s})} \qquad (2.16)$$

With a turbulent boundary layer on the sidewall, the stratified layer depth is given in Ref. 1 as

$$\frac{\Delta(t)}{H} = 1 - \left[1 + 0.0924\left(\frac{H}{R}\right) \phi_H \, Pr^{-2/3} \left(\frac{Gr_H^*}{1 + 0.443 \, Pr^{2/3}}\right)^{2/7}\right]^{-7} \qquad (2.17)$$

Then, using Eqs. (2.13) and (2.17)

$$\left(\frac{dT_S}{dt}\right)_{t = t_s} = \frac{2Hq_w}{\rho c_p RI^*} \left[\frac{\Delta_{2-s} - 7H\psi t_s \, (1 + \psi t_s)^{-8}}{\Delta_{2-s}}\right] + \frac{q_B}{\rho c_p H} \qquad (2.18)$$

where

$$\psi = 0.0924 \, Pr^{-2/3} \left[\frac{Gr_H^*}{1 + 0.443 \, Pr^{2/3}}\right]^{2/7} \left(\frac{H}{R}\right) \frac{\nu}{H^2} \qquad (2.19)$$

The time t_s at which $\Delta = \Delta_{2-s}$ is obtained from Eq. (2.17) as

$$t_s = \frac{\left(1 - \dfrac{\Delta_{2-s}}{H}\right)^{-1/7} - 1}{\psi} \tag{2.20}$$

Using assumption 3 with Eqs. (2.15), (2.18), and (2.20) yields an expression for evaluating Δ_{2-s}

$$\left(\frac{q_w}{q_B}\right)\left(\frac{H}{R}\right) = \frac{\left(\dfrac{\Delta_{2-s}}{H}\right)^2 \left[I^*\left(1 - \dfrac{\Delta_{2-s}}{H}\right) + 1 - I^*\right]}{14\left[\left(1 - \dfrac{\Delta_{2-s}}{H}\right)^2 - \left(1 - \dfrac{\Delta_{2-s}}{H}\right)^{15/7}\right]} \tag{2.21}$$

For $t > t_s$, Eqs. (2.15) and (2.16) are then integrated to give

$$\frac{T_S - T_0}{(q_w H)/k} = \frac{T_B - T_0}{(q_w H)/k} + \frac{2(H/R)\,\phi_H}{I^* \operatorname{Pr}(\Delta_{2-s}/H)} - \frac{\phi_H}{(q_w/q_B)\,I^* \operatorname{Pr}\left(1 - \dfrac{\Delta_{2-s}}{H}\right)}$$

$$+ \frac{\left(1 - \dfrac{\Delta_{2-s}}{H}\right)^{-8/7} - \left(1 - \dfrac{\Delta_{2-s}}{H}\right)^{-1}}{0.0924\,(q_w/q_B)\,\operatorname{Pr}^{1/3}\,(H/R)\,I^*\left(\dfrac{Gr_H^*}{1 + 0.443\,\operatorname{Pr}^{2/3}}\right)^{2/7}} \tag{2.22}$$

and

$$\frac{T_B - T_0}{(q_w H)/k} = \frac{\phi_H}{\operatorname{Pr}(q_w/q_B)\left(1 - \dfrac{\Delta_{2-s}}{H}\right)}$$

$$- \frac{\left(1 - \dfrac{\Delta_{2-s}}{H}\right)^{-8/7} - \left(1 - \dfrac{\Delta_{2-s}}{H}\right)^{-1} - \left(1 - \dfrac{\Delta_{2-s}}{H}\right)^{-1/7} + 1}{0.0924\,(q_w/q_B)\,\operatorname{Pr}^{1/3}\,(H/R)\left(\dfrac{Gr_H^*}{1 + 0.443\,\operatorname{Pr}^{2/3}}\right)^{2/7}} \tag{2.23}$$

2.2 EXPERIMENTS

The advantages and utility of performing experiments with noncryogenic fluids to study propellant stratification have been demonstrated with the results reported in Ref. 1. The same approach was used in the present experiments to obtain basic data on stratification in a cylindrical tank with sidewall and bottom heating and to evaluate the analytical models.

2.2.1 Facility and Experimental Procedures

Figure 2-2 illustrates the experimental facility. The tank, which is shown installed in the radiant heating facility, was a 9.75-in. diam., thin-walled (0.025 in.) cylinder. It was filled with fluid to a height of 11.3 in. to obtain an aspect ratio of 2.3. The lid and the portion of the container above the fluid level were insulated. The sidewalls and bottom of the container were heated with independently controlled arrays of tungsten-filament quartz lamps. Fluid temperatures were measured along the cylindrical axis of the tank with thermocouples mounted on a wood dowel.

Fourteen runs were made with this facility, using both water and trichloroethylene. The test conditions are summarized in Table 2-1. Bottom heat rates were determined from calibration runs with the tank subjected to bottom heating only. The sidewall heat rates were then determined by graphical integration of the temperature profiles from the tests with both sidewall and bottom heating. The values shown in Table 2-1 for modified Grashof and Prandtl numbers are based on the average fluid properties for each run. Fluid properties used in the graphical presentation of results were evaluated at the mixed mean temperature of the fluid in the thermal stratified layer.

2.2.2 Results and Comparisons to Predictions

A criterion for boundary-layer transition must be established before a prediction based on an appropriate boundary-layer analysis can be compared with the data. Transition from laminar to turbulent flow is assumed to occur at a value for the modified Rayleigh
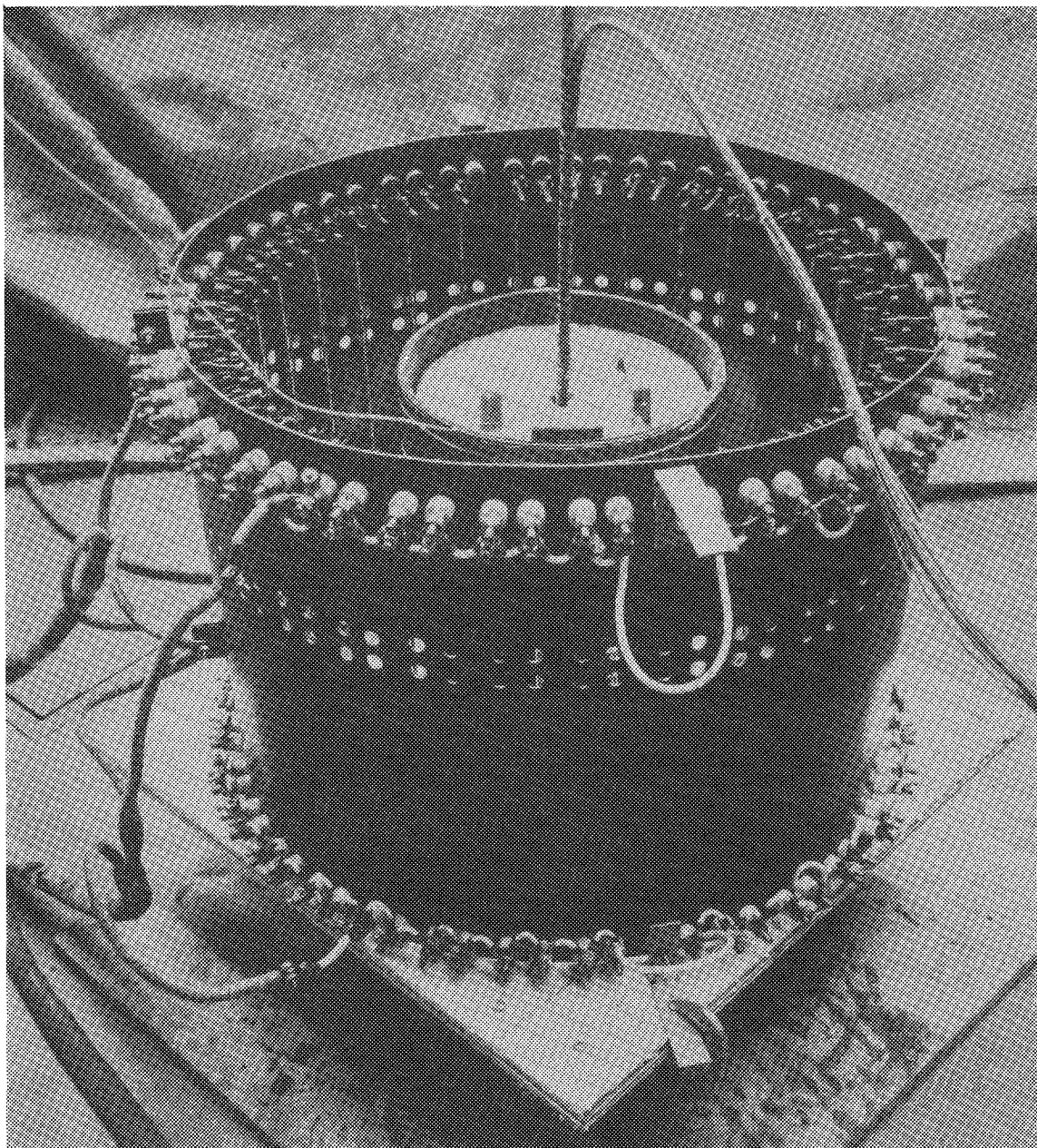
Fig. 2-2 Tank Used for Stratification Experiments —9.75-Inch-Diameter

Table 2-1

SUMMARY OF TEST CONDITIONS AND RESULTS FOR SIDEWALL AND BOTTOM HEATING STRATIFICATION EXPERIMENTS IN THE 9.75-INCH-DIAMETER TANK

(H/R = 2.3)

Run No.	Fluid	Sidewall Heat Flux q_w (Btu/ft²-sec)	Bottom Heat Flux q_B (Btu/ft²-sec)	Ratio Sidewall to Bottom Heat Flux q_w/q_B	Modified Grashof No. Gr_H^*	Prandtl No. Pr	Thermal Layer Energy Integral I*
B-1	Water	2.58	1.27	2.0	2×10^{12}	4.6	0.428
B-2	Water	1.24	0.65	1.9	1.5×10^{12}	4.3	0.400
B-3	Water	1.30	1.27	1.0	3×10^{12}	3.4	0.370
B-4	Water	2.56	2.41	1.1	2×10^{12}	4.5	0.414
B-5	Water	2.04	3.40	0.60	3×10^{12}	4.2	0.367
B-6	Water	1.38	2.41	0.57	2.4×10^{12}	3.5	0.355
105	Water	0.40	3.5	0.115	7×10^{11}	4.0	a
106	Water	0.90	3.0	0.30	2×10^{12}	3.2	0.374
107	Water	0.30	1.3	0.23	2×10^{11}	4.7	0.381
108	Trichloroethylene	2.5^c	1.3	1.9	2×10^{14}	4.1	b
109	Trichloroethylene	1.3^c	1.3	1.0	1×10^{14}	4.3	0.44
110	Trichloroethylene	2.0^c	3.5	0.57	1.6×10^{14}	4.1	b
111	Trichloroethylene	0.5^c	3.5	0.143	3×10^{13}	4.3	a
112	Trichloroethylene	1.0^c	3.0	0.33	8×10^{13}	4.2	a

[a] Uniformly mixed profiles
[b] Quality of data insufficient to determine I*
[c] Calibration value

number $(Ra_x^* = Gr_x^* \, Pr)$ of 10^{11} (Ref. 1). Data are compared with predictions based on the modified turbulent boundary layer analysis when at least half of the length of the boundary layer is turbulent, i.e., when $Ra_H^* \geq 1.6 \times 10^{12}$.

Some typical temperature profiles are compared with the predictions in Fig. 2-3. The prediction techniques are designated as Model I and Model II consistent with the discussion in Subsection 2.1. Both of these models yield values for the bottom and surface temperature rises and the thermal stratified layer depth. The profile within the thermal stratified layer is plotted by assuming a form which satisfies the boundary conditions:

$$\frac{(T - T_B)}{(T_S - T_B)} = \left(1 - \frac{z}{\Delta_2(t)}\right)^n \tag{2.24}$$

Using the definition of I^*, a value for the exponent n is obtained:

$$I^* = \int_0^1 \left(1 - \frac{z}{\Delta_2(t)}\right)^n d\left(\frac{z}{\Delta_2(t)}\right) = \frac{1}{n+1} \tag{2.25}$$

or

$$n = \frac{1 - I^*}{I^*} \tag{2.26}$$

Figure 2-3a illustrates the main difference between Model I and Model II. In Model I, there is no contribution of bottom heating to the energy increase of the fluid in the thermal stratified layer. In Model II, the maximum contribution is allowed. A comparison of the data with both models supports the assumption made in Model I that the surface temperature rise is unaffected by bottom heating. Since Model II is considerably more complicated than Model I, and generally predicts too high a surface temperature

2-12
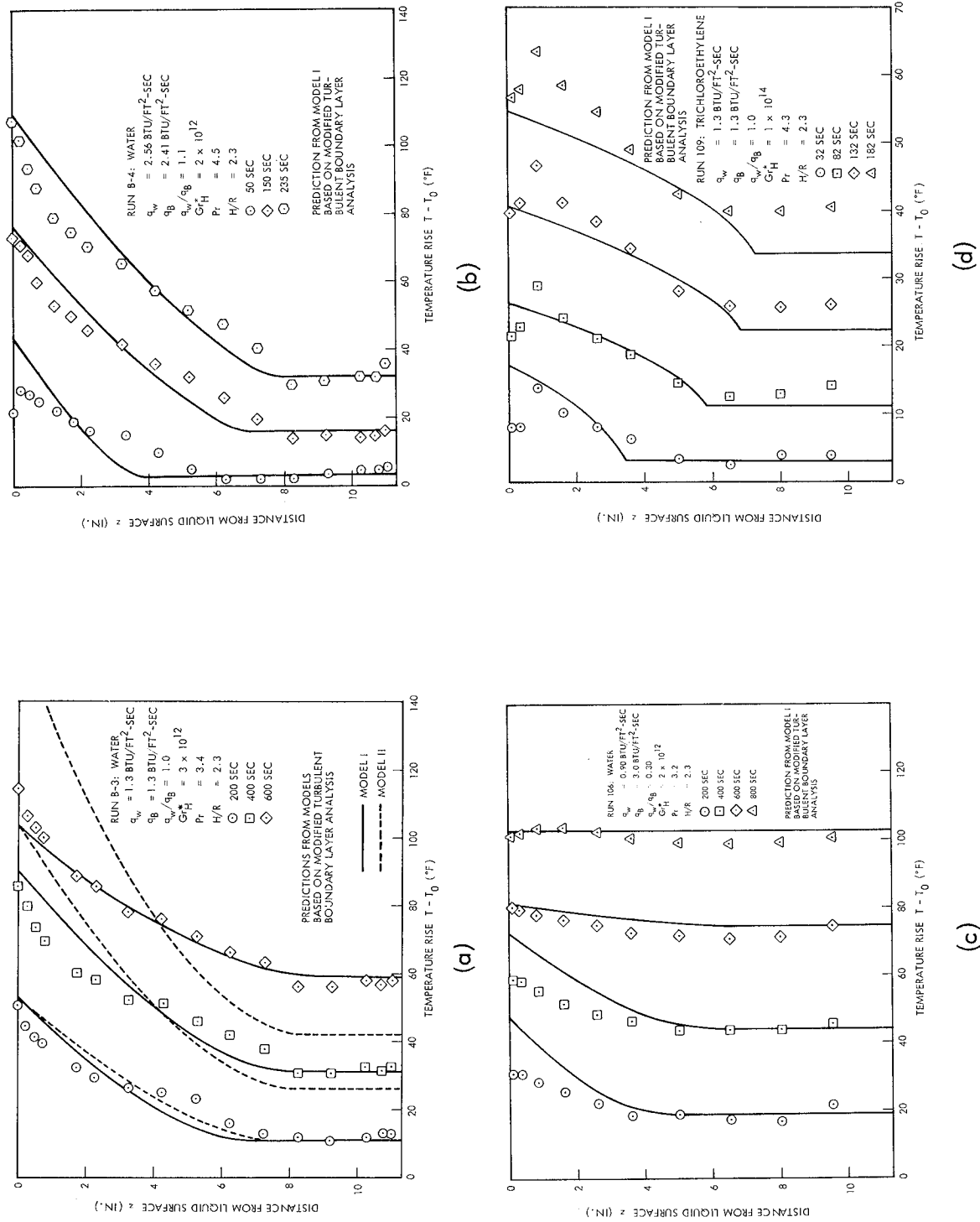
Fig. 2-3 Comparison of Experimental Data With Predictions for Stratification Temperature Profiles With Sidewall and Bottom Heating

rise and too low a bottom temperature rise, only Model I is compared with the data on the remaining figures.

The assumption made in Model I concerning the distribution of the energy which enters the bottom is verified in Fig. 2-3b when the predicted thermal stratified layer depth and bottom temperature rise are compared with the data.

Figure 2-3c shows how the temperature profiles become uniformly mixed when the bottom temperature overtakes the surface temperature. For the moderately low heat ratio shown (q_w/q_B = 0.30), the time when this occurs is predicted quite well by Model I. The profiles obtained with a very low value for the heat rate ratio (q_w/q_B = 0.115) were uniformly mixed at all times.

The results from a typical run using trichloroethylene are shown in Fig. 2-3d. In all of the runs with trichloroethylene, relatively large heat losses occurred at the liquid surface as the result of excessive evaporation. In order to obtain a prediction which would correctly represent the energy in the liquid, heat rates based on the integrated energy in the tank were used in the analysis. The evaporation at the surface caused a distortion of the temperature profiles, particularly near the surface. For this reason it was difficult to obtain values for the energy integral from the trichlorethylene data. This problem is reflected in Table 2-1 where no values for I^* are reported for Runs 108 and 110.

Figure 2-4 shows the dimensionless form of the temperature profiles presented in Fig. 2-3. These results indicate that the assumption of similar profiles in the thermal stratified layer is reasonable. The data points near the liquid surface which were greatly distorted by evaporation are not shown in Fig. 2-4d.

The energy integral values, which are obtained by graphical integration of the dimensionless profiles, are compared with those obtained with sidewall heating only in Fig. 2-5. All of the data points obtained with bottom heating using water are within
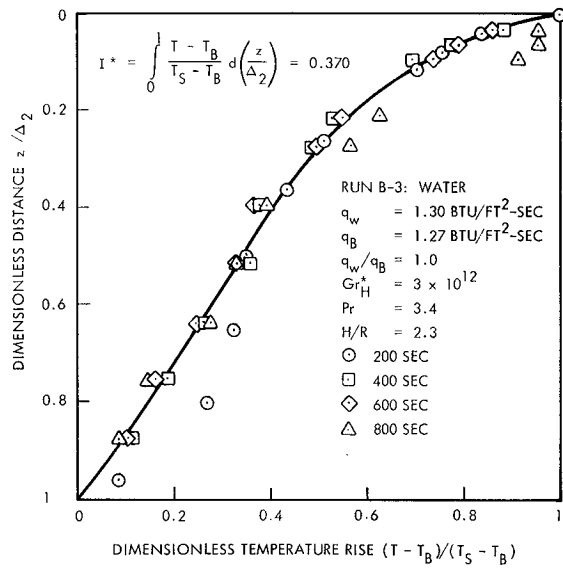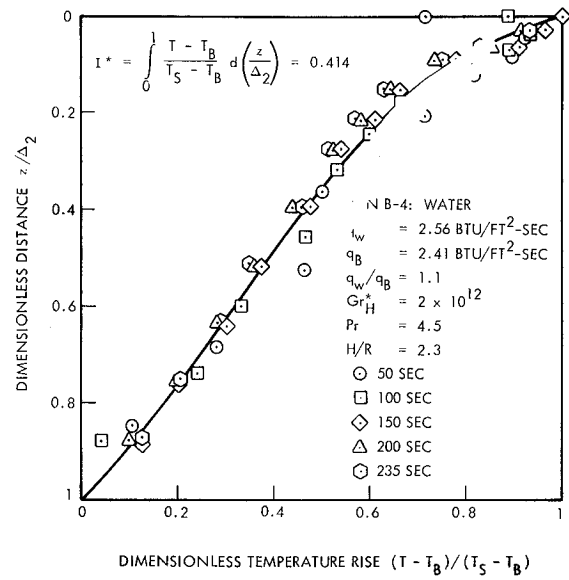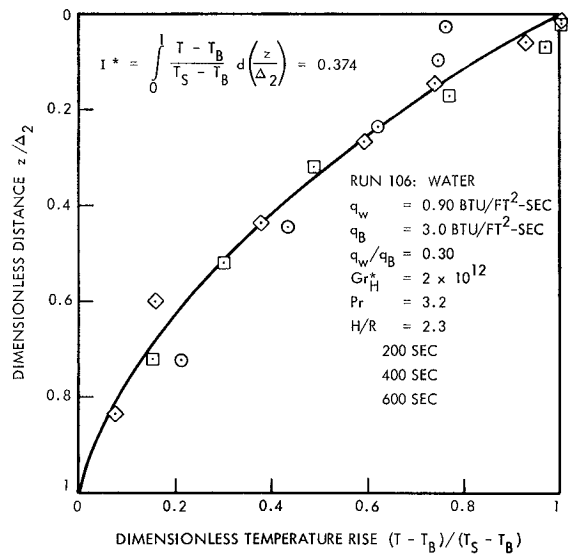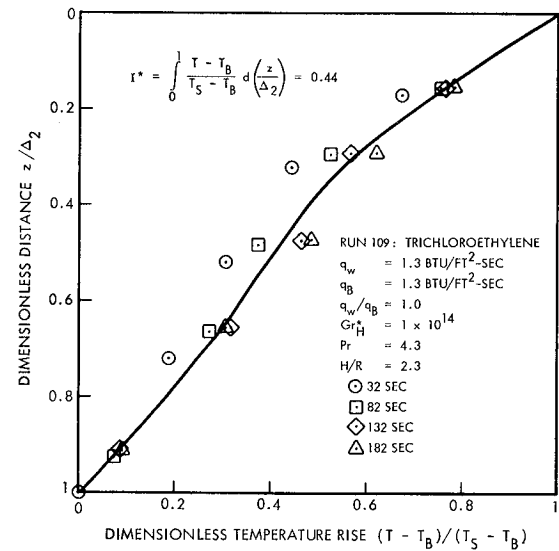
Fig. 2-4 Dimensionless Stratification Temperature Profiles With
Sidewall and Bottom Heating
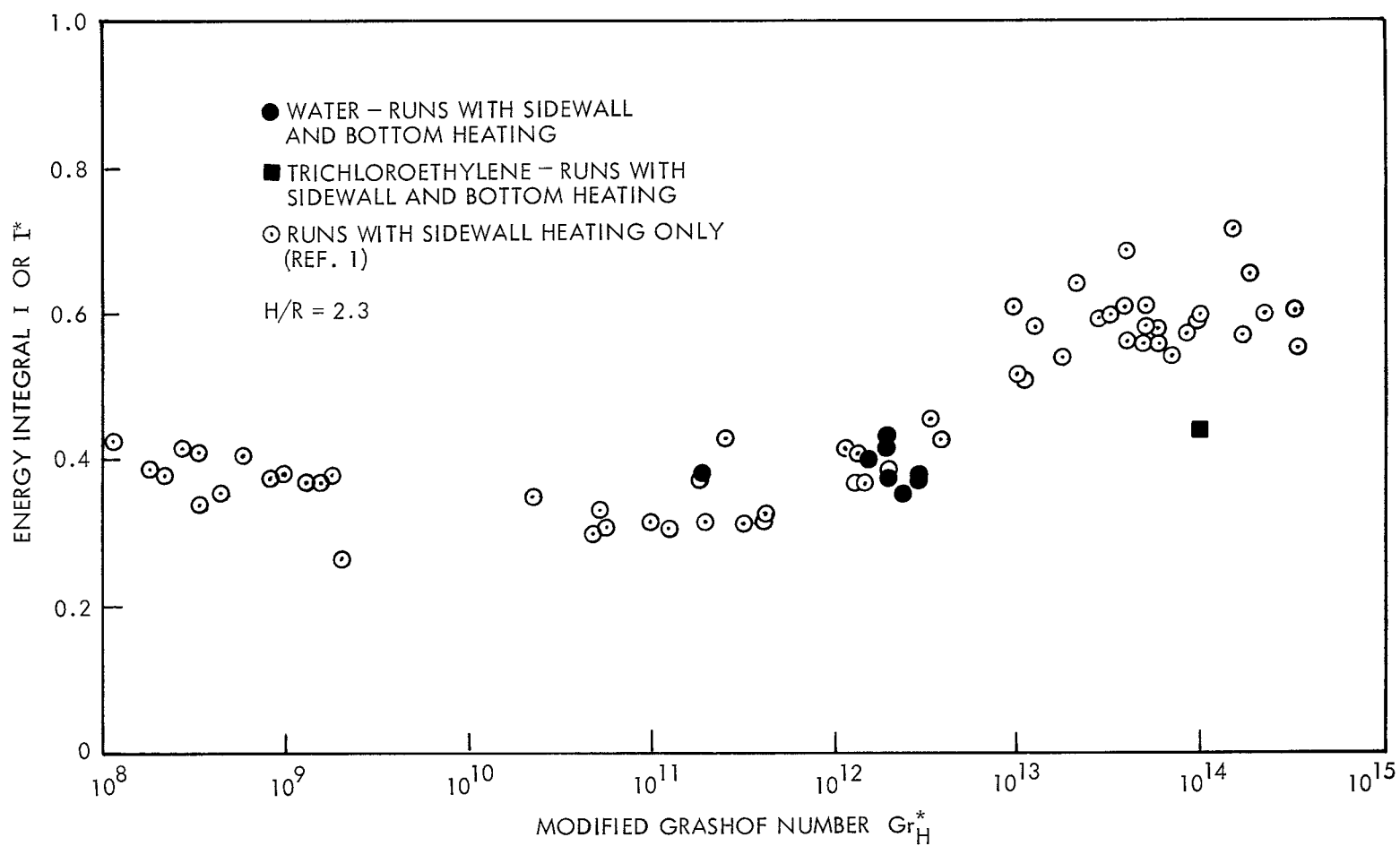
Fig. 2-5 Energy Integral as a Function of Modified Grashof Number

the range of the sidewall heating data. The one point obtained using trichloroethylene is below this range. Since the trichloroethylene temperature profiles were distorted by evaporation, it is difficult to reach a conclusion based on this one data point. However, some of the cryogenic data observed (Subsection 7.3.2) support the trend towards relatively low values for the energy integral at high modified Grashof numbers when bottom heating is significant.

The data for surface temperature rise are compared with Model I predictions in Fig. 2-6 for times before the mass stratified layer reached the tank bottom. For times after the mass stratified layer reached the tank bottom, the comparison of data with predictions is given in Fig. 2-7. Data at times for which the predicted profiles are uniformly mixed are not shown on these figures. For the trichloroethylene runs, data were not obtained after the mass stratified layer reached the tank bottom. The data with sidewall and bottom heating agree well with the predictions and thus support the assumption that the surface temperature rise is the same as with sidewall heating alone.
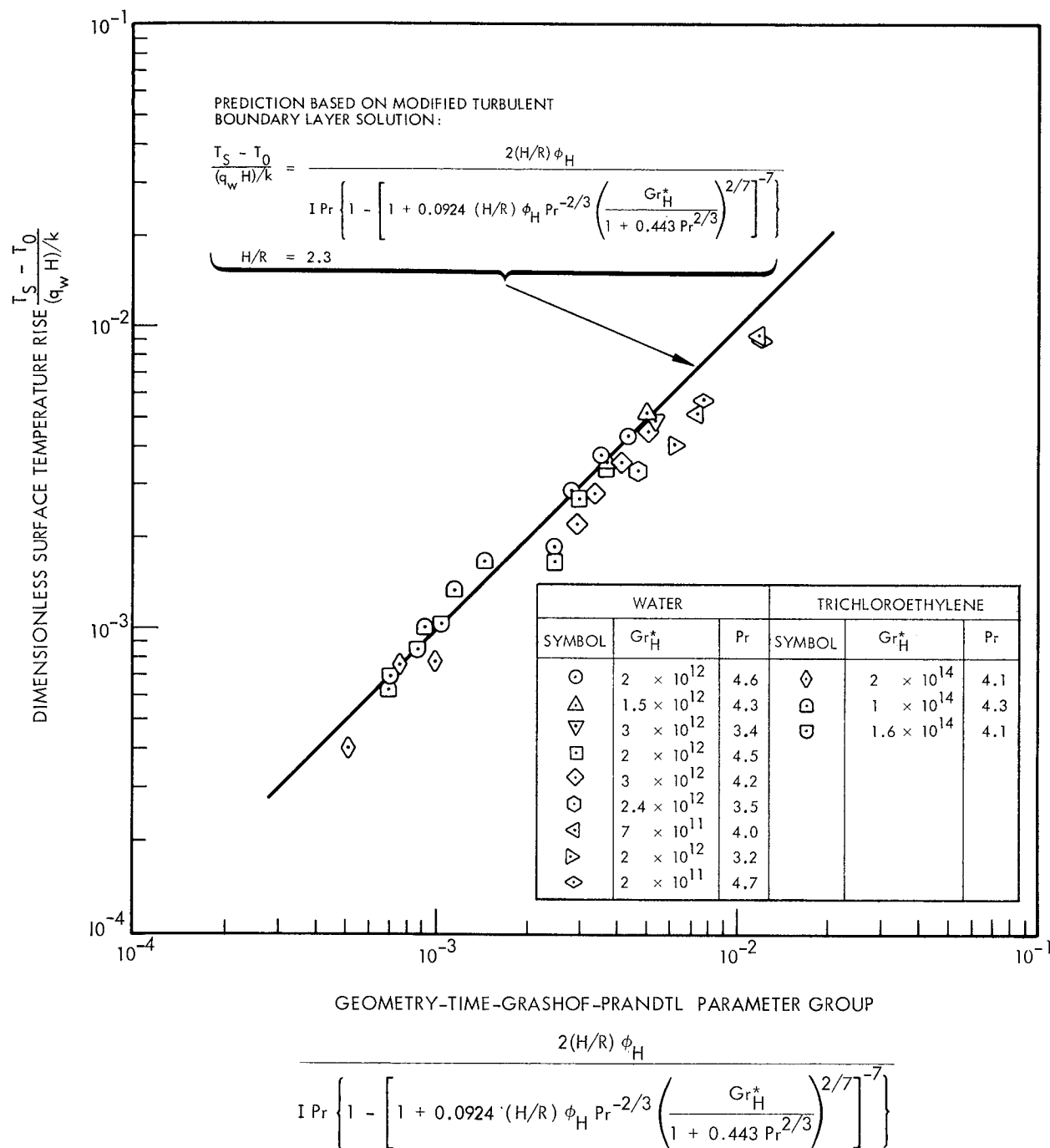
Fig. 2-6 Comparison of Experimental Data With Prediction for Surface Temperature Rise in Sidewall and Bottom Heating Stratification

2-18
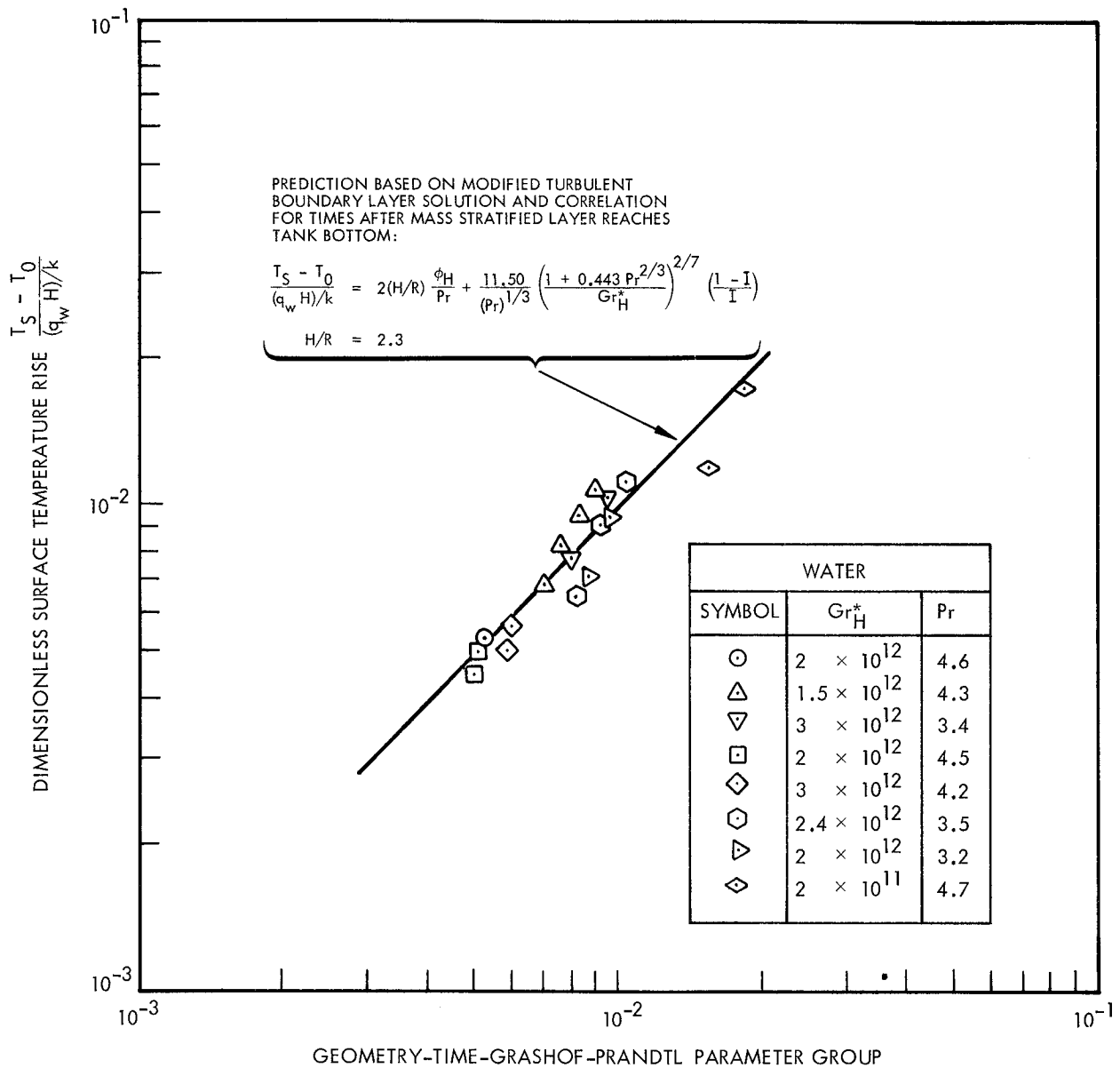
Fig. 2-7 Comparison of Experimental Data With Prediction for Surface Temperature Rise in Sidewall and Bottom Heating Stratification

2-19

Section 3

STRATIFICATION WITH ASYMMETRIC SIDEWALL HEATING

The basic analysis of Ref. 1 for stratification in a cylindrical tank with uniform sidewall heating has been extended to consider asymmetric sidewall heating boundary conditions. The analysis will be outlined in this section, and the results of experiments performed to evaluate the effects of asymmetric sidewall heating will be presented and compared with predictions. The application of the analysis to large propellant tanks will also be discussed.

3.1 ANALYSIS

To obtain expressions for the mass stratified layer growth and surface temperature rise for a general nonuniform heat rate distribution, the following assumptions were made:

- As suggested by the experimental data obtained, the surface temperature and stratified layer depth are radially uniform in spite of the asymmetric heating.
- As illustrated in Fig. 3-1, an arbitrary azimuthally varying heat-rate distribution can be approximated by a number of regions of the tank wall with uniform but different heat rates.
- The boundary layer in the various sections of uniform heating develops independently and is not affected by the boundary layer on adjacent sections.
- The energy integral I is the same as with uniform sidewall heating. It may be obtained from the experimental correlation (Ref. 1 and Fig. 2-5) using a modified Grashof number based on the integrated, average, sidewall heat rate.

A mass balance on the stratified layer yields

$$\text{Mass Change in Stratified Layer} = \sum_{n} \text{mass fluxes in boundary layer segments}$$

$$(3.1)$$

where n is a summation index over all segments.
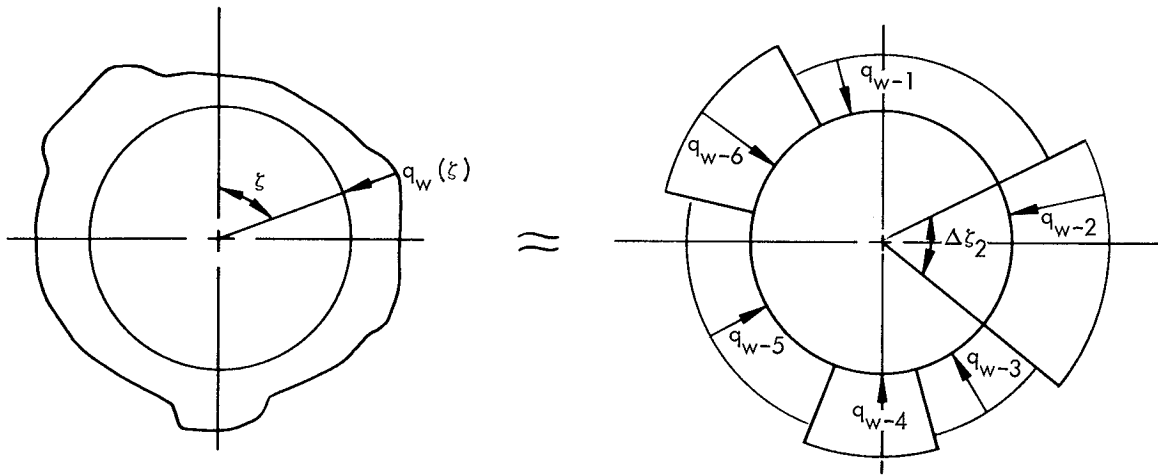
Fig. 3-1 Approximation of Arbitrary Azimuthally Varying Heat Rate
(Plan View of Tank)

This expression becomes

$$\frac{d\Delta}{dt} = \frac{2}{R} \sum_n \left\{ \frac{\Delta \zeta}{2\pi} \left[\int_0^\infty u \, dy \right]_{x=H-\Delta} \right\}_n \tag{3.2}$$

Using the modified turbulent boundary-layer analysis (Ref. 1), the following equation
for the stratified layer growth is obtained:

$$\frac{\Delta}{H} = 1 - \left[1 + \frac{0.0148 \, (H/R) \, \phi_H}{Pr^{2/3} \left(1 + 0.443 \, Pr^{2/3} \right)^{2/7}} \sum_n \Delta \zeta_n \left(Gr_H^* \right)_n^{2/7} \right]^{-7} \tag{3.3}$$

where

$$\left(Gr_H^* \right)_n = \frac{g\beta H^4}{k\nu^2} \left(q_w \right)_n \tag{3.4}$$

Using this result, an energy balance gives the surface temperature rise for times before $\Delta/H = 0.95$:

$$\frac{(T_S - T_0)}{\left[\dfrac{H \displaystyle\int_0^{2\pi} q_w \, d\zeta}{\pi k}\right]} = \frac{(H/R) \, \phi_H}{I \, Pr \left\{ 1 - \left[1 + \dfrac{0.0148 \, (H/R) \, \phi_H}{Pr^{2/3} \left(1 + 0.443 \, Pr^{2/3}\right)^{2/7} \displaystyle\sum_n \Delta\zeta_n \left(Gr_H^*\right)_n^{2/7}} \right]^{-7} \right\}}$$

(3.5)

If ϕ_{H_a} is defined as the time when $\Delta/H = 0.95$, then

$$\phi_{H_a} = \frac{36.2 \, Pr^{2/3} \left(1 + 0.443 \, Pr^{2/3}\right)^{2/7}}{(H/R) \displaystyle\sum_n \Delta\zeta_n \left(Gr_H^*\right)_n^{2/7}}$$

(3.6)

Following the same procedure as that previously used (Ref. 1) for $\phi_H > \phi_{H_a}$, an expression is obtained for the surface temperature rise after the stratified layer reaches the tank bottom:

$$\frac{(T_S - T_0)}{\left[\dfrac{H \displaystyle\int_0^{2\pi} q_w \, d\zeta}{\pi k}\right]} = (H/R) \, \frac{\phi_H}{Pr} + \frac{36.2 \left(1 + 0.443 \, Pr^{2/3}\right)^{2/7} (1 - I)}{I \, Pr^{1/3} \displaystyle\sum_n \Delta\zeta_n \left(Gr_H^*\right)_n^{2/7}}$$

(3.7)

The surface temperature rise is unaffected by bottom heating according to Model I for stratification with both sidewall and bottom heating. (See Section 2.) Equations (3.5) and (3.7) therefore may be used if there is bottom heating, to obtain the growth of the thermal stratified layer Δ_2 from Eq. (2.3). The bottom temperature is then obtained from Eq. (2.2).

3-3

3.2 EXPERIMENTS

3.2.1 Facility and Experimental Procedures

A series of five tests, using the 9.75-in.-diam. tank with water as the working fluid, was conducted to investigate the effect of asymmetric sidewall heating on stratification with and without bottom heating. The tank was installed in the radiant heating facility with radiation reflectors positioned 180 deg apart and in such a manner that uniform but different heat fluxes could be imposed on each 180-deg section of the tank sidewall surface. The two banks of sidewall heating lamps and the bottom heater were independently calibrated, using the tank filled with water as a calorimeter. The thermocouple probe used for these tests was made up of five vertical elements, each with six copper-constantan thermocouples which measured the vertical temperature profile at the position of the element. This probe was designed to detect asymmetry in the bulk fluid temperature distribution. The probe location is shown in Fig. 3-2.

A summary of test conditions is given in Table 3-1. The heat fluxes shown in the table are based on the calibrated heat input from the radiant lamps. In order to obtain heat fluxes which represent the energy in the bulk fluid, the following procedure was used. It was assumed that the heat entering the tank bottom was equal to the calibration value, i.e., that none of the bottom-heating energy entered the sidewall boundary layer. It was further assumed that the amount of sidewall energy stored in the boundary layer or lost by evaporation was proportional to the value of the incident heat flux on that side.

Using these assumptions and the energy in the bulk fluid obtained from an integration of the temperature profiles, sidewall heat fluxes which were consistent with the energy in the bulk fluid were obtained. Evaporation losses were small in these runs, and the heat fluxes obtained in this manner agreed well with the calibrated heat-flux values. The Prandtl and modified Grashof numbers shown in Table 3-1 are nominal values for each run.
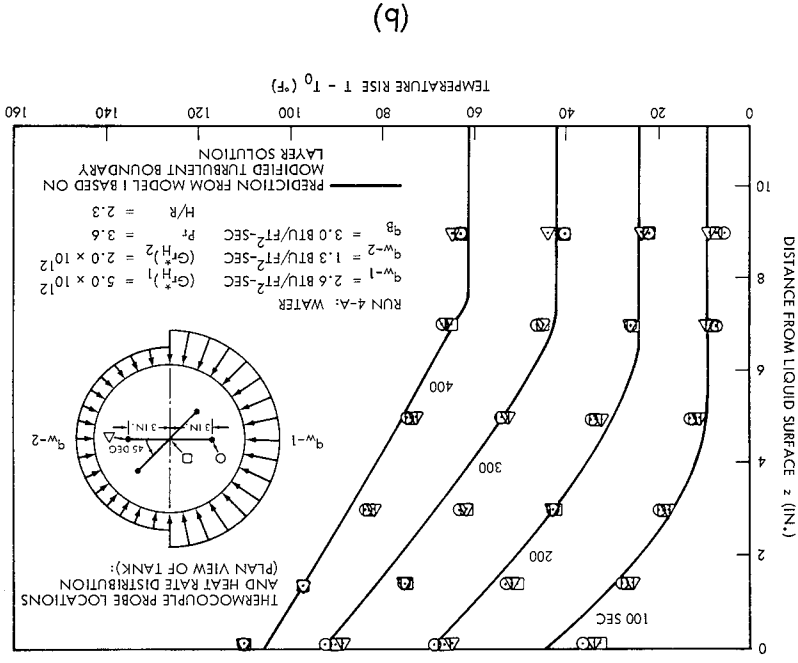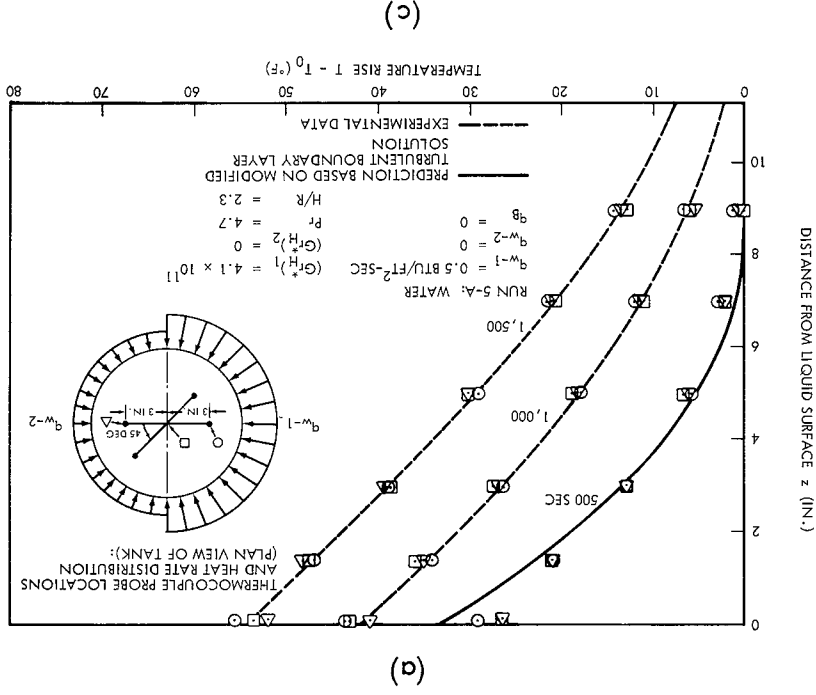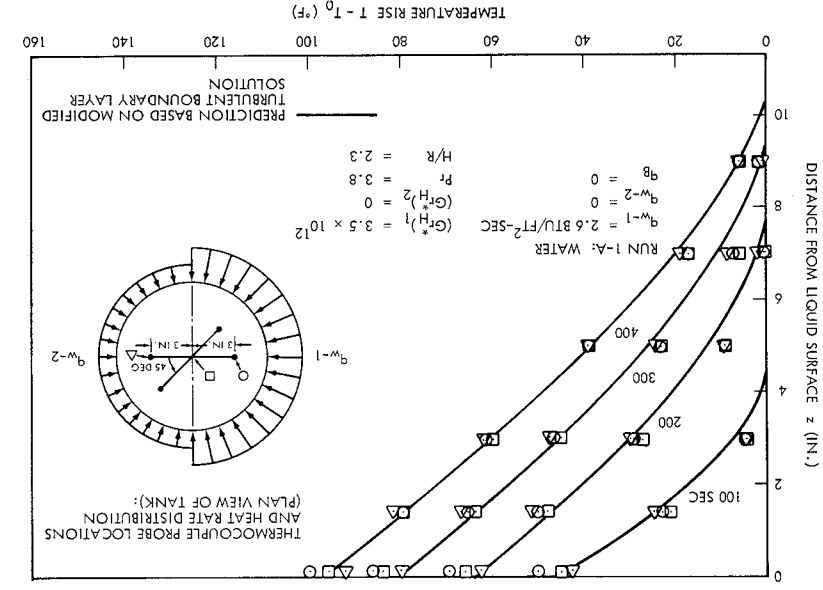
Fig. 3-2 Comparison of Experimental Data With Predictions for Stratification Temperature Profiles With Asymmetric Sidewall Heating

(a)

TEMPERATURE RISE $T - T_0$ (°F)

RUN 1-A: WATER

$q_{w-1} = 2.6$ BTU/FT²-SEC $(Gr_H^*)_1 = 3.5 \times 10^{12}$

$q_{w-2} = 0$ $(Gr_H^*)_2 = 0$

$q_B = 0$ Pr $= 3.8$

H/R $= 2.3$

PREDICTION BASED ON MODIFIED TURBULENT BOUNDARY LAYER SOLUTION

THERMOCOUPLE PROBE LOCATIONS AND HEAT RATE DISTRIBUTION (PLAN VIEW OF TANK):

q_{w-2} q_{w-1}

45 DEG   3 IN.   3 IN.

100 SEC   200   300   400

DISTANCE FROM LIQUID SURFACE z (IN.)

(b)

TEMPERATURE RISE $T - T_0$ (°F)

RUN 4-A: WATER

$q_{w-1} = 2.6$ BTU/FT²-SEC $(Gr_H^*)_1 = 5.0 \times 10^{12}$

$q_{w-2} = 1.3$ BTU/FT²-SEC $(Gr_H^*)_2 = 2.0 \times 10^{12}$

$q_B = 3.0$ BTU/FT²-SEC Pr $= 3.6$

H/R $= 2.3$

PREDICTION FROM MODEL I BASED ON MODIFIED TURBULENT BOUNDARY LAYER SOLUTION

THERMOCOUPLE PROBE LOCATIONS AND HEAT RATE DISTRIBUTION (PLAN VIEW OF TANK):

q_{w-2} q_{w-1}

45 DEG   3 IN.   3 IN.

100 SEC   200   300   400

DISTANCE FROM LIQUID SURFACE z (IN.)

(c)

TEMPERATURE RISE $T - T_0$ (°F)

RUN 5-A: WATER

$q_{w-1} = 0.5$ BTU/FT²-SEC $(Gr_H^*)_1 = 4.1 \times 10^{11}$

$q_{w-2} = 0$ $(Gr_H^*)_2 = 0$

$q_B = 0$ Pr $= 4.7$

H/R $= 2.3$

PREDICTION BASED ON MODIFIED TURBULENT BOUNDARY LAYER SOLUTION

EXPERIMENTAL DATA

THERMOCOUPLE PROBE LOCATIONS AND HEAT RATE DISTRIBUTION (PLAN VIEW OF TANK):

q_{w-2} q_{w-1}

45 DEG   3 IN.   3 IN.

500 SEC   1,000   1,500

DISTANCE FROM LIQUID SURFACE z (IN.)

Table 3-1

SUMMARY OF TEST CONDITIONS FOR ASYMMETRIC SIDEWALL HEATING STRATIFICATION
EXPERIMENTS WITH WATER IN THE 9.75-INCH-DIAMETER TANK

$(H/R = 2.3)$

Run No.	Wall Heat Flux Side No. 1 q_{w-1} (Btu/ft^2-sec)	Wall Heat Flux Side No. 2 q_{w-2} (Btu/ft^2-sec)	Bottom Heat Flux q_B (Btu/ft^2-sec)	Modified Grashof No. Side No. 1 $(Gr^*_H)_1$	Modified Grashof No. Side No. 2 $(Gr^*_H)_2$	Prandtl No. Pr
1A	2.6	0	0	3.5×10^{12}	0	3.8
2A	2.6	1.3	0	3×10^{12}	1.5×10^{12}	3.8
3A	2.6	1.3	1.3	5×10^{12}	2.5×10^{12}	3.6
4A	2.6	1.3	3.0	5×10^{12}	2.5×10^{12}	3.6
5A	0.5	0	0	4.1×10^{11}	0	4.7

3.2.2 Results and Comparisons to Predictions

Some temperature profiles which are typical of those measured are shown in Fig. 3-2. The most important result is that the temperature distributions are radially uniform in spite of the asymmetric heating. In Runs 1-A and 5-A, only one side was heated (an extreme asymmetric condition), and the bulk temperatures remained relatively free of radial gradients. Since all five vertical elements of the thermocouple probe registered essentially the same temperature response, measurements from only three are shown. It is implied by the results obtained that a wall boundary layer, which is formed on only one side, spreads uniformly across the entire liquid surface in a relatively short period of time. Before this result may be generalized, additional factors must be considered. The ability of the boundary layer to spread across the entire surface is probably a function of the tank size and shape as well as the boundary-layer characteristics. This aspect will be discussed subsequently in more detail.

Run 5-A was conducted in an attempt to obtain an asymmetric bulk temperature distribution. In this run, one half of the sidewall was subjected to a heat flux equal to 20 percent of that used in Run 1-A, and the other half of the sidewall was not heated. It was expected that this reduction in heat rate would reduce the tendency of the fluid from the boundary layer to spread quickly across the entire liquid surface. However, the spreading persisted, and the bulk temperature distributions were again without significant radial gradients.

Predictions for the temperature profiles are also shown in Fig. 3-2. In Fig. 3-2c, predictions are not given for 1,000 sec and 1,500 sec, since the temperature profile is not defined after the mass stratified layer has reached the tank bottom when there is no bottom heating. Very good agreement is indicated between the data and predictions both with and without bottom heating.

Runs 1-A, 2-A, and 5-A were not subjected to bottom heating, and the data may be compared with the prediction for the mass stratified layer growth. This comparison is shown in Fig. 3-3 and indicates that the data agree very well with the prediction. Since the data obtained with uniform sidewall and bottom heating (Subsection 2.2)

FRACTION STRATIFIED Δ/H

1.0

0.8

0.6

0.4

0.2

0

H/R = 2.3

PREDICTION BASED ON MODIFIED TURBULENT
BOUNDARY LAYER SOLUTION:

$$\frac{\Delta}{H} = 1 - \left[1 + \frac{0.0148 \, (H/R) \, \phi_H}{Pr^{2/3} \left(1 + 0.443 \, Pr^{2/3} \right)^{2/7}} \sum_n \Delta \zeta_n \left(Gr_H^* \right)_n^{2/7} \right]^{-7}$$

PLAN VIEW OF TANK:

q_{w-1} q_{w-2}

SYMBOL	q_{w-1} (BTU/FT²-SEC)	q_{w-2} (BTU/FT²-SEC)	$(Gr_H^*)_1$	$(Gr_H^*)_2$	Pr
⊙	2.6	0	3.5×10^{12}	0	3.8
⊡	2.6	1.3	3×10^{12}	1.5×10^{12}	3.8
◇	0.5	0	4.1×10^{11}	0	4.7

0   0.1   0.2   0.3   0.4   0.5   0.6   0.7   0.8

GEOMETRY-TIME-GRASHOF-PRANDTL PARAMETER GROUP
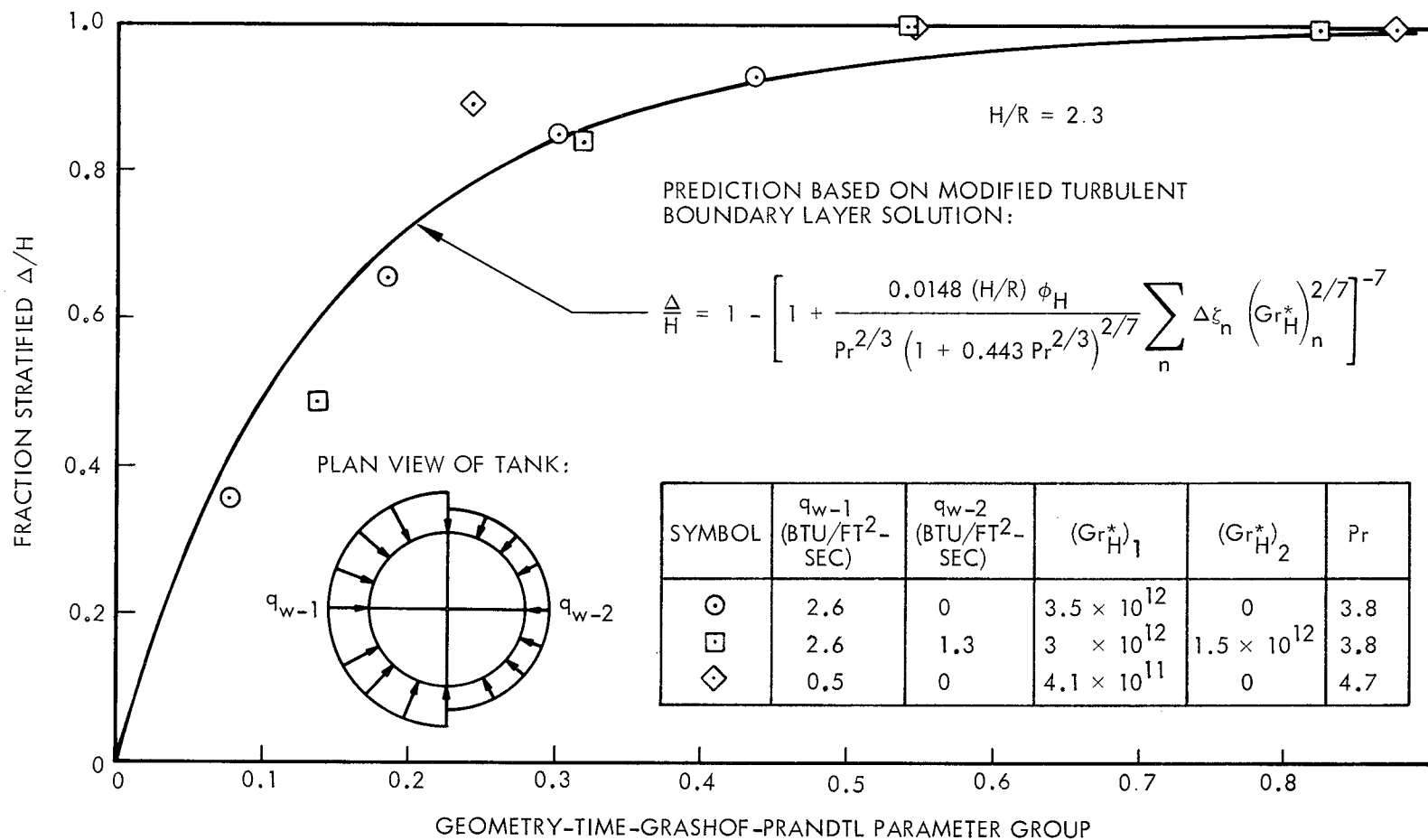
Fig. 3-3 Comparison of Experimental Data With Prediction for Stratified
Layer Growth With Asymmetric Sidewall Heating

indicate that the surface temperature rise is unaffected by bottom heating, the data obtained from all of the asymmetric heating runs can be compared with the surface temperature rise predictions. Figure 3-4 shows the data compared with surface temperature rise predictions for times before the mass stratified layer reached the tank bottom; Fig. 3-5 shows the comparison of data and predictions for times after the mass stratified layer reached the tank bottom. The data verify the validity of the predictions and the assumptions made to obtain them.

3.3 APPLICATION OF ANALYSIS

In order to extend the applicability of the analysis developed in Subsection 3.1, some indication of the bulk temperature asymmetry to be expected in other tanks with other fluids must be obtained. It is suggested that the degree of asymmetry in the bulk temperature distribution is a function of the time for the boundary-layer fluid to spread across the liquid surface compared with the time required for the bulk to stratify. If the boundary-layer fluid spreads much faster than the bulk stratifies, it is expected that the bulk temperature distribution will be relatively free of radial gradients.

For a turbulent boundary layer, the following relation is obtained for the stratified layer growth rate (Ref. 1):

$$\frac{d\Delta}{dt} \propto \frac{\nu}{R} \left(Gr_H^*\right)^{2/7} Pr^{-2/3} \left(1 + 0.443 \, Pr^{2/3}\right)^{-2/7} \left(1 - \frac{\Delta}{H}\right)^{8/7} \tag{3.8}$$

If time zero is selected as a reference for comparison, which also gives the highest stratification rate, then a characteristic time to stratify can be defined as

$$t_{strat} \equiv H/(d\Delta/dt)_{t=0} \tag{3.9}$$

PREDICTION BASED ON MODIFIED TURBULENT BOUNDARY LAYER SOLUTION:

$$\frac{T_S - T_0}{\left[\dfrac{H \int_0^{2\pi} q_w \, d\ell}{\pi k}\right]} = \frac{(H/R)\,\phi_H}{I\,Pr\left\{1 - \left[1 + \dfrac{0.0148\,(H/R)\,\phi_H}{Pr^{2/3}\left(1 + 0.443\,Pr^{2/3}\right)^{2/7}} \sum_n \Delta\zeta_n \left(Gr_H^*\right)_n^{2/7}\right]^{-7}\right\}}$$

H/R = 2.3

PLAN VIEW OF TANK

q_{w-1} q_{w-2}

SYMBOL	q_{w-1} (BTU/FT^2-SEC)	q_{w-2} (BTU/FT^2-SEC)	q_B (BTU/FT^2-SEC)	$\left(Gr_H^*\right)_1$	$\left(Gr_H^*\right)_2$	Pr
⊙	2.6	0	0	3.5×10^{12}	0	3.8
⊡	2.6	1.3	0	3×10^{12}	1.5×10^{12}	3.8
△	2.6	1.3	1.3	5×10^{12}	2.5×10^{12}	3.6
▽	2.6	1.3	3	5×10^{12}	2.5×10^{12}	3.6
◇	0.5	0	0	4.1×10^{11}	0	4.7

DIMENSIONLESS SURFACE TEMPERATURE RISE $(T_S - T_0) \Big/ \left[\left(H \int_0^{2\pi} q_w \, d\zeta\right)\Big/ \pi k\right]$

10^{-2}

10^{-3}

10^{-3} 10^{-2}

GEOMETRY–TIME–GRASHOF–PRANDTL PARAMETER GROUP

$$\frac{(H/R)\,\phi_H}{I\,Pr\left\{1 - \left[1 + \dfrac{0.0148\,(H/R)\,\phi_H}{Pr^{2/3}\left(1 + 0.443\,Pr^{2/3}\right)^{2/7}} \sum_n \Delta\zeta_n \left(Gr_H^*\right)_n^{2/7}\right]^{-7}\right\}}$$

Fig. 3-4   Comparison of Experimental Data With Prediction for Surface Temperature Rise in Asymmetric Sidewall Heating Stratification

PREDICTION BASED ON MODIFIED TURBULENT BOUNDARY
LAYER SOLUTION AND CORRELATION FOR TIMES AFTER
MASS STRATIFIED LAYER REACHES TANK BOTTOM:

$$(T_S - T_0) / \left(H \int_0^{2\pi} q_w \, d\zeta / \pi k \right) = (H/R) \frac{\phi_H}{Pr} + \frac{36.2 \left(1 + 0.443 \, Pr^{2/3}\right)^{2/7} (1 - I)}{I (Pr)^{1/3} \sum_n \Delta\zeta_n \left(Gr_H^*\right)_n^{2/7}}$$

Y-axis: DIMENSIONLESS SURFACE TEMPERATURE RISE $(T_S - T_0) / \left[\left(H \int_0^{2\pi} q_w \, d\zeta \right) / \pi k \right]$

$H/R = 2.3$

PLAN VIEW OF TANK

q_{w-1} q_{w-2}

SYMBOL	q_{w-1} (BTU-FT^2-SEC)	q_{w-2} (BTU/FT^2-SEC)	q_B (BTU/FT^2-SEC)	$(Gr_H^*)_1$	$(Gr_H^*)_2$	Pr
⊡	2.6	1.3	0	3×10^{12}	1.5×10^{12}	3.8
△	2.6	1.3	1.3	5×10^{12}	2.5×10^{12}	3.6
▽	2.6	1.3	3	5×10^{12}	2.5×10^{12}	3.6
◇	0.5	0	0	4.1×10^{11}	0	4.7

X-axis: GEOMETRY-TIME-GRASHOF-PRANDTL PARAMETER GROUP

$$(H/R) \frac{\phi_H}{Pr} + \frac{36.2 \left(1 + 0.443 \, Pr^{2/3}\right)^{2/7} (1 - I)}{I \, Pr^{1/3} \sum_n \Delta\zeta_n \left(Gr_H^*\right)_n^{2/7}}$$

Fig. 3-5 Comparison of Experimental Data With Prediction for Surface Temperature
Rise in Asymmetric Sidewall Heating Stratification

3-11

LOCKHEED MISSILES & SPACE COMPANY

Fig. 3-6 Free Jet Model Assumed for Spreading

In order to obtain a combination of significant parameters which characterizes the spreading velocity, the velocity along the center of a two-dimensional turbulent free jet (Fig. 3-6) will be examined. From Ref. 2:

$$\text{Centerline velocity} \; = \; u_c \; = \; \sqrt{\frac{3u_s^2 \ell \sigma}{2y}} \tag{3.10}$$

To adapt this relation to the spreading of a boundary layer it will be assumed that $\ell =$ boundary layer thickness at the liquid surface, and that $u_s = (u_1)_H$, the characteristic boundary layer velocity at the liquid surface.

Then, evaluating the centerline velocity at $y = R$ for reference

$$\left(u_c\right)_R \; \propto \; \left(u_1\right)_H \left(\frac{\delta_H}{R}\right)^{1/2} \tag{3.11}$$

A characteristic time to spread can be defined as

$$t_{SPREAD} \; \equiv \; \frac{R}{\left(u_c\right)_R} \tag{3.12}$$

3-12

The boundary-layer characteristic velocity and thickness from the modified turbulent boundary-layer analysis are given in Ref. 3.

$$\left(u_1\right)_H = 4.34 \frac{\nu}{H} \left(Gr_H^*\right)^{5/14} Pr^{-1/6} \left(1 + 0.443\, Pr^{2/3}\right)^{-5/14} \tag{3.13}$$

$$\frac{\delta_H}{R} = 0.510 \frac{H}{R} \left(Gr_H^*\right)^{-1/14} Pr^{-1/2} \left(1 + 0.443\, Pr^{2/3}\right)^{1/14} \tag{3.14}$$

Then, combining Eqs. (3.8), (3.9), (3.11), (3.12), (3.13), and (3.14), the two characteristic times may be compared to obtain a measure of the "spreadability":

$$\frac{\text{characteristic time to stratify}}{\text{characteristic time to spread}} \propto \left(\frac{H}{R}\right)^{1/2} \left(\frac{Gr_H^*}{1 + 0.443\, Pr^{2/3}}\right)^{1/28} Pr^{1/4} \equiv S \tag{3.15}$$

The relative values of S for the test tank described in Subsection 3.2 and a liquid hydrogen tank of a typical cryogenic upper stage like the S-IV can be compared. Assume for the S-IV tank:

$$Gr_H^* = 6 \times 10^{18}$$
$$Pr = 1.0$$
$$H/R = 1.5$$

For Test Run 5-A

$$Gr_H^* = 4.1 \times 10^{11}$$
$$Pr = 4.7$$
$$H/R = 2.3$$

Then

$$\frac{S_{\text{S-IV}}}{S_{\text{test tank}}} = 0.97$$

3-13

This result indicates that spreading in the S-IV tank will be sufficiently fast to produce a uniform bulk temperature gradient when heated on only one side. It should be noted that this "spreadability" factor is only used to gain insight for a very complicated phenomenon. The use of a two-dimensional, free-jet velocity expression and the accompanying assumptions must be treated as order of magnitude approximations. However, the foregoing argument somewhat justifies the assumption of a uniform bulk temperature distribution for prediction of the results of stratification in large cryogenic tanks like the S-IV when subjected to asymmetric heating. If this assumption is made, Eqs. (3.3), (3.5) and (3.7) of Subsection 3.1 can be used to predict the stratified layer growth and surface temperature rise (excluding ullage-coupling considerations) in such a tank.

Section 4
EFFECT OF TANK ASPECT RATIO ON STRATIFICATION

All the stratification data reported in Ref. 1 and in Sections 2 and 3 of this report, which verified the validity of the integral technique stratification analysis, were obtained in tanks with an aspect ratio H/R of 2.3. From these data, the dependence of the energy integral on the modified Grashof number was established, and it was determined that the energy integral is not a function of Prandtl number (Ref. 1). In order to verify the validity of the stratification analysis for an aspect ratio other than 2.3, and to determine whether the energy integral is a function of H/R, a series of 10 stratification experiments was conducted with water, using a tank with an aspect ratio of 4.7.

4.1 EXPERIMENTAL FACILITY AND PROCEDURES

The facility used for these tests was the 10.75-in.-diam. pressure vessel shown in Fig. 4-1. This tank was constructed from a 30-in. length of flanged steel pipe with an 11.75-in. i.d. A rolled epoxy tube with a glass cloth base and a 0.5-in. wall was tightly fitted inside the steel pipe from top to bottom. A cylindrical electric-resistance heating shell, made from 6-in.-wide strips of 0.001-in.-thick stainless steel, was attached to the inside wall of the epoxy tube. One of the annular copper bus bars which carries current to the heater strips was mounted at the bottom of the tank; the other, which could be mounted at any height desired, was positioned so that the aspect ratio of the stratifying fluid was 4.7. Fluid temperatures were measured along the cylindrical axis with 13 thermocouples mounted on a probe, which was supported on the tank bottom. The bottom end plate also accommodated a drain line, and the top plate was provided with a fill line and a pressurant line. The outside of the steel shell was insulated with a 2-in.-thick layer of fiberglass batting which was covered with a cork sheet for support and protection. The sight glass on the side of the tank was used to monitor the liquid level.
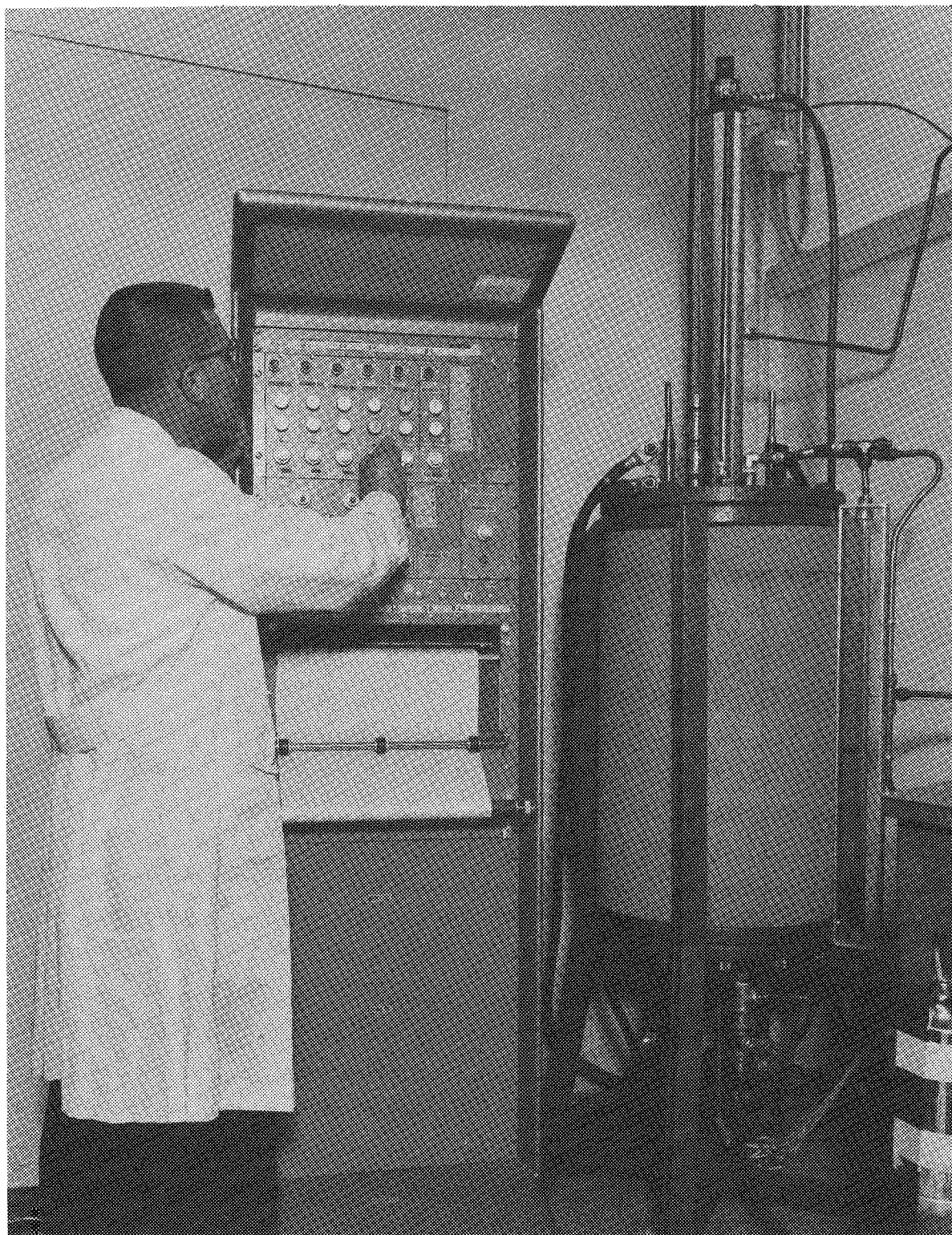
Fig. 4-1 Pressure Facility for Stratification Experiments

LOCKHEED MISSILES & SPACE COMPANY

The range of test conditions covered is shown in Table 4-1. The modified Grashof and Prandtl numbers shown in the table are nominal values for each run. Fluid properties used in the graphical presentation of results were evaluated at the mixed mean temperature of the fluid in the stratified layer. Heat fluxes were determined by graphically integrating the temperature profiles. A wide range of modified Grashof numbers was covered ($3.7 \times 10^{10} \leq Gr_H^* \leq 2.5 \times 10^{15}$) by using water and varying the heat rate and water temperature. The high modified Grashof numbers were obtained at a high heat rate with water which was pressurized to 150 psig with nitrogen to subcool it at temperatures above 250°F. Low values for the modified Grashof number were obtained using low heat fluxes and precooled water. The water for these tests was precooled to about 40°F by pumping it through an ice bath prior to each run.

Table 4-1

SUMMARY OF TEST CONDITIONS AND RESULTS FOR HIGH ASPECT RATIO
STRATIFICATION EXPERIMENTS WITH WATER IN THE 10.75-INCH-
DIAMETER PRESSURE VESSEL

(H/R = 4.7)

Run No.	Heat Flux q_w (Btu/ft^2-sec)	Modified Grashof Number Gr_H^*	Prandtl Number Pr	Energy Integral I
214	0.095	3.7×10^{10}	10.4	0.348
211	0.086	7.7×10^{10}	9.8	0.311
215	0.110	3.0×10^{11}	8.5	0.316
203	0.110	1.9×10^{12}	5.2	0.439
204	1.04	2.1×10^{13}	4.9	0.524
206	1.85	1.2×10^{14}	3.2	0.575
207	2.80	2.8×10^{14}	2.6	0.611
208	3.20	6.6×10^{14}	1.9	0.590
209	4.90	1.3×10^{15}	1.7	0.557
210	6.50	2.5×10^{15}	1.5	0.583

4.2 EXPERIMENTAL RESULTS

The measured temperature profiles for these tests are shown in Fig. 4-2. The change in temperature profile shape as a function of modified Grashof number is the same as that obtained for H/R = 2.3 (Ref. 1). A perturbation of the profiles near the liquid surface was observed in Runs 206 through 210. As the modified Grashof number is increased, this "surface bend-back" becomes larger. The most severe case in the high aspect ratio test series is shown in Fig. 4-2d. This effect was observed in some of the data obtained with H/R = 2.3 at lower modified Grashof numbers in the pressure vessel (Subsection 5.2) and in the 3-in.-diam. tank (Ref. 4). The cause of this phenomen is still unknown.

According to the criterion established in Subsection 2.2, at least half of the wall boundary layer is turbulent for all but two of the runs. Since transition occurs very near the half-way point in these two runs, all of the high aspect ratio data are compared with predictions based on the modified turbulent boundary layer analysis. This comparison is made for the stratified layer growth in Fig. 4-3. The results shown for H/R = 4.7 are similar to those previously obtained with H/R = 2.3 (Ref. 1). The data again indicate that the stratified layer growth proceeds faster than predicted by the modified turbulent boundary layer solution.

The dimensionless form of the temperature profiles is shown in Fig. 4-4. The profiles are similar (time-invariant) until the "surface bend-back" becomes significant. The data scatter shown in Figs. 4-4c and 4-4d results from this surface effect.

In Fig. 4-5 the high aspect ratio data for the surface temperature rise are compared with the prediction based on the modified turbulent boundary layer solution. The surface temperatures for the three highest modified Grashof number runs (208, 209, and 210) were taken from an extrapolation of the temperature profiles to the surface as shown in Fig. 4-2d. Apart from the surface effect, the deviation of the data from the prediction can be attributed primarily to the low prediction of the stratified layer growth.
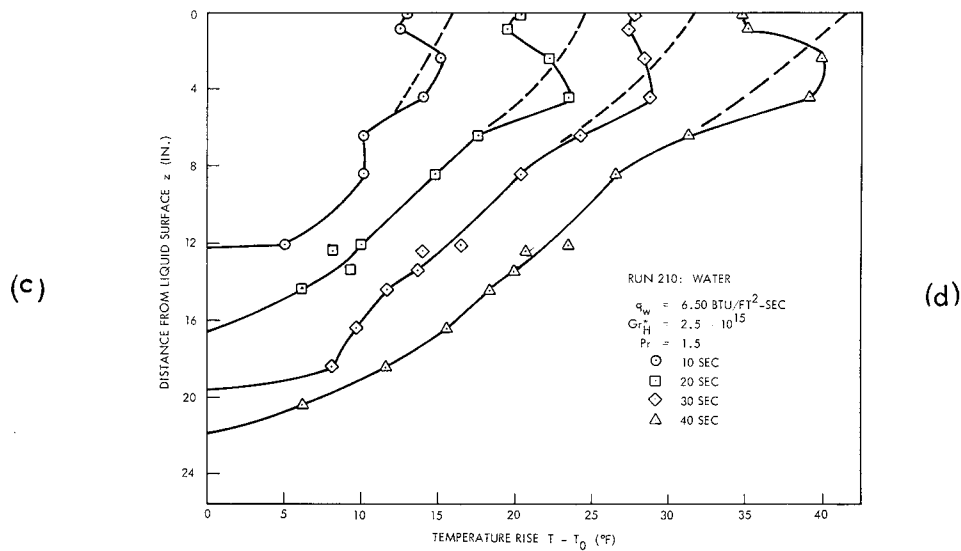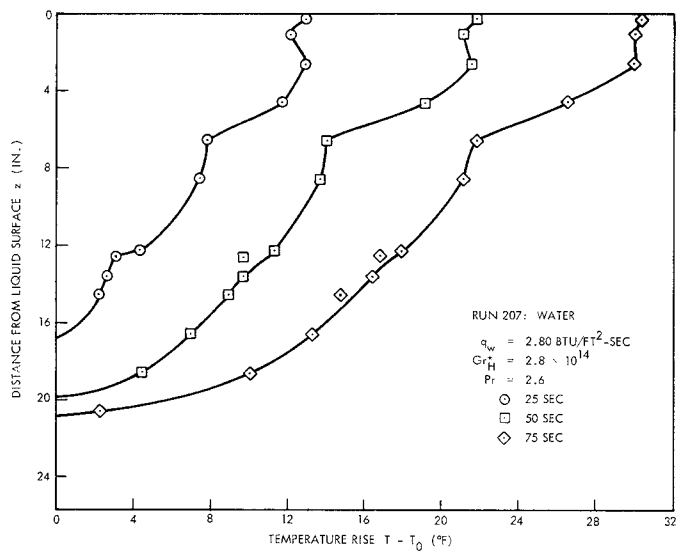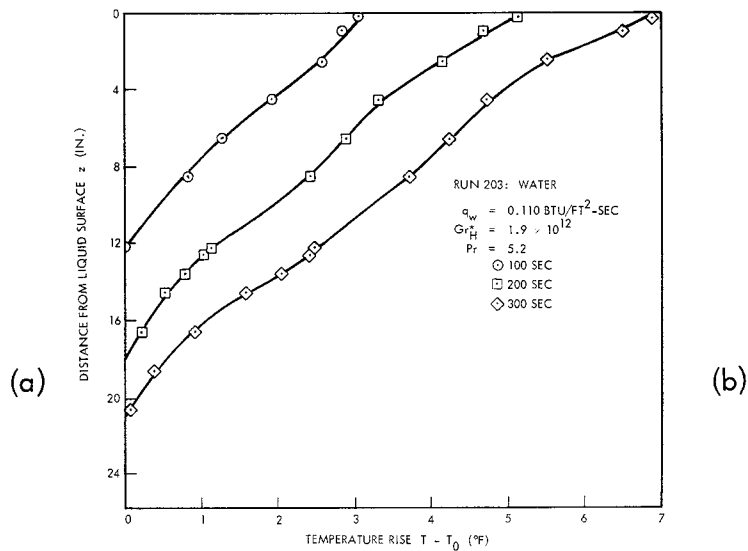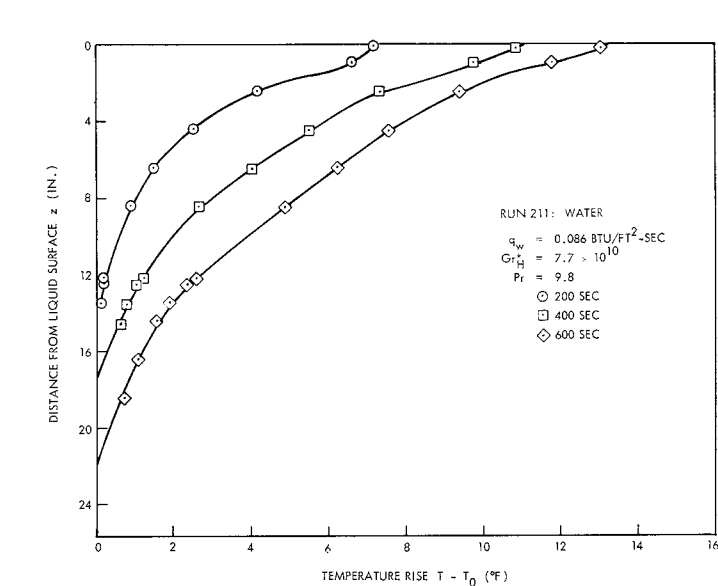
Fig. 4-2 Stratification Temperature Profiles for H/R = 4.7

H/R = 4.7

PREDICTION BASED ON MODIFIED TURBULENT
BOUNDARY LAYER SOLUTION:

$$\frac{\Delta}{H} = 1 - \left[1 + 0.0924 \ \frac{H}{R} \ \phi_H \ Pr^{-2/3} \left(\frac{Gr_H^*}{1 + 0.443 \ Pr^{2/3}}\right)^{2/7}\right]^{-7}$$

SYMBOL	q_w (BTU/FT^2-SEC)	Gr_H^*	Pr
⬦	0.095	3.7×10^{10}	10.4
▽	0.086	7.7×10^{10}	9.8
◇	0.11	3.0×10^{11}	8.5
○	0.11	1.9×10^{12}	5.2
⊡	1.04	2.1×10^{13}	4.9
◇	1.85	1.2×10^{14}	3.2
△	2.80	2.8×10^{14}	2.6
▷	3.2	6.6×10^{14}	1.9
◁	4.9	1.3×10^{15}	1.7
⬠	6.5	2.5×10^{15}	1.5

GEOMETRY-TIME-GRASHOF-PRANDTL PARAMETER GROUP $(H/R) \ \phi_H \ Pr^{-2/3} \left(\frac{Gr_H^*}{1 + 0.443 \ Pr^{2/3}}\right)^{2/7}$

FRACTION STRATIFIED Δ/H

Fig. 4-3 Comparison of Experimental Data With Prediction for Stratified
Layer Growth With Sidewall Heating

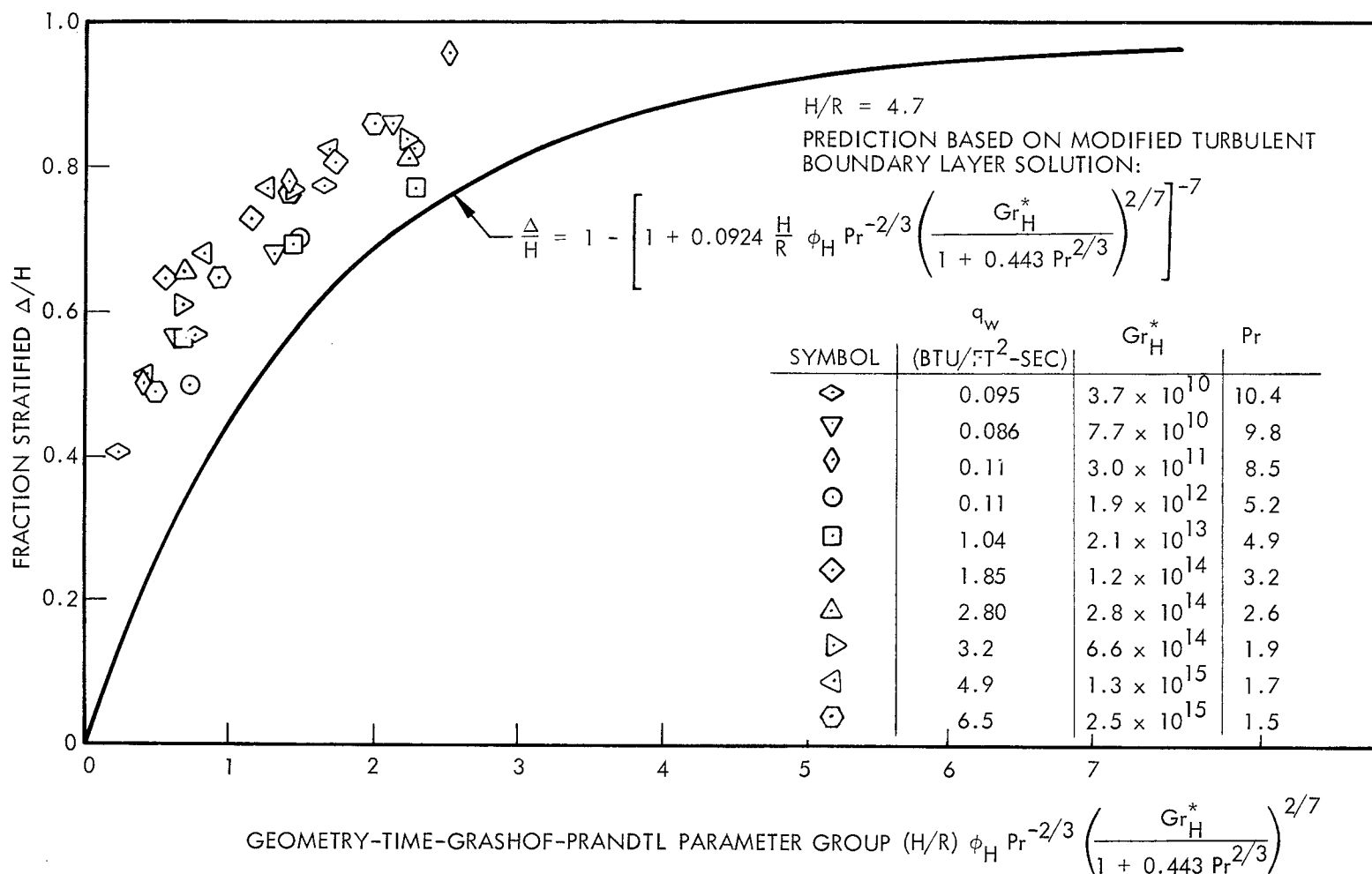Fig. 4-4 Dimensionless Stratification Temperature Profiles

PREDICTION BASED ON MODIFIED TURBULENT
BOUNDARY LAYER SOLUTION:

$$\frac{T_S - T_0}{(q_w H)/k} = \frac{2(H/R)\,\phi_H}{I\,Pr\left\{1 - \left[1 + 0.0924\,(H/R)\,\phi_H\,Pr^{-2/3}\left(\frac{Gr_H^*}{1 + 0.443\,Pr^{2/3}}\right)^{2/7}\right]^{-7}\right\}}$$

$H/R = 4.7$

DIMENSIONLESS SURFACE TEMPERATURE RISE $(T_S - T_0)/[(q_w H)/k]$

GEOMETRY-TIME-GRASHOF-PRANDTL PARAMETER GROUP

$$\frac{2(H/R)\,\phi_H}{I\,Pr\left\{1 - \left[1 + 0.0924\,(H/R)\,\phi_H\,Pr^{-2/3}\left(\frac{Gr_H^*}{1 + 0.443\,Pr^{2/3}}\right)^{2/7}\right]^{-7}\right\}}$$

SYMBOL	q_w (BTU/FT^2-SEC)	Gr_H^*	Pr
⬦	0.095	3.7×10^{10}	10.4
▽	0.086	7.7×10^{10}	9.8
◇	0.11	3.0×10^{11}	8.5
☉	0.11	1.9×10^{12}	5.2
⊡	1.04	2.1×10^{13}	4.9
◇	1.85	1.2×10^{14}	3.2
△	2.80	2.8×10^{14}	2.6
▷	3.2	6.6×10^{14}	1.9
◁	4.9	1.3×10^{15}	1.7
⬠	6.5	2.5×10^{15}	1.5
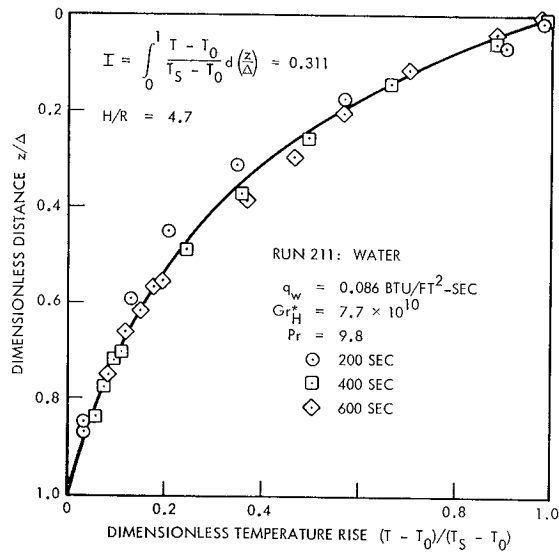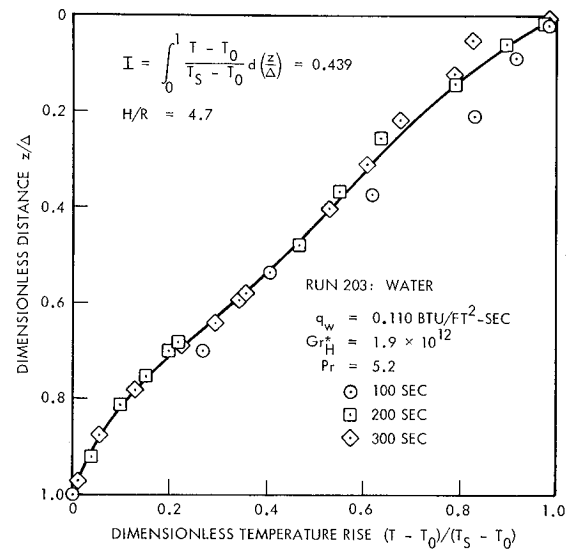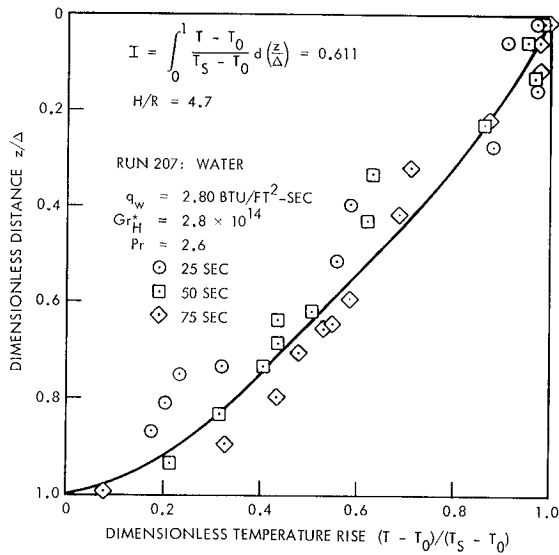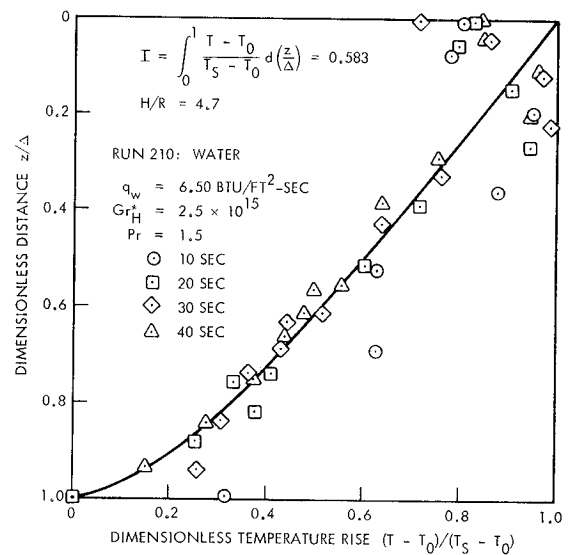
Fig. 4-5 Comparison of Experimental Data With Prediction for Surface Temperature
Rise in Sidewall Heating Stratification

The values for the energy integral with an aspect ratio of 4.7, obtained by graphical integration from the dimensionless temperature profiles, are plotted in Fig. 4-6 as a function of modified Grashof number. A line which represents the best fit of all the data obtained with an aspect ratio of 2.3 (Ref. 1) is also shown on Fig. 4-6. From a comparison of this line with the data points it is concluded that, for aspect ratios within the range of practical values, the energy integral is not a function of tank aspect ratio.

Fig. 4-6 Energy Integral as a Function of Modified Grashof Number

Section 5

LIQUID-ULLAGE COUPLING

Heat transfer to a contained fluid which is near a saturation state will result in stratification in the liquid phase. In addition, significant evaporation or condensation at the liquid free surface and a pre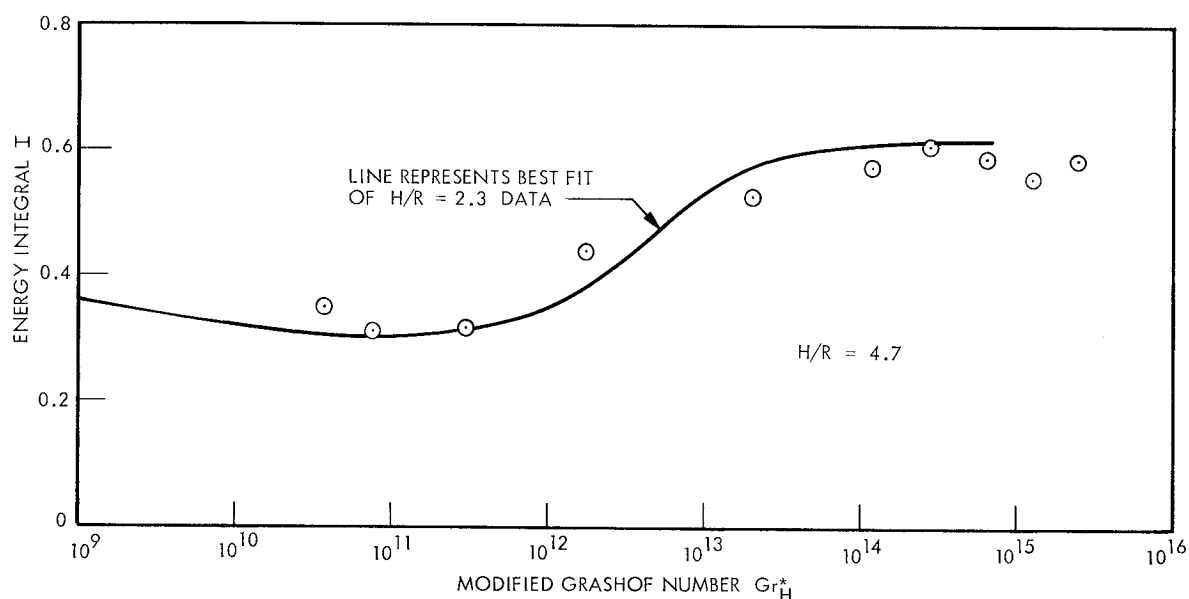ssure and temperature rise of the ullage gas may occur. An analysis of this coupling between liquid and ullage gas, which utilizes the results of the subcooled stratification analysis previously presented, will be outlined in this section. A limited number of experiments have been conducted in the pressure vessel under self-pressurizing conditions with sidewall heating of both liquid and ullage. A preliminary comparison of experimental results with the analytical model will be discussed.

5.1 ANALYSIS

The simplified model used in the present analysis is shown in Fig. 5-1. It is based on the following assumptions:

- The fluid in the cylindrical tank is a single component in the liquid and gas phases with constant properties except for the volumetric expansion effect on buoyancy and liquid volume.
- The bulk of the ullage is at a uniform, mixed temperature.
- The perfect gas equation of state applies to the ullage.
- The ullage pressure is the saturation pressure corresponding to the liquid-vapor interface temperature.
- A vapor and a liquid film exist at the interface and represent resistances to heat transfer across the interface. The physical thickness of the films is neglected.
- The fluid is initially in thermodynamic equilibrium.
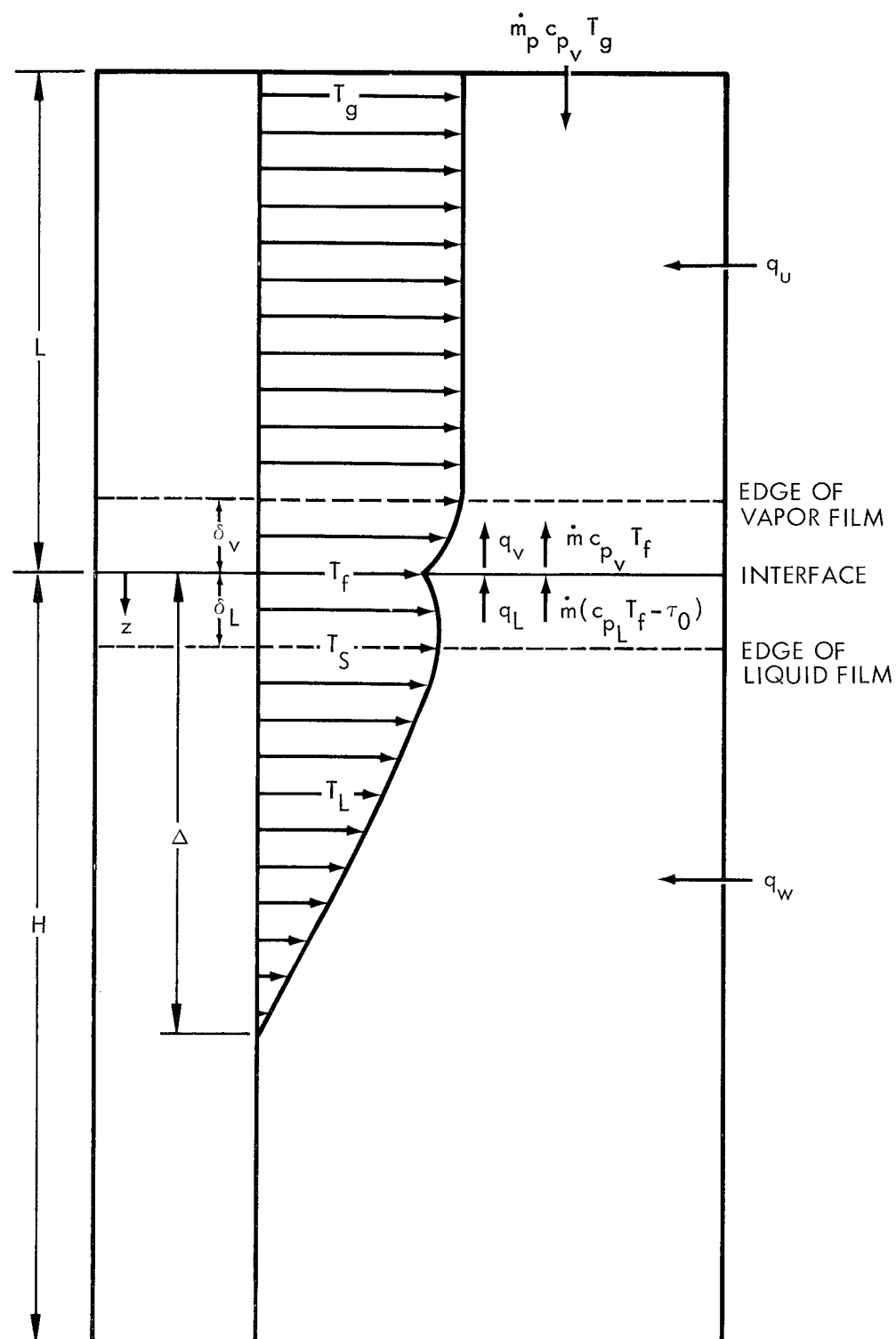
Fig. 5-1 System Model Used in Liquid-Ullage Coupling Analysis

LOCKHEED MISSILES & SPACE COMPANY

It was shown in Section 2 that bottom heating will not affect the surface temperature rise. Bottom heating therefore does not appear explicitly in the formulation of the liquid-ullage coupling model. When it is present, the bottom heat flux defines the thermal stratified layer depth and the uniform bottom temperature.

In the ullage, the model provides for mass addition or removal of gas at the ullage temperature.

An energy balance at the interface may be written as

$$q_L - q_v = \dot{m} \left[\tau_0 + \left(c_{p_v} - c_{p_L} \right) T_f \right] = \dot{m} \lambda \qquad (5.1)$$

The heat flux terms q_L and q_v are related to the temperature differences across the vapor and liquid films by the film heat transfer coefficients

$$h_v = \frac{k_v}{\delta_v} = \frac{\dot{m} c_{p_v}}{\ln \left[1 + \dfrac{\dot{m} c_{p_v} (T_f - T_g)}{q_v} \right]} \qquad (5.2)$$

$$h_L = \frac{k_L}{\delta_L} = \frac{-\dot{m} c_{p_L}}{\ln \left[1 + \dfrac{\dot{m} c_{p_L} (T_f - T_S)}{q_L} \right]} \qquad (5.3)$$

Equations (5.2) and (5.3) result from integration of the energy balances for the films (Ref. 5), using a quasi-steady state approximation, and reflect the assumption that the vapor and liquid films have no mass or energy capacitance (i.e., the thickness is negligible).

For the ullage, an energy balance gives

$$\left(\frac{2L}{R}\right) q_u + q_v + \dot{m} c_{p_v} T_f + \dot{m}_p c_{p_v} T_g = \frac{d\left(M_v c_{v_v} T_g\right)}{dt} + p \frac{dL}{dt} \qquad (5.4)$$

For the liquid, an energy balance yields

$$\left(\frac{2H}{R}\right) q_w - q_L - \dot{m} c_{p_L} (T_f - T_0) = \frac{d}{dt} \int_0^H \rho_L c_{p_L} (T_L - T_0) \, dz + p \frac{dH}{dt}$$

$$(5.5)$$

The rate of change of ullage mass is given by

$$\frac{dM_v}{dt} = \dot{m} + \dot{m}_p \qquad (5.6)$$

If the thermal expansion of the tank is neglected

$$\frac{dL}{dt} = - \frac{dH}{dt} \qquad (5.7)$$

The equation of state for the vapor is taken to be

$$p = \frac{M_v \mathcal{R} T_g}{L} \qquad (5.8)$$

The ullage pressure is related to the interface temperature by the Clausius-Clapeyron equation

$$\frac{p}{p_0} = \exp\left[\frac{\lambda}{\mathcal{R} T_0} \left(1 - \frac{T_0}{T_f}\right)\right] \qquad (5.9)$$

The change in liquid level is due to the interface mass transfer and to the thermal expansion of the liquid. Then

$$\dot{m} = \beta \rho_L \frac{d}{dt} \int_0^H (T_L - T_0) \, dz - \left[\beta (T_S - T_0) + 1 \right] \rho_L \frac{dH}{dt} \qquad (5.10)$$

The time derivative of the temperature integral in Eqs. (5.5) and (5.10) represents the effect of stratification and is given by

$$\frac{d}{dt} \int_0^H (T_L - T_0) \, dz = \frac{d}{dt} \left[(T_S - T_0) \, I \Delta \right] \qquad (5.11)$$

where I is the energy integral (Ref. 1)

$$I = \int_0^1 \frac{T_L - T_0}{T_S - T_0} \, d \left(\frac{z}{\Delta} \right) \qquad (5.12)$$

The above system of nonlinear ordinary differential equations can be solved to give the ullage pressure and temperature and the liquid temperatures. A FORTRAN computer program has been written which integrates the equations by a forward finite difference technique. The input and output in the program are in dimensionless form. The program incorporates the following options for the ullage:

- Closed self-pressurizing tank.
- Continuous venting through a choked orifice: ullage mass is removed at a rate proportional to the pressure and inversely proportional to the square root of the absolute temperature.

- Continuous venting at a constant ullage pressure: ullage mass is removed to maintain a constant pressure and interface temperature. The liquid heat flux is absorbed primarily by vaporization.
- Continuous venting with a programmed ullage pressure or intermittent venting between two pressure levels.

There are three parameters in the analysis which must be determined empirically: the vapor film heat transfer coefficient h_V, the liquid film heat transfer coefficient h_L, and the energy integral I. The values of the heat-transfer coefficients are probably controlled by both free and forced convection effects arising from buoyant forces and spreading velocities near the interface. The energy integral is assumed to be defined by the results previously obtained for subcooled stratification (Figs. 2-5 and 4-6). It is possible that these values may have to be modified to account for mass transfer effects.

5.2 EXPERIMENTS

An experimental program was begun to obtain data on stratification with liquid-ullage coupling. The objectives of the experimental program are as follows:

- To establish the validity of the liquid-ullage coupling model
- To establish criteria for estimating h_V, h_L, and I.

The first objective requires that the model predict the results of experiments over a wide range of boundary conditions while employing a logical and consistent combination of the parameters h_V, h_L, and I. The second objective requires an experimental correlation of the parameters over a range of fluid properties, tank geometry, and boundary conditions.

5.2.1 Facility and Experimental Procedures

The liquid-ullage coupling experiments were conducted in the pressure vessel described in Section 4. The ullage height L was 17.5 in. and the ullage diameter was 9.25 in.

A separate heater was installed in the ullage region in order to control independently the heat rates to the liquid and the gas. The aspect ratio for the liquid was H/R = 2.3. The fluid used was Freon 11, a refrigerant which is saturated at 74.8° F and 1 atm.

The procedure used was to fill the pressure vessel completely with Freon 11 liquid to displace all air. The Freon was then heated, which raised its pressure, and then forced out the tank bottom until the desired liquid level was reached and the tank was filled completely with Freon liquid and vapor. The pressure vessel was then allowed to come to thermal equilibrium with the saturated vapor and liquid. With these initial conditions, the liquid wall heating transient should be nearly identical from run to run for a fixed liquid heater input independent of the ullage heat rate. The heat rate to the liquid was therefore determined as a function of liquid heater input by calibration runs, with the liquid highly subcooled to prevent evaporation to the ullage.

Figure 5-2 shows two typical calibration runs at the same heater input but with different degrees of subcooling by pressurizing with nitrogen. The double-valued profile shape near the surface is concluded to be a hydrodynamic effect rather than a mass transfer effect based on the analysis of Ref. 6.

In order to determine the heat rate to the ullage in a given run, the total energy input to the tank was calculated using the following equation:

$$Q_u + Q_w = \pi R^2 \left[c_{p_L} \int_0^H \rho_L \, (T - T_0) \, dx + c_{p_v} \int_H^{L+H} \rho_v \, (T - T_0) \, dx \right]$$
$$+ \tau_0 \, (\Delta M_v) \qquad (5.13)$$

The ullage heat rate was then determined by subtracting the calibrated liquid heat input from the total calculated heat input.
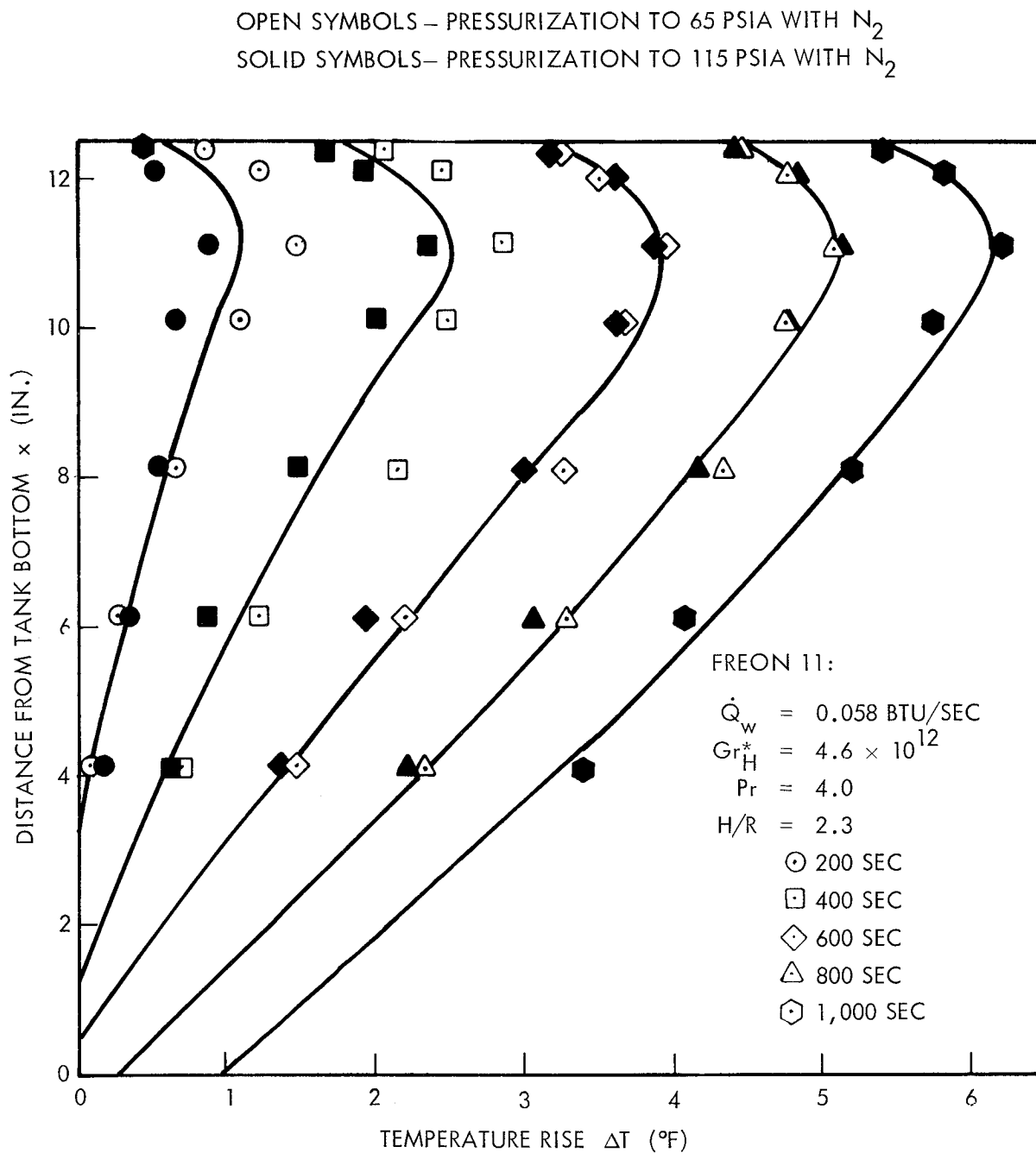
Fig. 5-2 Stratification Temperature Profiles for Subcooled Liquid
Calibration Tests

5.2.2 Experimental Results

The temperature profiles obtained from three runs with the same liquid heat rate but with increasing ullage heat rates are given in Figs. 5-3, 5-4, and 5-5. All three runs were performed under self-pressurizing conditions. The solid symbols at the liquid surface represent the saturation temperatures corresponding to the measured pressures. Figure 5-6 shows the measured pressure rise for these runs compared with the saturation pressure rise corresponding to the subcooled liquid surface temperature rise in the calibration run.

5.3 PRELIMINARY COMPARISON OF EXPERIMENTAL RESULTS WITH ANALYTICAL MODEL

The experimental results from Run UC-16 (Fig. 5-3) have been compared with predictions from the analytical model. As discussed previously, there are three parameters in the model which must be determined empirically: h_v, h_L, and I. Values of these parameters were selected which predicted the measured ullage pressure, temperature, and mass transfer. Since there is an infinite combination of parameters that will predict each of these quantities separately, the "correct" values of h_v, h_L, and I were considered to be those which simultaneously predicted the pressure rise and mass transfer with reasonable values of gas temperature. Less importance was attached to the predicted value of gas temperature because it had to be compared with the average experimental gas temperature. The volumetric average gas temperature was used for comparison because it differed only slightly from the mass average and was easier to compute.

Figure 5-7 compares the experimental results with predictions based on a vapor film heat-transfer coefficient h_v of 5×10^{-4} Btu/ft^2-sec-°F and a value for I of 0.65. This value of I was chosen in order to predict adequately the subcooled surface temperature rise. This value does not fit the correlation of I as a function of the modified Grashof number (Fig. 4-6) obtained for subcooled stratification. The appropriate

LOCKHEED MISSILES & SPACE COMPANY
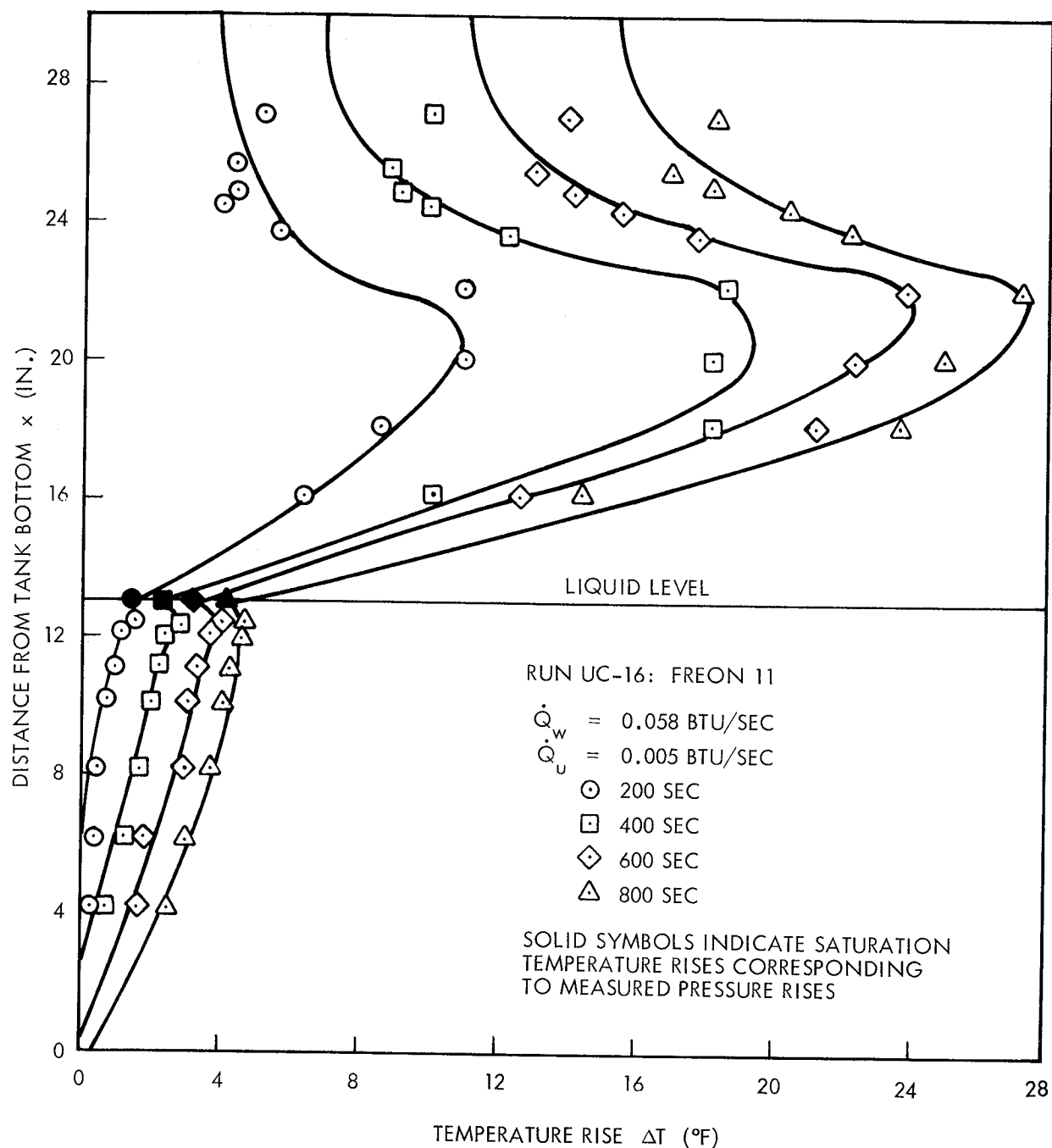
Fig. 5-3 Temperature Profiles for Stratification With Liquid-Ullage Coupling Under Self-Pressurizing Conditions – Run UC-16
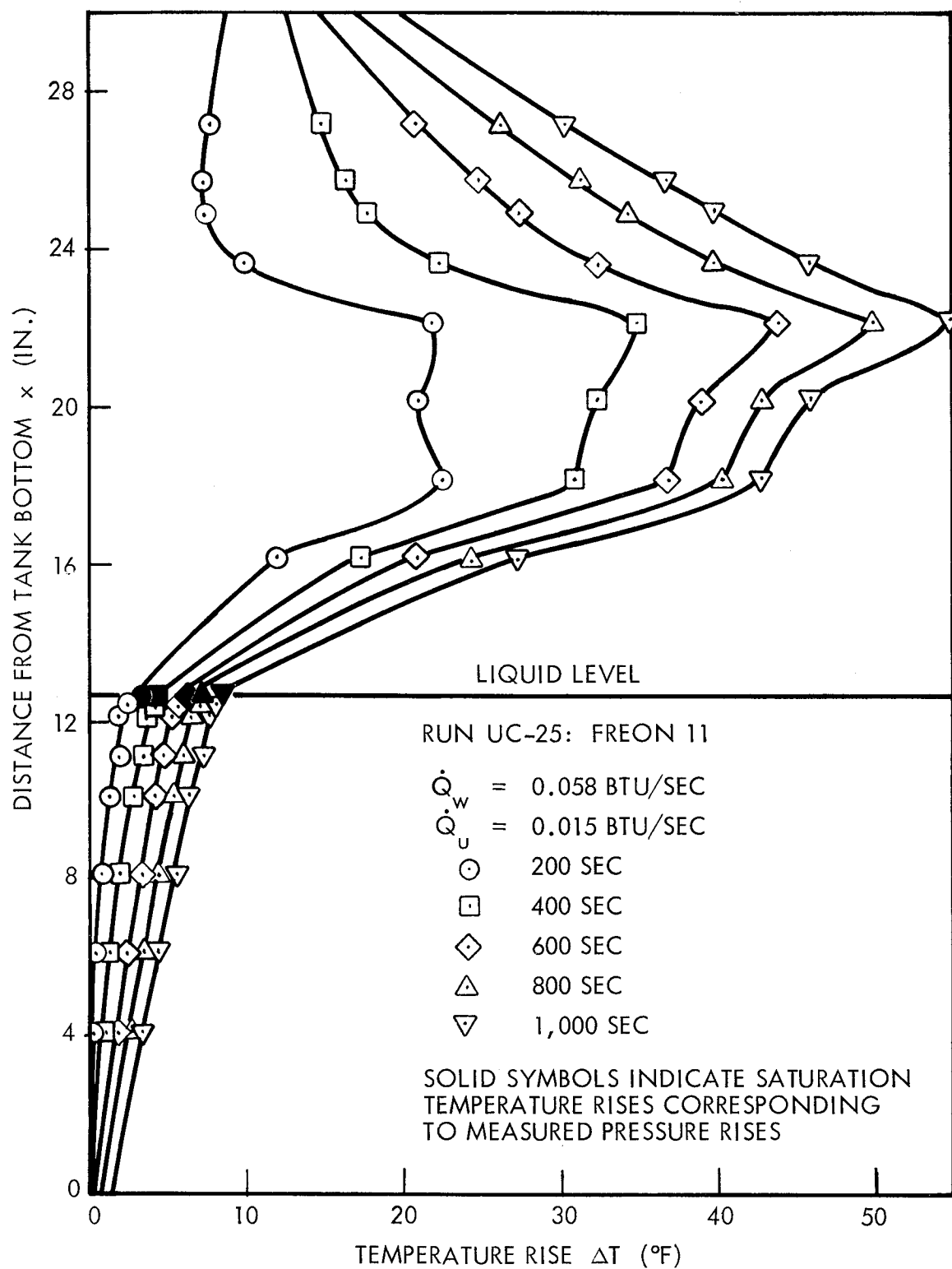
Fig. 5-4 Temperature Profiles for Stratification With Liquid-Ullage Coupling Under Self-Pressurizing Conditions – Run UC-25
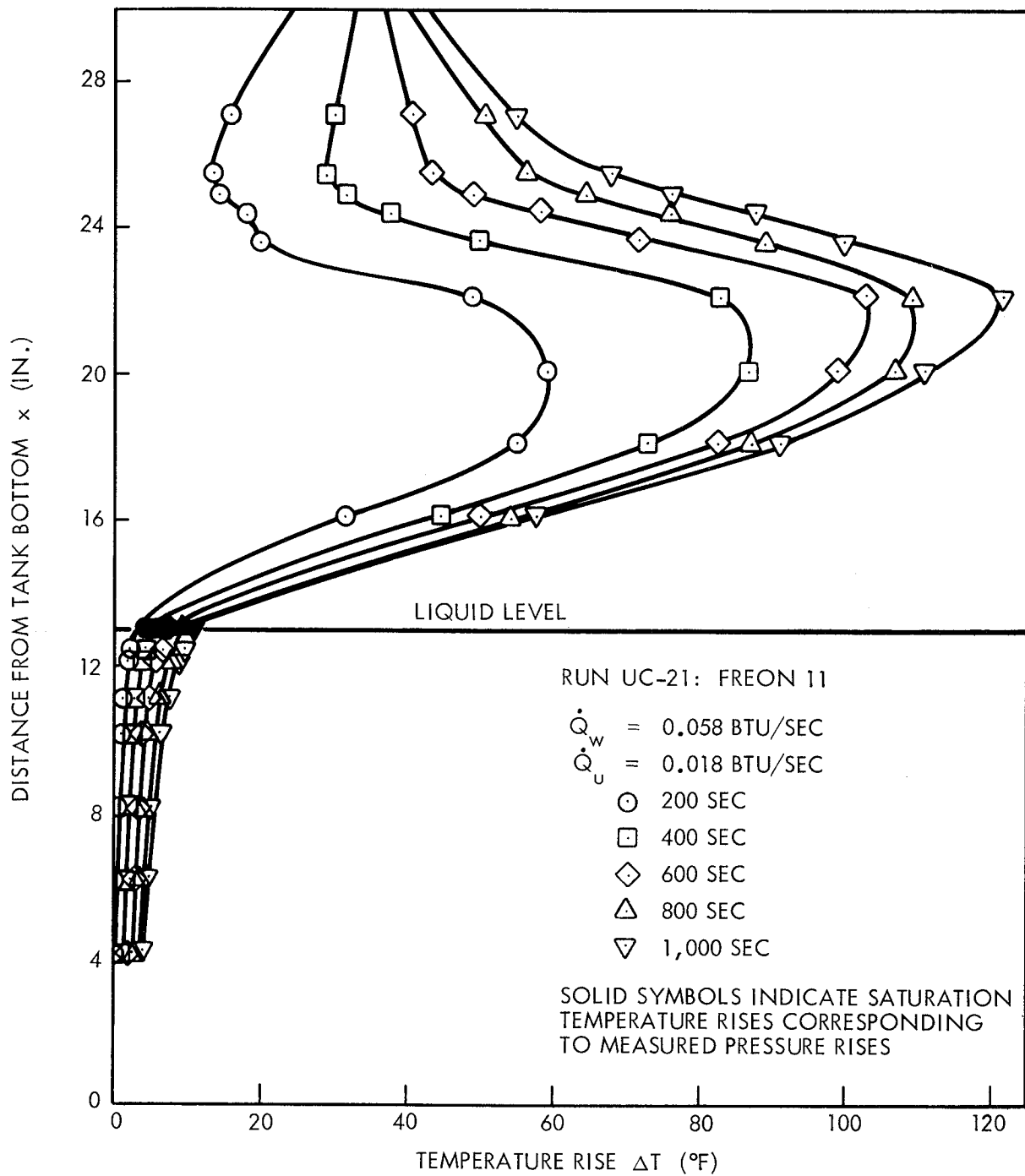
Fig. 5-5 Temperature Profiles for Stratification With Liquid-Ullage Coupling Under Self-Pressurizing Conditions — Run UC-21
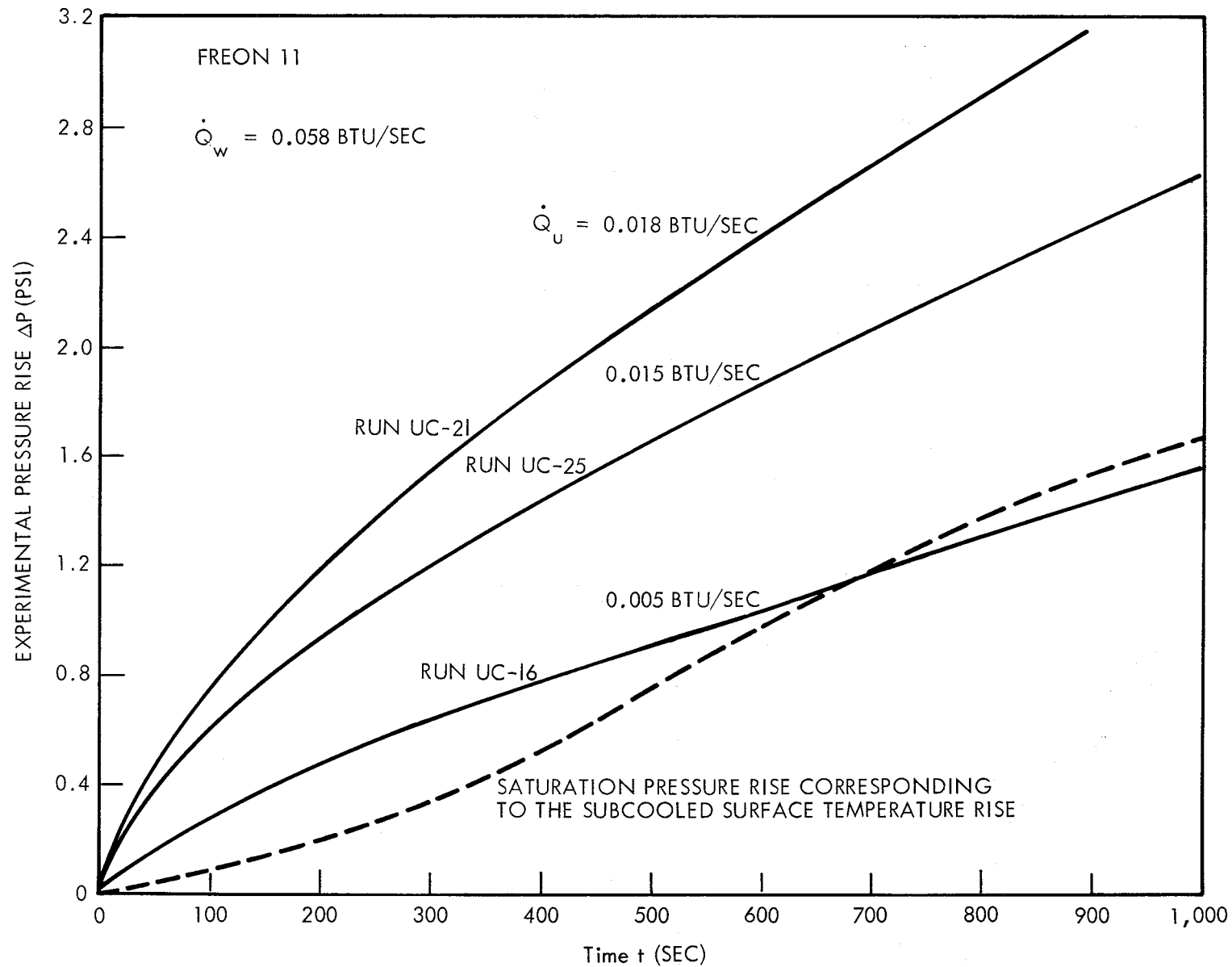
Fig. 5-6 Ullage Pressure Rise in Stratification With Liquid-Ullage
Coupling Experiments Under Self-Pressurizing Conditions

2-05-65-1
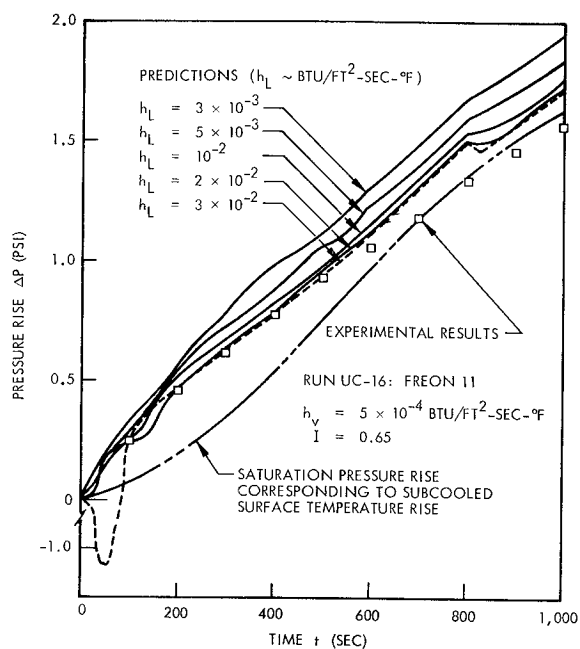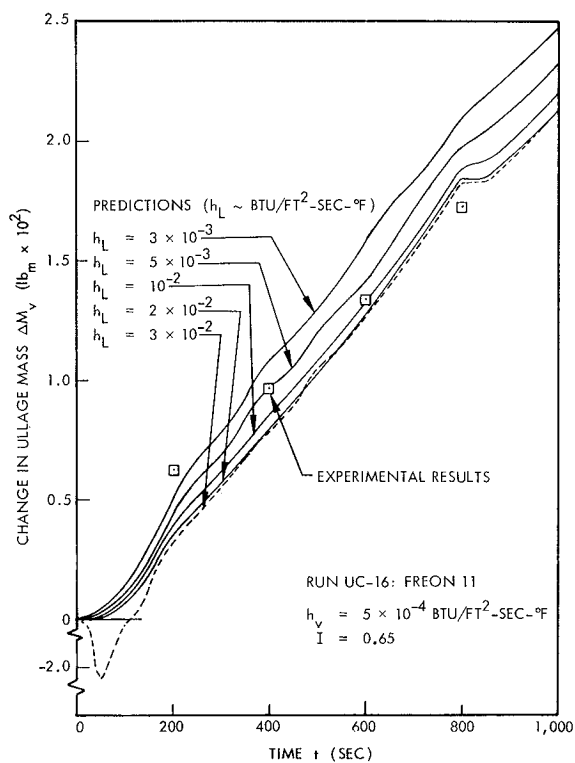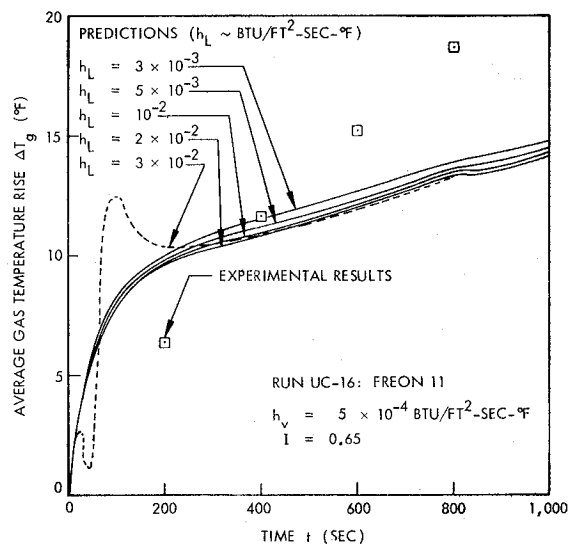
Fig. 5-7 Comparison of Experimental Results With Predictions
from Liquid-Ullage Coupling Model

value from this correlation would be 0.46, corresponding to a modified Grashof number of 4.6×10^{12}. This discrepancy is due to the double-valued temperature profiles obtained in the subcooled tests with Freon 11. However, for the purpose of examining the behavior of the liquid-ullage coupling model, a value of I was chosen which accurately predicts the subcooled surface temperature rise. The effect of I on the prediction will be discussed later. Figure 5-7a shows the pressure rise for values of h_L ranging from 3×10^{-3} to 3×10^{-2} Btu/ft^2-sec-° F. Values of h_L in excess of 2×10^{-2} produce negative pressure rises at early times and are therefore eliminated from consideration since this phenomenon was not observed experimentally. Figure 5-7b shows the mass transfer ΔM_v, where positive values correspond to evaporation at the interface. The condensation that occurs at early times for a value of $h_L = 3 \times 10^{-2}$ Btu/ft^2-sec-° F accounts for the decrease in pressure shown in Fig. 5-7a. The gas temperature is relatively insensitive to values of h_L below 2×10^{-2}, as shown in Fig. 5-7c. The discontinuities in the derivatives of the prediction curves at 800 sec are a result of the stratified layer reaching the tank bottom, which was taken to correspond to a stratified layer depth $\Delta/H = 0.95$.

Figure 5-8 compares the experimental results with predictions based on a liquid film heat transfer coefficient h_L of 5×10^{-3} Btu/ft^2-sec-° F and a value for I of 0.65. The pressure rise is insensitive to changes in the vapor film heat-transfer coefficient. This is because the mass transfer and the average gas temperature have a compensating effect on the pressure at a constant value of the liquid film coefficient.

The effect of I is shown in Fig. 5-9 for values of h_v and h_L of 5×10^{-4} and 5×10^{-3} Btu/ft^2-sec-° F respectively. The strong effect of I on the pressure rise is due in large part to the effect on mass transfer since the change in average gas temperature is not large. This effect is discussed further in the following paragraphs.

All the calculated results presented in Figs. 5-7 through 5-9 were computed with 160 time steps. The time step used, determined by trial, was considered to be sufficiently small. A minor smoothing effect was obtained by using 1,600 time steps, but it was not significant.

5-15
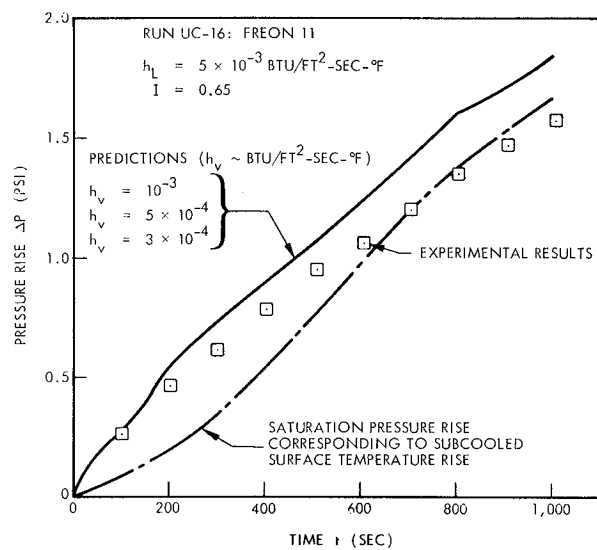
(a)
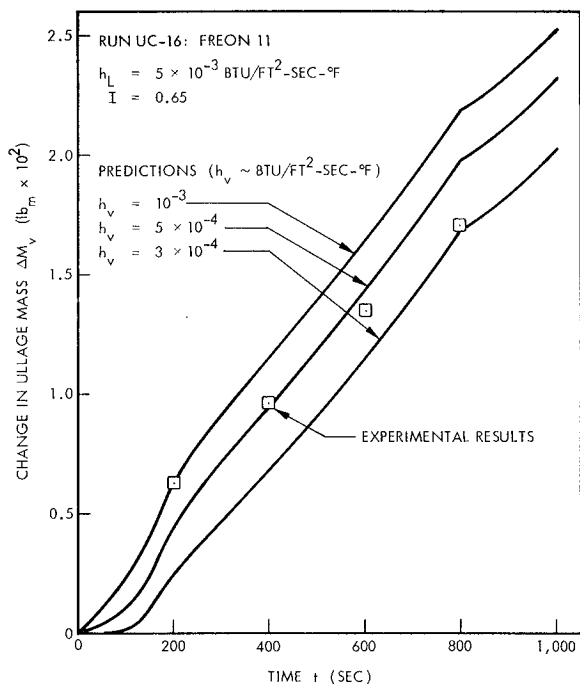
(b)
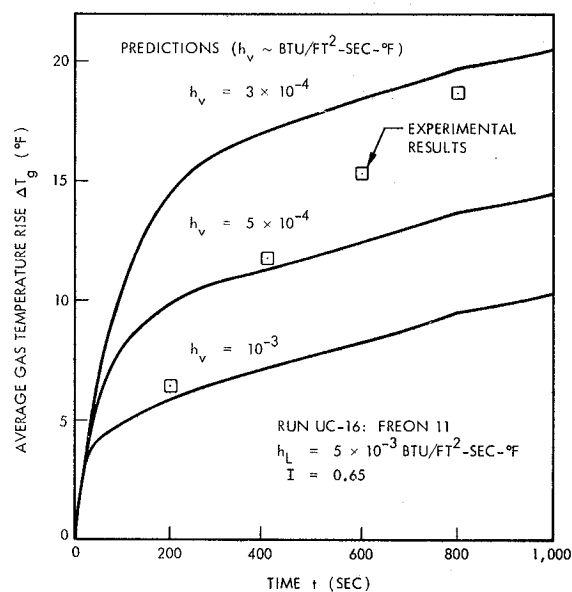
(c)

Fig. 5-8 Comparison of Experimental Results With Predictions
from Liquid-Ullage Coupling Model

5-16

(a)

(b)

(c)
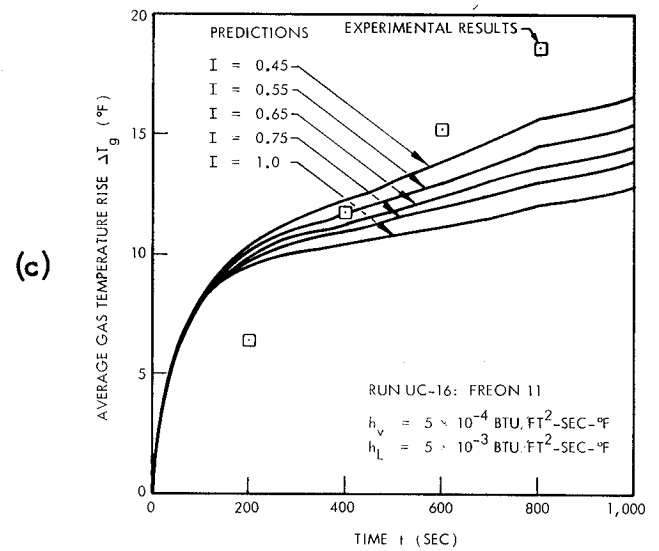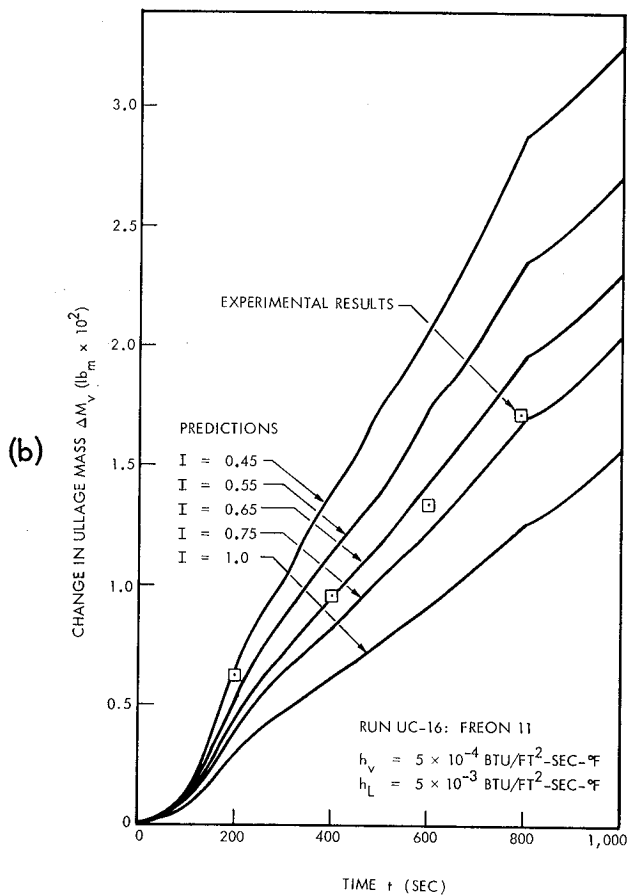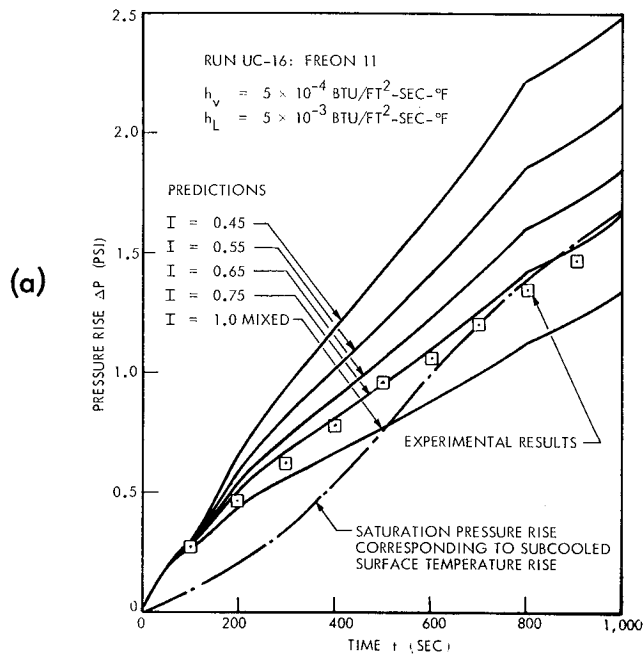
Fig. 5-9 Comparison of Experimental Results With Predictions from Liquid-Ullage Coupling Model

Mass transfer plays a relatively important role in the pressure rise in Run UC-16. In order to make this clear, the following approximate calculation will be helpful. If the ullage gas pressure is assumed to be a function of specific volume and temperature, the pressure rise may be expressed in approximate linearized form as

$$\Delta p \approx \left(\frac{\partial p}{\partial v}\right)_{T_0} \Delta v + \left(\frac{\partial p}{\partial T}\right)_{v_0} \Delta T_g \qquad (5.14)$$

The pressure rise may thus be approximated as

$$\Delta p \approx - \left(\frac{\partial p}{\partial v}\right)_{T_0} \frac{V}{M_{v,0}^2} (\Delta M_v) + \left(\frac{\partial p}{\partial T}\right)_{v_0} \Delta T_g \qquad (5.15)$$

where the first term is the contribution to the pressure rise from mass transfer. Figure 5-10 compares the magnitude of the two terms in Eq. (5.15) for Run UC-16. The mass transfer appears to account for about two-thirds of the pressure rise. The increase in pressure with decreasing value of I shown in Fig. 5-9 may therefore be attributed to the increase in mass transfer rather than the relatively small increase in gas temperature. In Run UC-16, the prediction of pressure rise is sensitive to values of the parameter I because of the large role played by mass transfer. The sensitivity of the pressure prediction to values of the parameter I depends, in general, on the values of the vapor film heat-transfer coefficient; e.g., increasing h_v with h_L fixed tends to increase the mass transfer. (See Fig. 5-8.) It remains to be seen whether or not the effect of I will remain significant at higher values of ullage heat rate, since the vapor film heat transfer coefficient will probably increase. The mass transfer may therefore be expected to increase over that for Run UC-16 at the same liquid heat rate. However, the gas temperature will also change due to changes in the ullage heat rate and h_v. The relative importance of mass transfer and I will probably change.

In general, these initial results are considered encouraging in that they support the approach based on the proposed liquid-ullage coupling model. Work is continuing on experiments to obtain data for a range of boundary conditions and fluid properties which will be used to evaluate the analytical model fully.
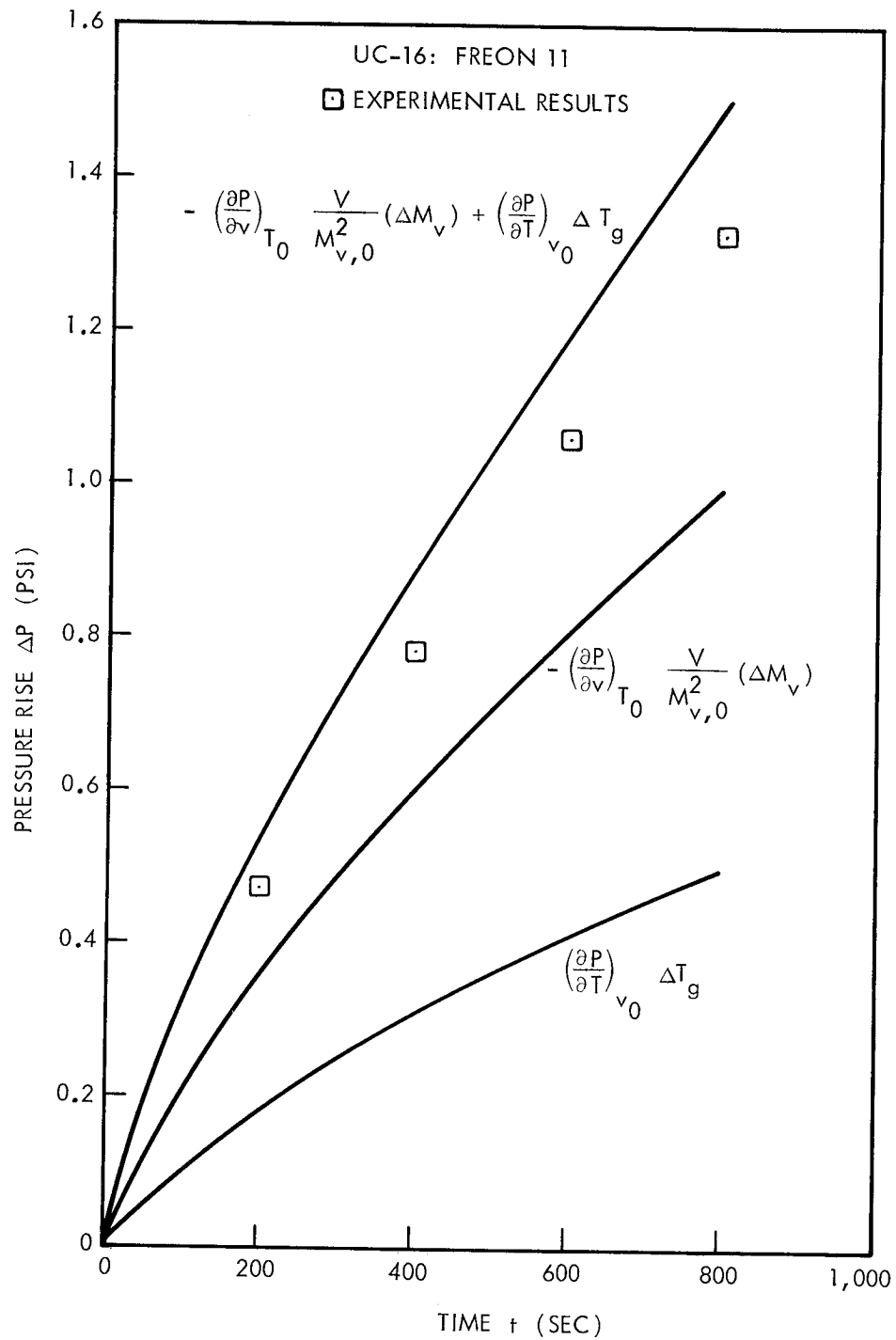
Fig. 5-10 Contribution of Mass Transfer to Total Pressure Rise
for Liquid-Ullage Coupling Run

LOCKHEED MISSILES & SPACE COMPANY

Section 6

NUCLEATE BOILING EFFECTS ON STRATIFICATION

When heat is transferred to a liquid in a container, the wall temperature may be sufficiently above the saturation temperature to result in nucleate boiling at the wall. In cryogenic propellant tanks, the liquid-side heat-transfer resistance is usually a small fraction of the total heat-transfer resistance, and the heat flux is, in effect, independent of the heat-transfer modes to the propellant. For a given heat flux under 1-g conditions, turbulent free convection may be the dominant mode of heat transfer to the propellant. As the g-level is reduced, the heat-transfer coefficient decreases and, since the heat flux is approximately constant, the wall temperature will increase. If boiling occurs, the vapor generated will modify the boundary-layer flow which, in turn, will affect stratification.

In this section, a solution obtained for a boiling free-convection boundary layer on a vertical flat plate is presented. The results of this solution are then used to determine the growth of the stratified layer.

Experiments have been conducted with water to obtain data on a boiling free-convection boundary layer and to evaluate the analysis. Preliminary experiments have also been conducted in the pressure vessel with Freon 11 to obtain stratification data, and these have been compared to predictions.

6.1 ANALYSIS

This analysis includes consideration of boundary-layer and stratification effects.

6.1.1 Boundary Layer Effects

The solution obtained for a boiling free-convection boundary layer on a vertical flat plate is based on a simple continuum analysis utilizing assumed boundary-layer profiles, the Reynolds analogy, and an empirical expression for the boiling heat-transfer coefficient. It is assumed that the wall heat flux is constant, that the bulk liquid is saturated, and that the fluid properties are constant (except for the buoyancy effect).

The steady flow momentum and energy integral boundary-layer equations are

$$\frac{d}{dx} \int_0^\delta \left[\rho_v u_v^2 \alpha + \rho_L u_L^2 (1 - \alpha) \right] dy + g \int_0^\delta \left[\rho_v \alpha + \rho_L (1 - \alpha) - \rho_\infty \right] dy + \tau_w = 0$$

$$(6.1)$$

$$\frac{d}{dx} \int_0^\delta \left[\rho_v u_v \alpha (\lambda + c_{p_v} \theta_v) + \rho_L u_L (1 - \alpha) c_{p_L} \theta_L \right] dy = q_w \qquad (6.2)$$

where α is the vapor fraction defined by

$$\alpha = (m_v / \rho_v) / \left[(m_v / \rho_v) + (m_L / \rho_L) \right] \qquad (6.3)$$

and the other symbols are defined in the nomenclature.

A vapor distribution through the boundary layer will be assumed

$$\alpha = \alpha_0 f \left(\frac{y}{\delta} \right) \qquad (6.4)$$

and an average vapor or void fraction is defined as

$$\bar{\alpha} = \frac{\alpha_0}{\delta} \int_0^\delta f\left(\frac{y}{\delta}\right) dy \qquad (6.5)$$

A dimensionless density ratio ρ^* and slip velocity u^* are introduced

$$\rho^* = \frac{\rho_v}{\rho_L}$$

$$u^* = \frac{u_v}{u_L} \qquad (6.6)$$

The boundary-layer equations become

$$\frac{d}{dx} \int_0^\delta u_L^2 \left[\rho^* u^{*2} \alpha + (1 - \alpha)\right] dy + g \int_0^\delta \left[\alpha(\rho^* - 1) - \frac{\rho_\infty}{\rho_L} \beta \theta_L\right] dy + \frac{\tau_w}{\rho_L} = 0$$

$$(6.7)$$

$$\frac{d}{dx} \int_0^\delta \rho_L u_L \left[\rho^* u^* \alpha \lambda + (1 - \alpha) c_{p_L} \theta_L\right] dy = q_w \qquad (6.8)$$

where

$$\beta = - \frac{\rho_L - \rho_\infty}{\rho_\infty \theta_L}$$

and it is assumed that

$$\lambda \gg c_{p_v} \theta_v$$

The velocity and temperature profiles are taken to be those of Ref. 7 for a turbulent free-convection boundary layer given by

$$u_L = u_1 \left(\frac{y}{\delta}\right)^{1/7} \left(1 - \frac{y}{\delta}\right)^4$$

$$\theta_L = \theta_S \left[1 - \left(\frac{y}{\delta}\right)^{1/7}\right] \tag{6.9}$$

The Reynolds analogy is introduced as

$$\tau_w = \frac{h u_1}{c_{p_L}} \tag{6.10}$$

where

$$h = \frac{q_w}{\theta_S} \tag{6.11}$$

Assuming first that the vapor distribution through the boundary layer is uniform

$$\alpha = \alpha_o = \bar{\alpha} \tag{6.12}$$

the boundary-layer equations become

$$0.0521 \left[\rho^* u^{*2} \bar{\alpha} + (1 - \bar{\alpha})\right] \frac{d}{dx} \left(u_1^2 \delta\right) - g \left[\bar{\alpha} (1 - \rho^*) + 0.125 \frac{\beta q_w}{h}\right] \delta + \frac{h}{\rho_L c_{p_L}} u_1 = 0$$

$$\tag{6.13}$$

6-4

$$\rho_L \left[\frac{0.146\rho^* u^* \overline{\alpha} \lambda}{q_w} + \frac{0.0366 (1 - \overline{\alpha}) c_{p_L}}{h} \right] \frac{d}{dx} (u_1 \delta) = 1 \qquad (6.14)$$

with $\rho_\infty / \rho_L \approx 1$

The solution of these equations is

$$\frac{u_1}{x^{1/2}} = \left[\frac{0.115 (1 - \overline{\alpha}) + \dfrac{0.146 \rho^* u^* \overline{\alpha} \lambda h}{q_w c_{p_L}}}{g \overline{\alpha} (1 - \rho^*) + \dfrac{0.125 g q_w \beta}{h}} \right]^{-1/2} \qquad (6.15)$$

$$\frac{\delta}{x^{1/2}} = \frac{\left[\dfrac{0.115 (1 - \overline{\alpha}) + \dfrac{0.146 \rho^* u^* \overline{\alpha} \lambda h}{q_w c_{p_L}}}{g \overline{\alpha} (1 - \rho^*) + \dfrac{0.125 g q_w \beta}{h}} \right]^{1/2}}{\rho_L \left[\dfrac{0.146 \rho^* u^* \overline{\alpha} \lambda}{q_w} + \dfrac{0.0366 (1 - \overline{\alpha}) c_{p_L}}{h} \right]} \qquad (6.16)$$

The boundary-layer mass flow rate per unit width is given by

$$\dot{m}_{BL} = \int_0^\delta \left[\rho_L u_L (1 - \alpha) + \rho_v u_v \alpha \right] dy$$

$$= \int_0^\delta \rho_L u_L \left[(1 - \alpha) + \rho^* u^* \alpha \right] dy \qquad (6.17)$$

If it is assumed that $\rho^* u^* \alpha \ll (1 - \alpha)$, the mass flow rate becomes

$$\dot{m}_{BL} = \int_0^\delta \rho_L u_L (1 - \alpha) \, dy \qquad (6.18)$$

This may be evaluated with Eqs. (6.9), (6.15), and (6.16) for a uniform vapor distribution

$$\frac{\dot{m}_{BL}}{x} = \frac{\dfrac{4h}{c_{p_L}}}{\left(\dfrac{\rho^* u^* \bar{\alpha}}{1 - \bar{\alpha}}\right) \left(\dfrac{4\lambda h}{q_w c_{p_L}}\right) + 1} \tag{6.19}$$

The average liquid velocity is defined as

$$u_{ave} = \frac{\dot{m}_{BL}}{\rho_L (1 - \bar{\alpha}) \delta}$$

$$= \frac{\displaystyle\int_0^1 u_L (1 - \alpha) \, d\left(\frac{y}{\delta}\right)}{\displaystyle\int_0^1 (1 - \alpha) \, d\left(\frac{y}{\delta}\right)} \tag{6.20}$$

With a uniform vapor distribution, this becomes

$$u_{ave} = 0.146 \, u_1 \tag{6.21}$$

The energy that goes into vaporization is given by

$$\frac{q_{vap}}{q_w} = \frac{\lambda}{q_w} \frac{d}{dx} \int_0^\delta \rho_v u_v \alpha \, dy$$

$$\simeq \frac{1}{1 + \left(\dfrac{1 - \bar{\alpha}}{\rho^* u^* \bar{\alpha}}\right)\left(\dfrac{q_w c_{p_L}}{4\lambda h}\right)} \tag{6.22}$$

The relative buoyant effects of liquid heating and vaporization on the characteristic velocity and boundary layer thickness may be seen from Eqs. (6.15) and (6.16) by comparing the magnitudes of the terms

$$g \bar{\alpha} (1 - \rho^*) \quad \text{and} \quad \frac{0.125 \, g \, q_w \beta}{h}$$

The first term represents the effect of vapor while the second term represents the effect of changes in liquid density. The second term is generally of a lower order of magnitude than the first. The contribution to buoyancy of changes in liquid density due to temperature variations therefore was assumed to be negligible compared to the effect of phase change when considering other, nonuniform, vapor distributions. This assumption implies that liquid motion in the boundary layer is a result of viscous drag by the rising vapor bubbles. The slip velocity u^* is indicative of the momentum exchange between the two; a value of $u^* = 1$ implies maximum momentum exchange.

In order to determine the effect of vapor distribution on the results of this analysis, two other distributions will be considered which are given by

$$\alpha = 2 \bar{\alpha} (1 - \frac{y}{\delta}) \tag{6.23}$$

$$\alpha = 8 \bar{\alpha} \left[1 - (\frac{y}{\delta})^{1/7} \right] \tag{6.24}$$

Again with the restriction that $\rho^* u^* \alpha << (1 - \alpha)$ the boundary-layer mass flow is

$$\frac{\dot{m}_{BL}}{x} = \frac{(1 - 1.63 \bar{\alpha}) \frac{4h}{c_{p_L}}}{\frac{6.5 \, \rho^* u^* \bar{\alpha} \lambda h}{q_w c_{p_L}} - 0.688 \, \bar{\alpha} + 1} \tag{6.25}$$

for the vapor distribution of Eq. (6.23) and

$$\frac{\dot{m}_{BL}}{x} = \frac{(1 - 2\bar{\alpha})\, c_{p_L} \dfrac{4h}{}}{\dfrac{8\rho^* u^* \bar{\alpha}\, \lambda h}{q_w\, c_{p_L}} - 2.4\,\bar{\alpha} + 1} \qquad (6.26)$$

for the vapor distribution of Eq. (6.24).

The equations for the boundary-layer thickness and average velocity are

$$\frac{\delta}{x^{1/2}} = \frac{\dfrac{h}{\rho_L\, c_{p_L}} \left\{ \dfrac{0.5}{g\,\bar{\alpha}(1-\rho^*)} \left[0.274\rho^* u^{*2}\bar{\alpha} + 0.476\,\rho^* u^*\,\bar{\alpha}\,\dfrac{\lambda h}{q_w\, c_{p_L}} - 0.324\bar{\alpha} + 0.230 \right] \right\}^{1/2}}{\left[0.238\,\rho^* u^*\,\bar{\alpha}\,\dfrac{\lambda h}{q_w\, c_{p_L}} - 0.252\,\bar{\alpha} + 0.0366 \right]}$$

$$(6.27)$$

$$\frac{u_{ave}}{x^{1/2}} = \frac{\left(\dfrac{0.146 - 0.238\,\bar{\alpha}}{1 - \bar{\alpha}} \right)}{\left\{ \dfrac{0.5}{g\,\bar{\alpha}(1-\rho^*)} \left[0.274\,\rho^* u^{*2}\,\bar{\alpha} + 0.476\rho^* u^*\,\bar{\alpha}\,\dfrac{\lambda h}{q_w\, c_{p_L}} - 0.324\,\bar{\alpha} + 0.230 \right] \right\}^{1/2}}$$

$$(6.28)$$

6-8

for the vapor distribution of Eq. (6.23), and

$$\frac{\delta}{x^{1/2}} =$$

$$\frac{\dfrac{h}{\rho_L c_{p_L}} \left\{ \dfrac{1}{g\bar{\alpha}(1-\rho^*)} \left[0.180\rho^* u^{*2} \bar{\alpha} + 0.293\rho^* u^* \bar{\alpha} \dfrac{\lambda h}{q_w c_{p_L}} - 0.268\bar{\alpha} + 0.115 \right] \right\}^{1/2}}{\left[0.293\rho^* u^* \bar{\alpha} \dfrac{\lambda h}{q_w c_{p_L}} - 0.0878\bar{\alpha} + 0.0366 \right]}$$

$$(6.29)$$

$$\frac{u_{ave}}{x^{1/2}} =$$

$$\frac{\left(\dfrac{0.146 - 0.293\bar{\alpha}}{1 - \bar{\alpha}} \right)}{\left\{ \dfrac{1}{g\bar{\alpha}(1-\rho^*)} \left[0.180\rho^* u^{*2} \bar{\alpha} + 0.293\rho^* u^* \bar{\alpha} \dfrac{\lambda h}{q_w c_{p_L}} - 0.268\bar{\alpha} + 0.115 \right] \right\}^{1/2}}$$

$$(6.30)$$

for the vapor distribution of Eq. (6.24).

In order to apply the foregoing results, it is necessary to employ an experimentally determined value of the boiling heat-transfer coefficient h and estimate the slip velocity u^* and vapor fraction $\bar{\alpha}$. The general effect of u^* and $\bar{\alpha}$ on the mass flow rate may be seen from Eq. (6.19) for a uniform vapor distribution. It has been assumed in the analysis that

$$\frac{\rho^* u^* \bar{\alpha}}{1 - \bar{\alpha}} \ll 1$$

In general, the assumption allows for large slip velocities since both ρ^* and $\bar{\alpha}$ are small. The combined effect of slip velocity and vapor fraction is significant only if the quantity $4\lambda h / q_w c_{p_L}$ is large. If the quantity $4\lambda h / q_w c_{p_L}$ is not large, so that

$$\left(\frac{\rho^* u^* \bar{\alpha}}{1 - \bar{\alpha}} \right) \left(\frac{4\lambda h}{q_w c_{p_L}} \right) \ll 1$$

the mass flow rate approaches the limiting value

$$\frac{\dot{m}_{BL}}{x} = \frac{4h}{c_{p_L}} \tag{6.31}$$

The use of Eq. (6.31) is not generally valid. Consider, for example, the case of liquid hydrogen. The boiling curves in Fig. 7-5 indicate that for

$$q_W = 1,000 \text{ Btu/ft}^2\text{-hr}$$

then

$$h = 500 \text{ Btu/ft}^2\text{-hr}$$

With

$$\lambda = 190 \text{ Btu/lb}_m$$

$$c_{p_L} = 2.5 \text{ Btu/lb}_m - {}^\circ F$$

$$\rho^* = 2 \times 10^{-2}$$

and estimating

$$\bar{\alpha} \approx 5 \times 10^{-2}$$

$$u^* \approx 5$$

6-10

gives

$$\left(\frac{\rho^* u^* \bar{\alpha}}{1 - \bar{\alpha}}\right) \left(\frac{4 \lambda h}{q_w c_{p_L}}\right) \approx (5.3 \times 10^{-3})(150) \approx 0.8$$

Thus, the use of Eq. (6.31) for liquid hydrogen could predict a mass flow rate which is high by a factor of almost two.

6.1.2 Stratification Effects

The results of the boundary layer analysis may be used to determine the growth of the stratified layer under boiling conditions at the wall. The mass flow in the boundary layer at the bottom of the stratified layer is equal to the rate of change of mass in the stratified layer. This may be expressed (Ref. 1) as

$$\pi R^2 \rho_L \frac{d\Delta}{dt} = 2 \pi R \dot{m}_{BL} \tag{6.32}$$

Substituting the value of boundary-layer mass flow for a uniform vapor distribution from Eq. (6.19) and integrating, gives

$$\frac{\Delta}{H} = 1 - \exp\left[-\frac{\dfrac{8 ht}{R \rho_L c_{p_L}}}{\left(\dfrac{\rho^* u^* \bar{\alpha}}{1 - \bar{\alpha}}\right)\left(\dfrac{4 \lambda h}{q_w c_{p_L}}\right) + 1}\right] \tag{6.33}$$

If

$$\left(\frac{\rho^* u^* \bar{\alpha}}{1 - \bar{\alpha}}\right)\left(\frac{4 \lambda h}{q_w c_{p_L}}\right) << 1$$

Equation (6.33) reduces to

$$\frac{\Delta}{H} = 1 - \exp\left(-\frac{8\ ht}{R\rho_L c_{p_L}}\right)$$ (6.34)

With the growth of the stratified layer established, it is possible to evaluate the surface temperature rise by Eq. (2.4). However, the effect that boiling in the boundary layer at the wall will have on the energy integral remains to be determined.

6.2 EXPERIMENTS

Experiments were conducted to verify the results of the analytical effort with respect to boundary-layer and stratification effects.

6.2.1 Boundary-Layer Effects

In order to verify the validity of the boiling boundary-layer solution, experiments were conducted in a two-dimensional tank with saturated water at one atmosphere. The tank, shown in Fig. 6-1, was 18 in. high, 12 in. wide, and 6 in. deep. It was constructed with transparent walls.

The heated plate, mounted vertically at one end of the tank, was 8 in. high by 6 in. wide and consisted of 1-mil, stainless-steel, shim stock bonded to a phenolic insulating plate for support. A heat flux of known value was imposed by applying direct current through the shim stock. The liquid depth was maintained at approximately 12 in. (4 in. above the top of the plate), and a series of screens in the top 4 in. of water prevented the flow field near the plate from being affected by the surface spreading. A rake which emitted dye in individual particles at various depths was mounted about 3 in. from the plate.

Motion pictures of the dye particles as they progressed from the rake toward the boundary layer were taken at 24 frames/sec. The normal and tangential velocity
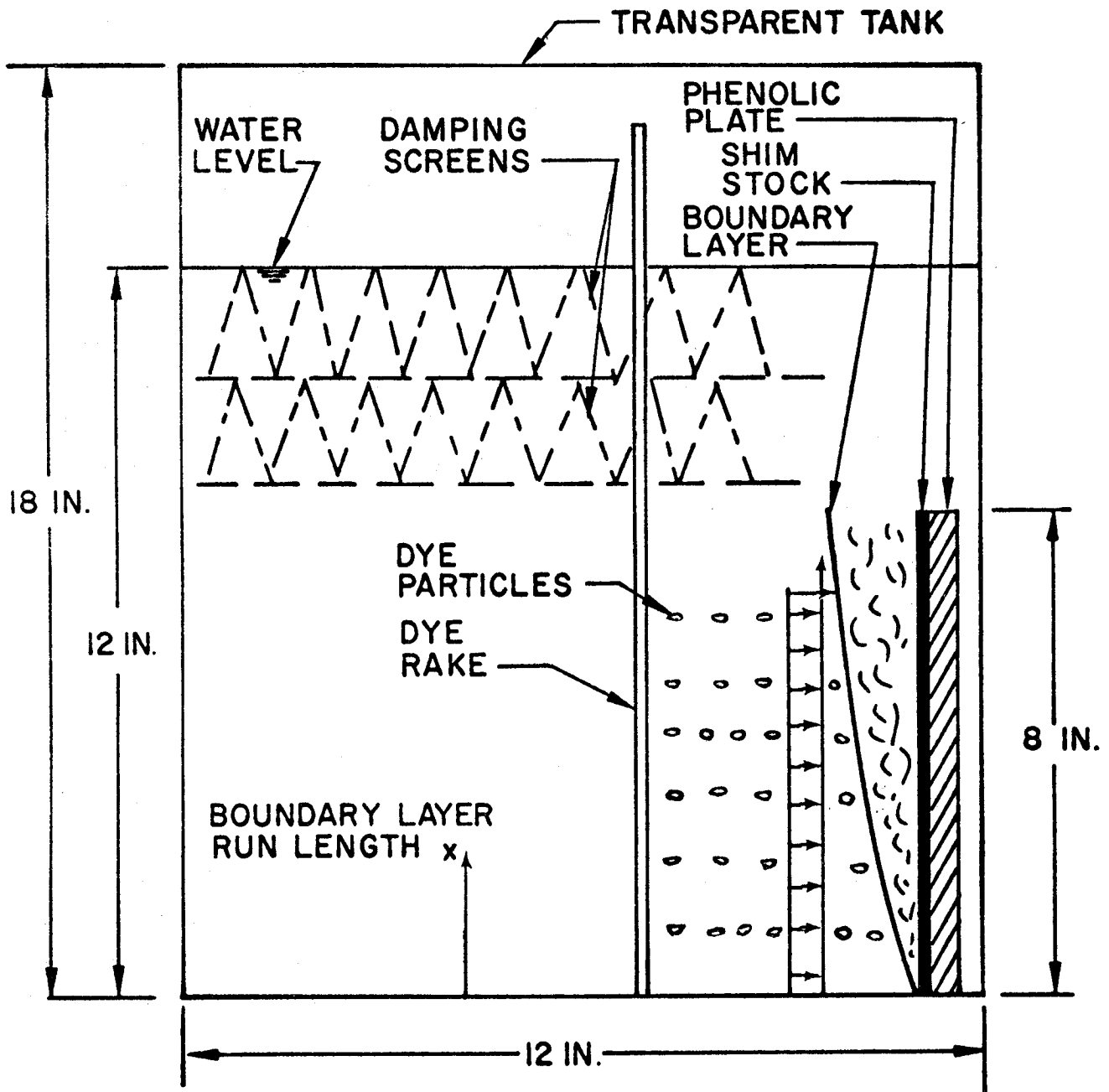
Fig. 6-1 Two-Dimensional Tank Used for Boiling, Free-Convection, Boundary-Layer Experiments

6-13

components approaching the edge of the boundary layer were determined, as a function of run length, by means of a film reader. The boundary-layer mass flow rate was determined by continuity. At a given vertical location, a rectangular control volume was considered, and the experimentally determined normal velocity component was integrated. The tangential velocity distribution between the upper left-hand corner of the control volume and the edge of the boundary layer was approximated as linear; this contribution to the total mass flow was very small. The edge of the boundary layer was clearly defined by the rapid disappearance of the dye particles as they entered the boundary layer.

In order to determine the accuracy of the experimental method, nonboiling tests were run with 150°F water at a heat flux of 2 Btu/ft^2-sec. The experimentally determined boundary layer mass flow is compared in Fig. 6-2 with a prediction obtained from the similarity solution of Sparrow and Gregg for the laminar free-convection boundary layer (Ref. 8). The prediction equation

$$\dot{m}_{BL} = 1.58 \, \mu \, \frac{Gr^*_x{}^{1/5}}{Pr^{0.388}} \tag{6.35}$$

was obtained from the numerical integration of the similarity equations and by curve-fitting the results over a range of Prandtl numbers from 1 to 30. The nonboiling data points correspond to run lengths of 0.14, 0.29, and 0.38 ft. Although the transition run length, corresponding to a value of $Gr_x \, Pr = 10^9$, was calculated to be 0.2 ft, the agreement with the prediction is good. Figure 6-2 also shows the boiling results, obtained at an ambient temperature of 212°F and a wall heat flux of 2 Btu/ft^2-sec. The run lengths are 0.1, 0.2, 0.3, and 0.4 ft. The strong effect of boiling on the boundary-layer mass flow rate is clear.

In order to estimate the value of $\bar{\alpha}$, still pictures were taken normal to the plate surface with an exposure time of 1/1,000 sec. The vapor fraction $\bar{\alpha}$ was determined to be approximately 0.017 by counting the bubble number density per unit plate area and measuring the bubble diameters.
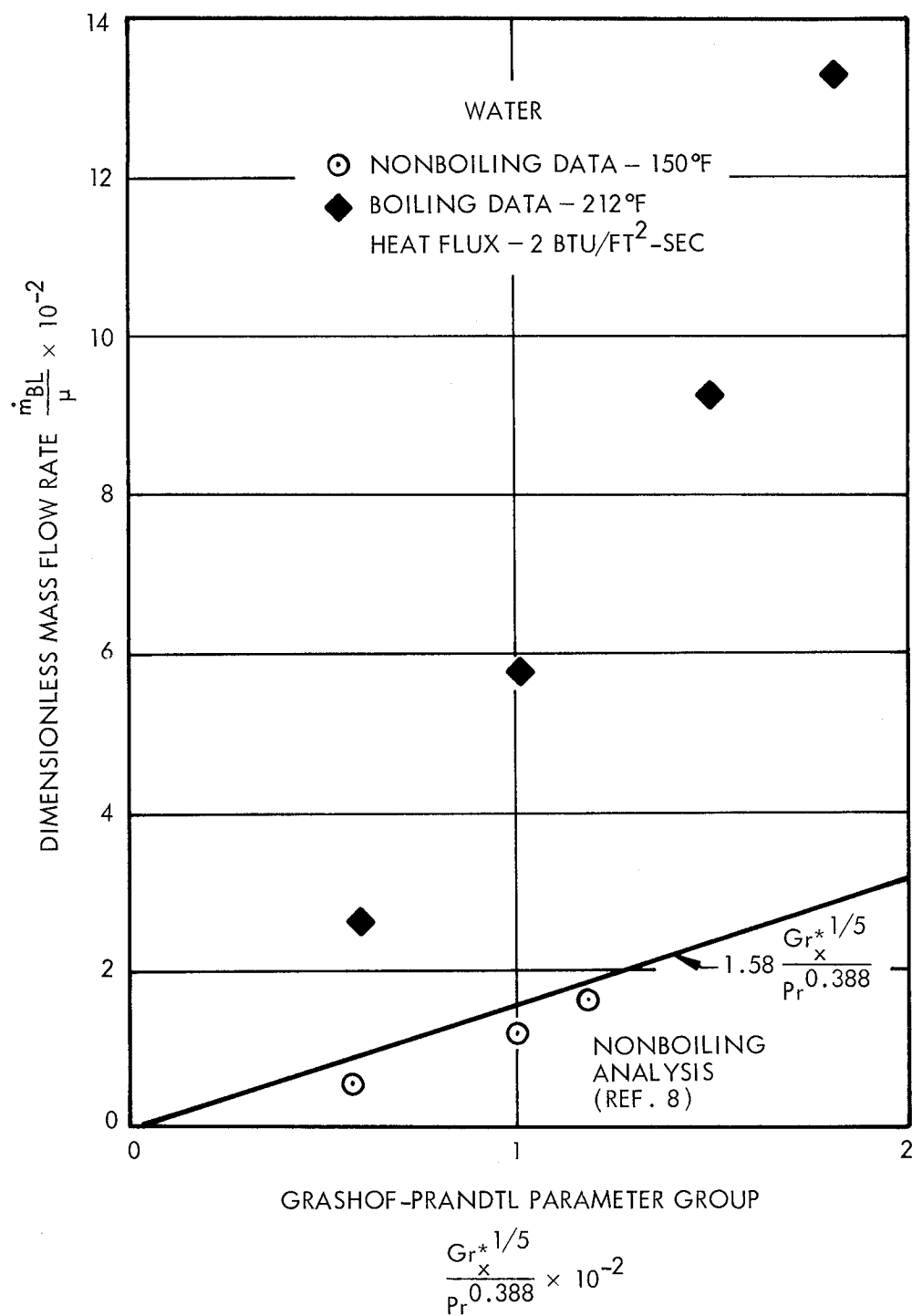
Fig. 6-2 Experimental Results for Free-Convection, Boundary-Layer
Mass Flow Rate

Motion pictures taken normal to the plate surface at 500 frames/sec indicated that the absolute bubble velocity varied between 0.5 and 0.8 ft/sec. A maximum liquid velocity was calculated using the experimentally determined average velocity and a 1/7th-power velocity profile. The vapor velocity was only slightly in excess of the calculated maximum liquid velocity, indicating a large momentum exchange and a small slip velocity; that is, u* is of the order of one.

The boiling boundary-layer equations were evaluated using water properties at 212°F and a heat flux of 2 Btu/ft^2-sec. A value for the heat transfer coefficient was determined by the method of Rohsenow (Ref. 9) to be 0.125 Btu/ft^2-sec-$^{\circ}$F. Figure 6-3 shows the effect of vapor distribution and slip velocity on the mass flow rate predicted by the boiling analysis. With the measured values of $\bar{\alpha}$ and u*

$$\left(\frac{\rho^* \, u^* \, \bar{\alpha}}{1 - \bar{\alpha}} \right) \left(\frac{4 \lambda h}{q_w \, c_{p_L}} \right) = (1.1 \times 10^{-5})(242) = 0.003$$

The mass flow rate, therefore, is that given by Eq. (6.31).

Figure 6-4 shows the experimental results for boundary-layer mass flow rate compared with the boiling prediction. The nonboiling predictions of Refs. 8 and 10 up to x = 0.4 ft — twice the transition run length — are also shown. The analysis of Ref. 10 is based on a solution of the integral laminar free-convection boundary-layer equations. The boiling prediction shown is for a value of u* between 1 and 10 and for the measured vapor fraction with a uniform distribution. Inspection of Fig. 6-3 indicates that at this vapor fraction the predicted mass flow is relatively insensitive to vapor distribution and slip velocity over a reasonable range.

Figure 6-5 compares the experimentally determined boiling boundary-layer thickness with the nonboiling prediction of Ref. 10 and the boiling prediction with a uniform vapor distribution.
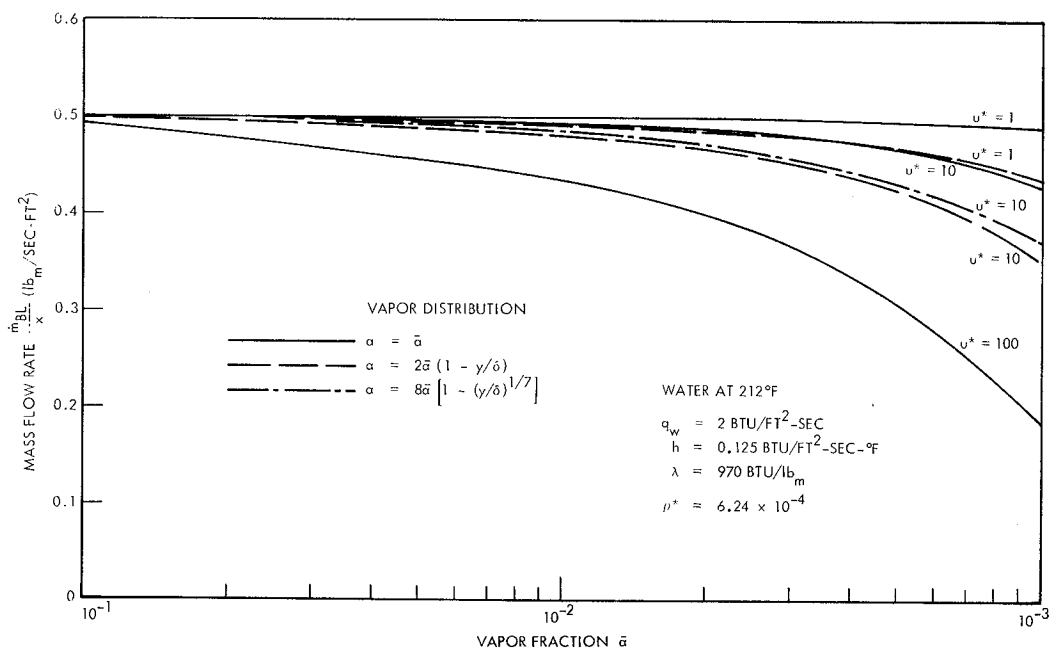
Fig. 6-3 Mass Flow Rate Predicted by Boiling, Free-Convection, Boundary-Layer
Analysis
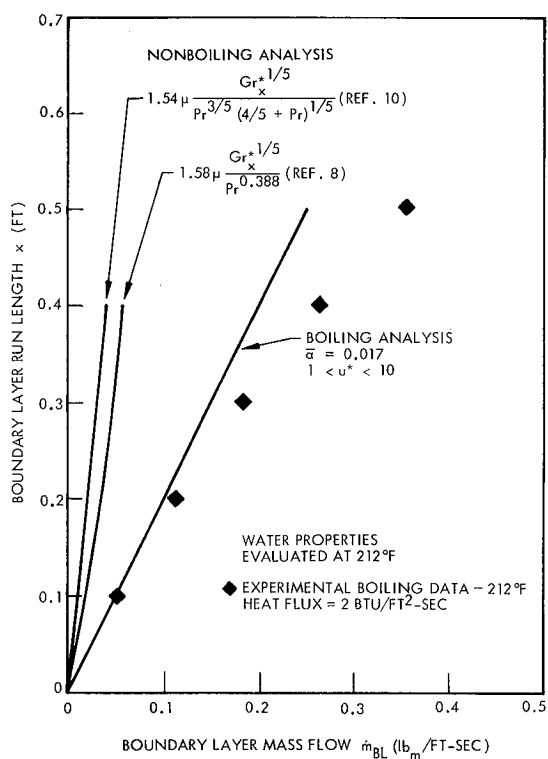
Fig. 6-4 Comparison of Experimental
Results With Predictions for
Boiling, Free-Convection,
Boundary-Layer Mass Flow
Rate

Fig. 6-5 Comparison of Experimental
Results With Predictions for
Boiling, Free-Convection,
Boundary-Layer Thickness

LOCKHEED MISSILES & SPACE COMPANY
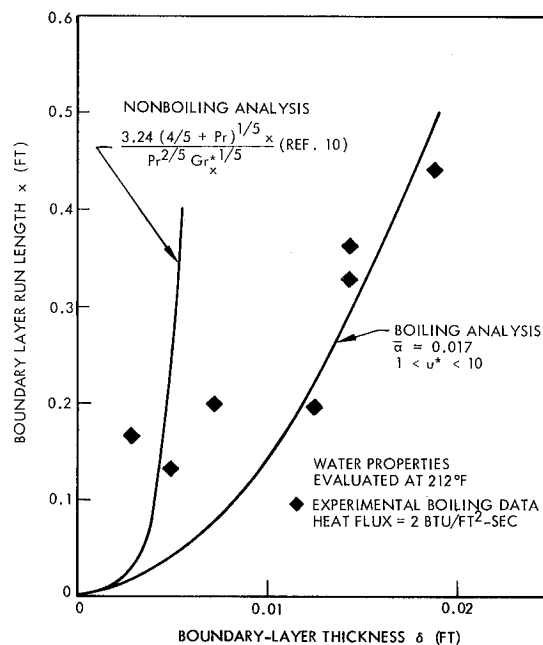
Figure 6-6 shows the experimental average liquid velocity which was determined using the measured mass flow rate and approximating the experimental boundary-layer thickness as $\delta = 0.043\, x$. The assumed linear dependence of δ on x was used because a parabolic dependence could not be justified on the basis of the data shown in Fig. 6-5. The nonboiling prediction of Ref. 10 is shown in Fig. 6-6 together with the boiling prediction for a uniform vapor distribution.

The calculated boundary-layer thickness and average velocity for the three assumed vapor distributions are shown in Table 6-1. The results indicate that both the boundary layer thickness and average velocity are insensitive to vapor distribution.

Table 6-1

PREDICTED BOILING BOUNDARY-LAYER
THICKNESS AND AVERAGE VELOCITY

Vapor Distribution	Boundary-Layer Thickness	Boundary-Layer Average Velocity
α	$\delta / x^{1/2}$	$u_{ave} / x^{1/2}$
$-$	$ft^{1/2}$	$ft^{1/2}/sec$
$\bar{\alpha}$	0.0265	0.321
$2\,\bar{\alpha}\,(1 - \frac{y}{\delta})$	0.0281	0.319
$8\,\bar{\alpha}\left[1 - (\frac{y}{\delta})^{1/7}\right]$	0.0256	0.313

Note: $\bar{\alpha} = 0.017$; $1 < u^* < 10$; $q_w = 2$ Btu/ft^2-sec; $h = 0.125$ Btu/ft^2-sec-°F

From the results presented, it may be concluded that the effect of vapor bubbles in a free-convection boundary layer is to increase the mass flow rate, the boundary-layer thickness, and the average velocity at the same values of the liquid modified Grashof and Prandtl numbers. This is due to the increase momentum imparted to the liquid
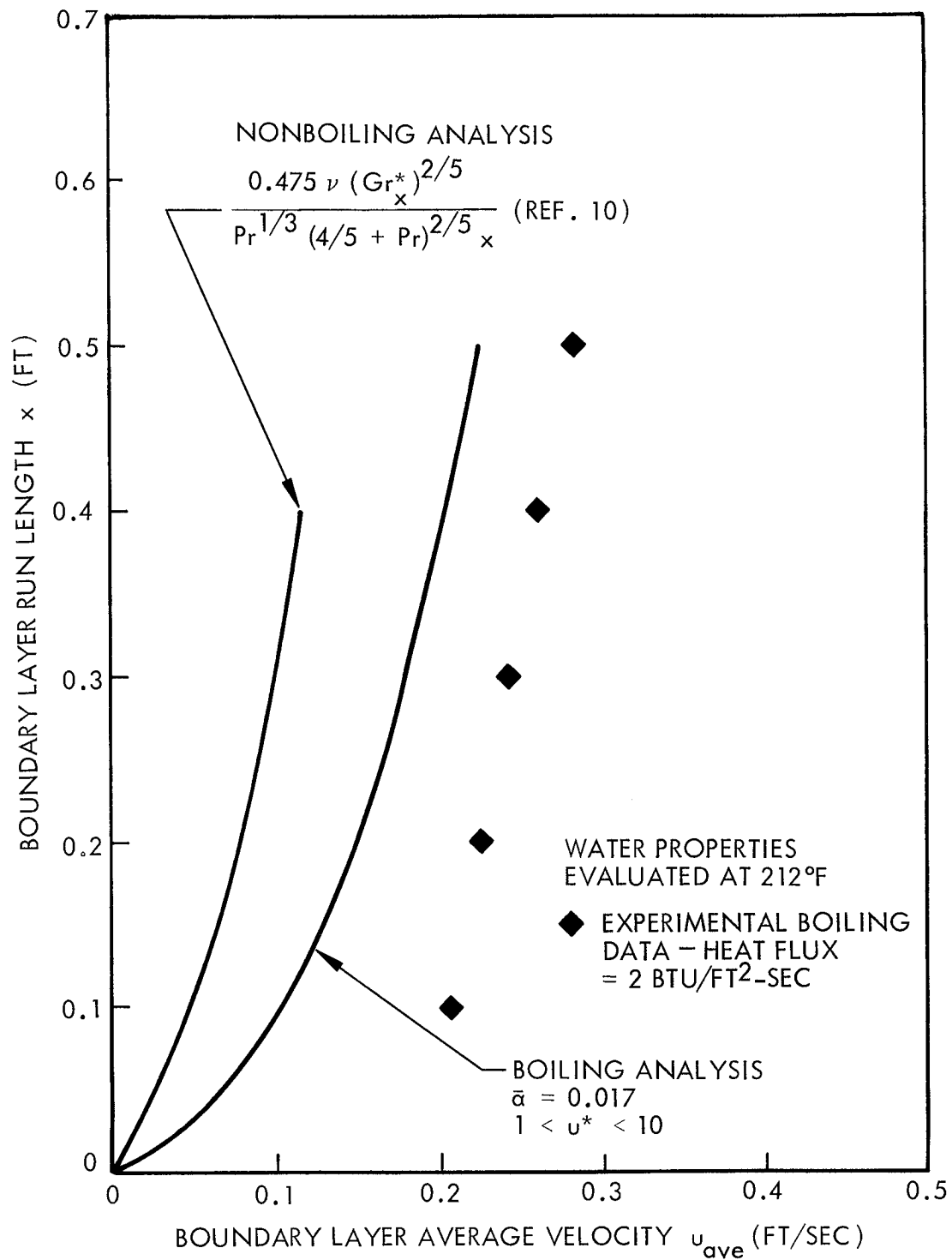
Fig. 6-6 Comparison of Experimental Results With Predictions for Boiling, Free-Convection, Boundary-Layer Average Velocity

6-19

by the vapor through viscous drag. A boundary-layer model which attempts to account for this effect results in predictions which are in general agreement with the experimental results.

6.2.2 Stratification Effects

Preliminary experiments have been conducted with Freon 11 in the pressure vessel described in Section 4 to obtain stratification data with a boiling boundary layer at the wall.

In order to establish the boiling characteristics of Freon 11, measurements were first made, in a transparent container, of the heat-transfer coefficient with and without boiling. An electric shim-stock heater plate with a thermocouple on the heating surface was submerged in the Freon 11. The plate, which was oriented in a vertical position, was 7 in. high with the wall thermocouple located 5 in. from the bottom. A range of currents was passed through the heater, and the heat rate, and wall and bulk temperatures were recorded. During these experiments, the existence and intensity of any boiling which occurred was observed visually.

The measured values of the boiling heat-transfer coefficient were used in Eq. (6.34) to predict the stratified layer growth. Equation (6.34) may also be used to predict the stratified layer growth with a nonboiling boundary layer if the appropriate nonboiling heat-transfer coefficient is used. In Fig. 6-7, these predictions are compared to experimental data from two tests at the same liquid heat rate, one with boiling in the boundary layer and one with the liquid subcooled at 150 psig to prevent boiling. A second nonboiling prediction, shown in Fig. 6-7, is based on the modified turbulent free-convection boundary-layer solution (Ref. 1).

The stratified layer growth prediction for the nonboiling case based on the measured heat-transfer coefficient is in much better agreement with the experimental data than the prediction based on the modified turbulent boundary-layer solution. For the boiling case, the data are in good agreement with the prediction and confirm that boiling in the boundary layer results in a substantially increased stratified layer growth rate. Additional data will be obtained in a continuing experimental program to evaluate fully the effects of nucleate boiling on stratification and on liquid-ullage coupling.
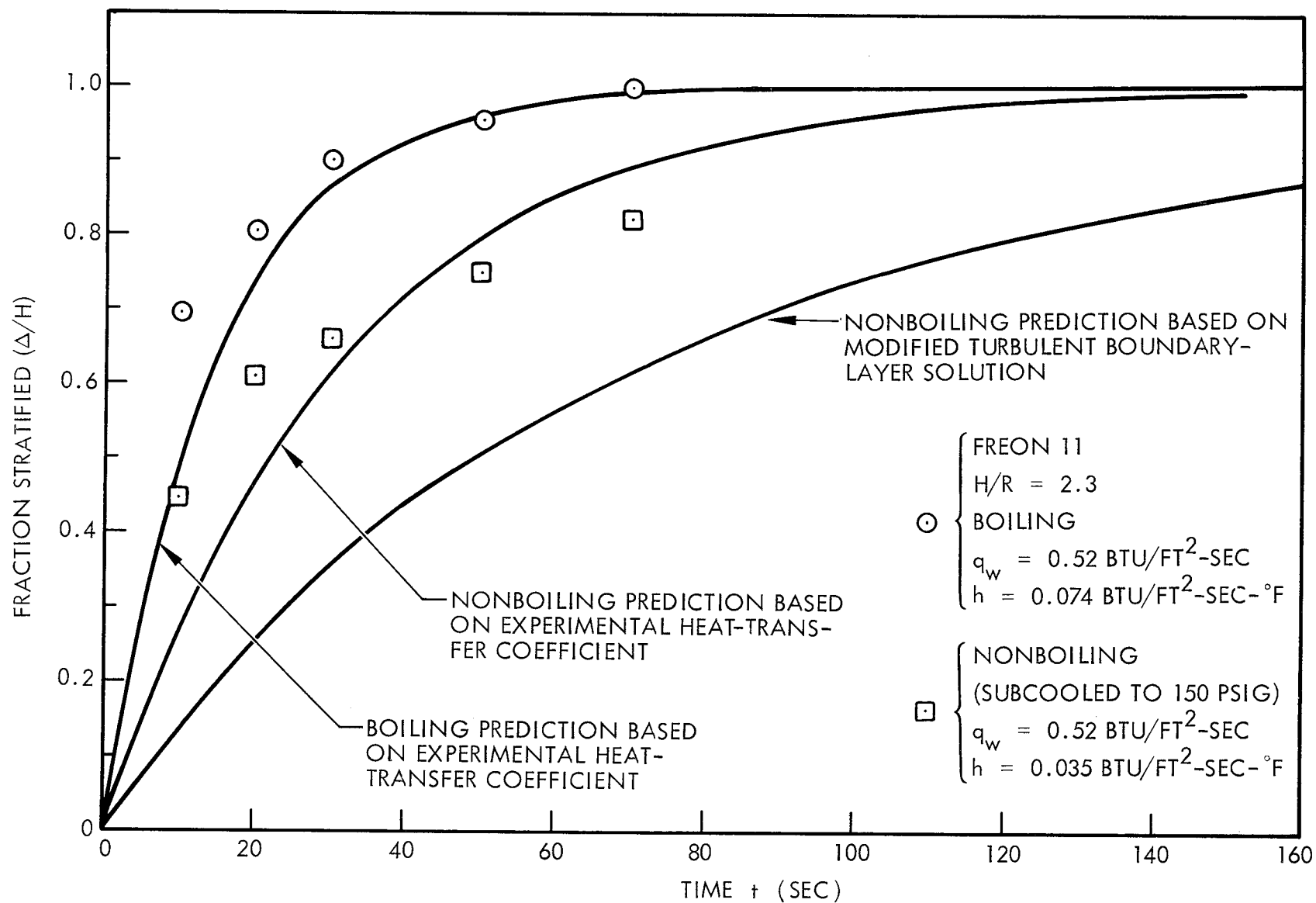
Fig. 6-7 Comparison of Experimental Results With Predictions for Stratified Layer Growth With Boiling and Nonboiling Boundary-Layer Conditions

Section 7

CORRELATION OF CRYOGENIC STRATIFICATION DATA

An objective of the present study was to apply the analytical techniques developed for predicting stratification to the correlation of cryogenic liquid stratification data. The general approach has been to check first the validity and repeatability of the calibrated or assumed heat-flux boundary conditions, and then to compare the temperature data with the integral analyses developed. The analyses presently include the capability for considering sidewall and bottom heating with or without nucleate boiling in the free-convection boundary layer. The effects of liquid-ullage coupling have not yet been sufficiently investigated to be included in these correlations of the liquid temperature data.

7.1 REVIEW OF EXPERIMENTAL PROGRAMS

Four series of liquid-hydrogen stratification tests, sponsored by NASA/MSFC, were considered. A description of each program is presented in the following subsections.

7.1.1 Lockheed Tests

These tests were conducted by Lockheed-Georgia Company for LMSC under the RIFT development program. The test tank was a 40-in.-i.d. dewar with an inside height of 98 in. The inner tank was suspended by cables from the outer tank which was located on a test pad exposed to ambient atmospheric conditions. The primary mode of heat transfer to the liquid for the higher heat-flux condition was by radiation across the evacuated annulus between the high-emittance surfaces of the tank walls.

The resulting heat flux was between 0.019 and 0.022 Btu/ft^2-sec, depending upon the atmospheric condition effect on the outer tank temperature. The lower heat-flux condition of approximately 0.0035 Btu/ft^2-sec was achieved by filling the tank annulus with expanded Perlite powder, and then evacuating the interstitial volume of residual gas. The heat transfer to the inner tank in these runs was thus effected by conduction and radiation through the powder.

7-1

The liquid-filled portion of the fill line (between the valve and the tank bottom) was vented to the tank ullage through a bypass line so that liquid would not be forced into the tank as energy leaked into the fill line, expanding and vaporizing the liquid trapped there. This arrangement is thought to have greatly increased the rate of pressurization of the tank during passive pressurization runs. It is also likely that considerable energy transfer to the ullage vapor in the vent system took place. The passive pressurization was therefore controlled primarily by energy and mass transfer from outside the tank and does not represent true self-pressurization.

The liquid-hydrogen temperatures were measured with carbon resistors; each sensor, with its own bridge circuit, was individually calibrated. Carbon resistors were also used as point liquid-level sensors. The liquid-temperature sensor locations and tank configuration are shown in Fig. 7-1.

The calibrated gross heat rates are considered to be quite accurate; they were obtained by measuring the rate of change of the liquid level during steady-state, vented boiloff runs prior to each new test condition and equating the heat transfer to the mass transfer multiplied by the latent heat of vaporization. Since the test vessel was a dewar, with approximately uniform heat-transfer characteristics throughout the annular space, the heat flux to the inner tank was assumed to be constant over the entire tank area.

Prior to each test run, the liquid was allowed to become saturated at 1 atm pressure. For passively pressurized runs, the vent valve was closed at time zero and the test was terminated when the tank pressure reached approximately 35 psia. For actively pressurized runs, the vent valve was closed and pressurization initiated at time zero; the tank pressure of 35 psia was reached in about 40 sec and was maintained constant by controlling the vent and pressurant valves. Details of the experimental apparatus and procedures and a tabulation of the data are presented in Ref. 11. The test conditions are shown in Table 7-1.
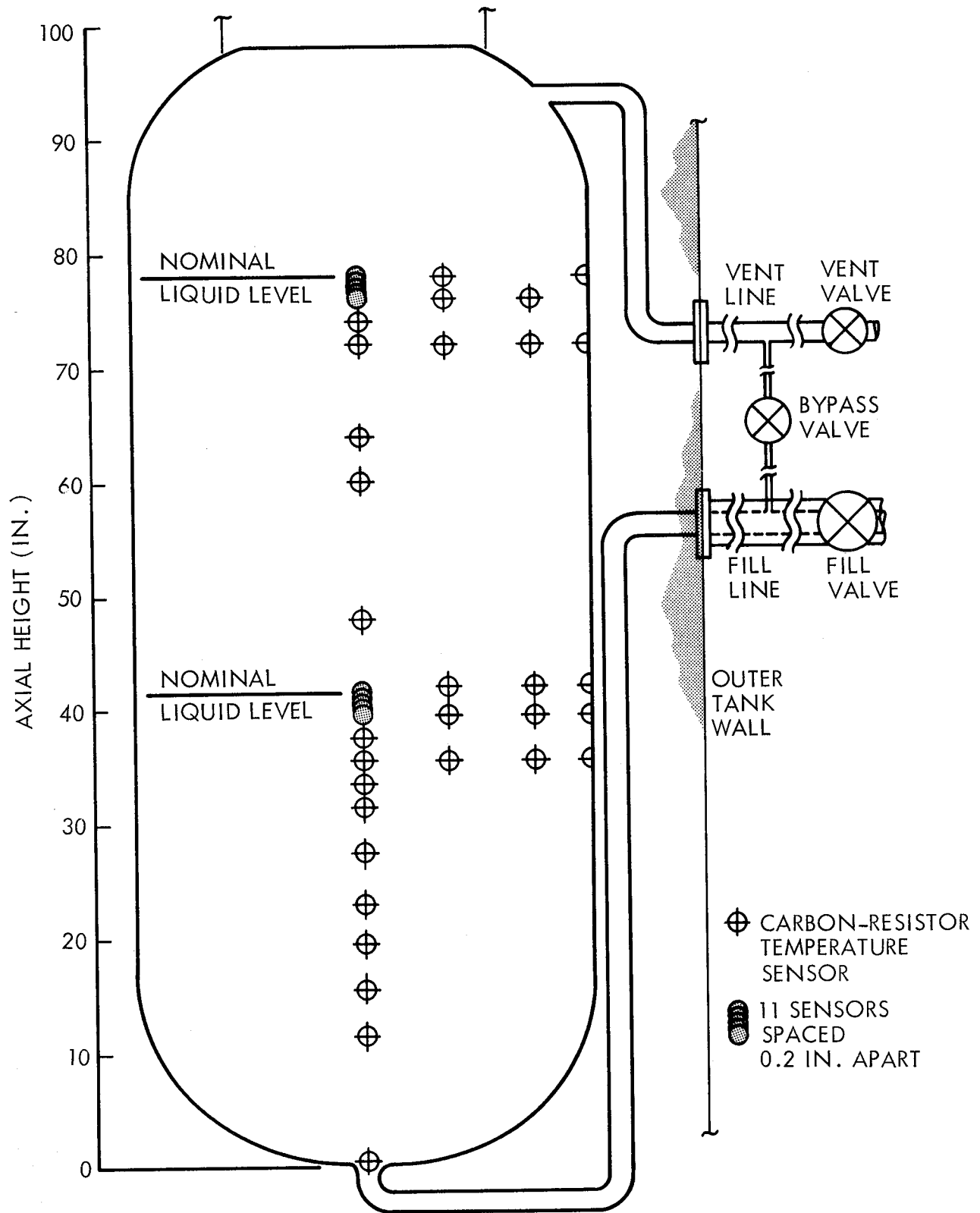
Fig. 7-1 Test Tank and Instrumentation — Lockheed

LOCKHEED MISSILES & SPACE COMPANY

Table 7-1

STRATIFICATION TEST CONDITIONS – 40-INCH-DIAMETER TANK (LOCKHEED)

Run No.	Time Interval (sec)	Pressurization* Mode (psia)	Energy Balance Results				Calibration Data		
			Net Heat Rate (Btu/sec)	Net Energy (Btu)	Heat Flux		Gross Heat Rate (Btu/sec)	Heat Flux	
					Sidewall (Btu/ft^2-sec)	Bottom (Btu/ft^2-sec)		Sidewall (Btu/ft^2-sec)	Bottom (Btu/ft^2-sec)
L-1	0 to 60	14.2-P-19.8	1.66	100	0.0252	0.0187	1.30	0.0187	0.0187
	60 to 120	19.8-P-24.8	1.23	174	0.0173	↓	↓	↓	↓
	120 to 300	24.8-P-35.2	1.21	391	0.0169				
L-2	0 to 60	14.2-A-35.4	2.01	121	0.0318	0.0188	1.31	0.0188	0.0188
	60 to 120	35.4-C-35.4	1.30	199	0.0187				
	120 to 300	35.4-C-35.4	1.13	403	0.0156				
	300 to 600	35.4-C-34.9	1.07	723	0.0144				
	600 to 1,200	34.9-C-35.4	1.05	1,351	0.0140				
	1,200 to 1,740	35.4-C-35.3	1.08	1,933	0.0144	↓	↓	↓	↓
L-6	0 to 60	13.6-P-16.3	1.00	60	0.0291	0.0224	0.85	0.0224	0.0224
	60 to 120	16.3-P-18.3	0.92	115	0.0256				
	120 to 300	18.3-P-23.0	0.91	279	0.0251				
	300 to 600	23.0-P-30.3	0.75	503	0.0180				
	600 to 900	30.3-P-37.6	0.74	724	0.0175	↓	↓	↓	↓
L-7	0 to 60	13.6-A-34.3	1.50	90	0.0511	0.0224	0.85	0.0224	0.0224
	60 to 120	34.3-C-34.3	0.74	135	0.0178				
	120 to 300	34.3-C-34.0	0.82	283	0.0212				
	300 to 600	34.0-C-35.3	0.75	508	0.0180				
	600 to 900	35.3-C-34.5	0.75	734	0.0179				
	900 to 1,200	34.5-C-34.0	0.69	940	0.0153				
	1,200 to 1,500	34.0-C-34.3	0.76	1,169	0.0182	↓	↓	↓	↓
L-9	0 to 60	14.2-P-19.1	0.42	24.9	0.0065	0.0035	0.24	0.0035	0.0035
	60 to 120	19.1-P-23.2	0.06	28.4	0.0001				
	120 to 300	23.2-P-35.7	0.23	70.6	0.0033	↓	↓	↓	↓
L-10	0 to 60	14.2-A-35.7	0.64	38.2	0.0107	0.0034	0.24	0.0034	0.0034
	60 to 120	35.7-C-35.7	0.33	58.0	0.0051				
	120 to 300	35.7-C-35.4	0.14	84.1	0.0017				
	300 to 1,800	35.4-C-35.2	0.10	240.8	0.0010	↓	↓	↓	↓

*P Passive pressurization
A Active pressurization with GH$_2$
C Held constant

7.1.2 MSFC Tests

These tests were conducted at MSFC, utilizing the full-scale propellant tank of the S-IV stage of the Saturn-I launch vehicle. The tank was 220 in. in diameter and 340 in. long, including a nested liquid-oxygen tank in the bottom. The LOX tank was filled with liquid nitrogen during these tests. The hydrogen tank was internally insulated with 0.5 in. and 0.75 in. of polyurethane foam. The thermal conductivity of the insulation is estimated to be about 0.04 Btu/ft-hr-° R. The bulkhead between the LN_2-filled LOX tank and the LH_2 tank was constructed of 1-in.-thick fiberglass honeycomb which was evacuated to 1.5 psia. The heat transfer to the LH_2 was thus controlled by conduction through the foam and fiberglass.

The LH_2 temperatures were measured with platinum resistance thermometers and the liquid level was monitored with a capacitance probe. The instrumentation locations and tank configuration are shown in Fig. 7-2. Not shown is a boundary-layer rake for measuring temperatures close to the wall at an axial height of 112 in. The insulation thicknesses shown are not drawn to scale.

Two test series were conducted which were similar except for minor instrumentation changes. The second series of tests had fewer radial temperature measurements in the liquid, but added ullage temperatures and vent orifice pressure and temperature data. Both tests were conducted under the same conditions, except for a possible degradation of the insulation in the second series. The schedule of test conditions is shown in Table 7-2.

Each stratification test was preceded by a saturated boiloff test in order to evaluate the steady-state heat rate to the tank. However, valid flow-rate data were obtained from the second test series only. The first stratification test in each series was passively pressurized; the second test was actively pressurized with GH_2, and the rest were pressurized to different levels with GHe. The vent valve remained closed during these runs until the tank pressure reached approximately 28 psig.

LOCKHEED MISSILES & SPACE COMPANY
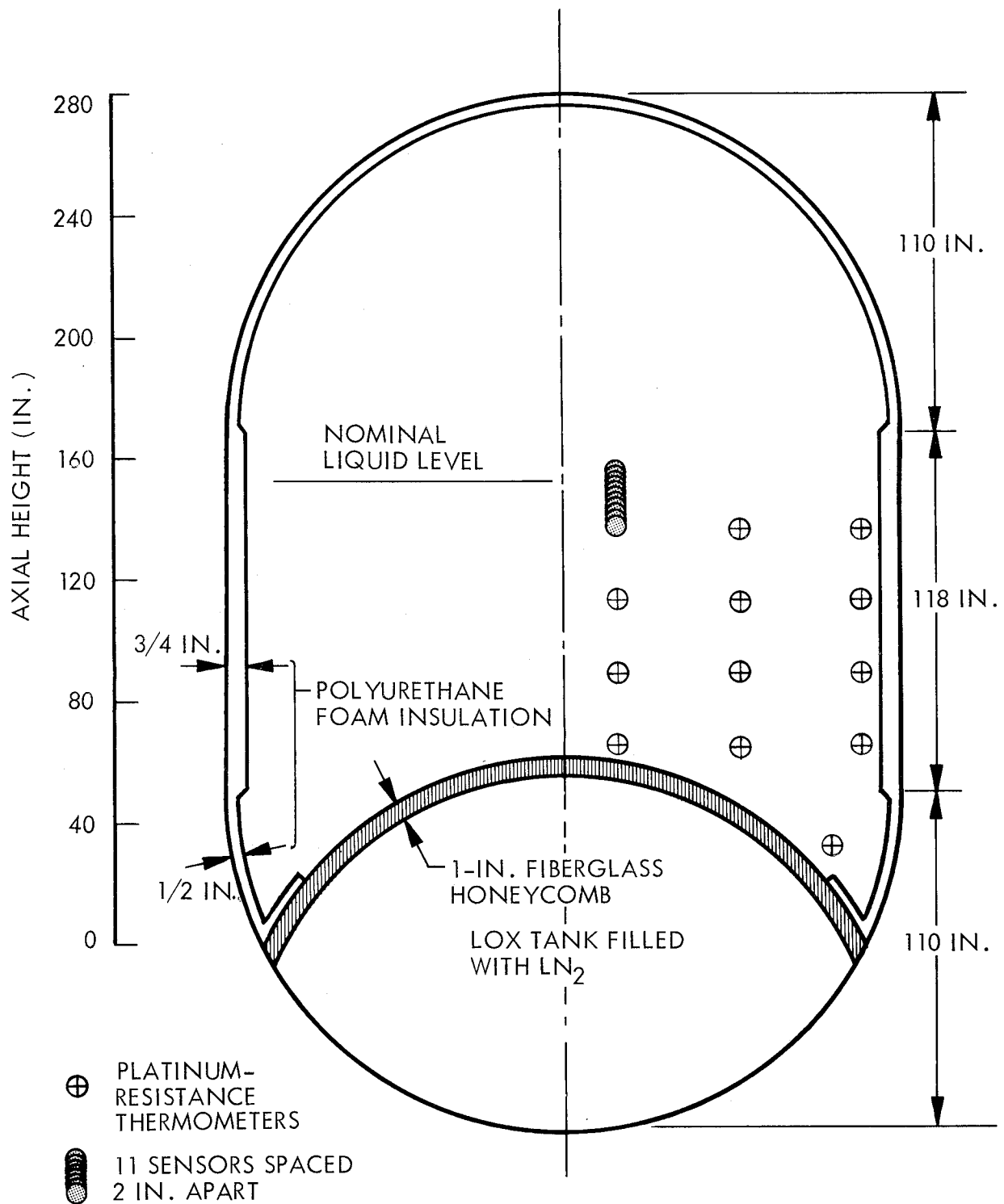
Fig. 7-2 S-IV Tank and Instrumentation — MSFC

Table 7-2

STRATIFICATION TEST CONDITIONS – S-IV TANK (MSFC)

Run No.	Time Interval (sec)	Pressurization* Mode (psia)	Energy Balance Results				Calibration Data		
			Net Heat Rate (Btu/sec)	Net Energy (Btu)	Heat Flux		Gross Heat Rate (Btu/sec)	Heat Flux	
					Sidewall (Btu/ft²-sec)	Bottom (Btu/ft²-sec)		Sidewall (Btu/ft²-sec)	Bottom (Btu/ft²-sec)
N1-B	5 to 100	15.1-P-17.5	46.4	4,402	0.0455	0.0455	—	0.0375	—
	100 to 200	17.5-P-19.6	36.7	8,068	0.0360	0.0360			
	200 to 300	19.6-P-21.5	33.8	11,448	0.0332	0.0332			
	300 to 551	21.5-P-25.7	37.2	20,773	0.0365	0.0365			
	551 to 1,151	25.7-P-34.1	37.5	43,241	0.0366	0.0366			
	1,151 to 1,751	34.1-P-40.5	39.4	66,869	0.0383	0.0383			
N1-D	5 to 55	15.3-V-15.3	-3.3	-166	—	—	—	0.0380	—
	55 to 100	15.3-A-34.9	98.8	4,278	0.0949	0.0949			
	100 to 205	34.9-P-34.7	22.1	6,598	0.0213	0.0213			
	205 to 325	34.7-P-35.6	39.8	11,377	0.0383	0.0383			
	325 to 595	35.6-P-38.4	39.1	21,932	0.0376	0.0376			
	595 to 895	38.4-P-41.5	37.4	33,137	0.0359	0.0359			
N2-B	5 to 102	15.3-P-18.3	59.6	5,788	0.0581	0.0581	39.1	0.0501	—
	102 to 202	18.3-P-21.0	44.6	10,248	0.0434	0.0434			
	202 to 330	21.0-P-24.0	48.5	16,459	0.0472	0.0472			
	330 to 420	24.0-P-25.9	58.6	21,738	0.0570	0.0570			
	420 to 837	25.9-P-34.2	49.0	42,151	0.0475	0.0475			
	837 to 1,313	34.2-P-42.1	51.6	66,729	0.0499	0.0499			
N2-D	5 to 60	15.3-A-33.3	136.4	7,502	0.1353	0.1353	46.7	0.0514	—
	60 to 303	33.3-P-35.5	53.3	20,439	0.0527	0.0527			
	303 to 541	35.5-P-38.8	48.0	31,855	0.0474	0.0474			
	541 to 779	38.8-P-42.2	48.4	43,366	0.0477	0.0477			
	779 to 957	42.2-P-42.2	48.8	52,043	0.0480	0.0480			
N2-F	5 to 75	15.4-AH-40.5	87.2	6,106	0.0857	0.0857	42.5	0.0528	—
	75 to 313	40.5-P-41.5	52.8	18,692	0.0519	0.0519			
	313 to 610	41.5-P-42.7	48.2	33,008	0.0472	0.0472			
	610 to 847	42.7-P-43.5	48.3	44,473	0.0472	0.0472			
N2-H	5 to 35	15.4-V-15.5	13.0	388	0.0125	0.0125	44.8	0.0519	—
	35 to 114	15.5-AH-33.0	92.1	7,663	0.0888	0.0888			
	114 to 352	33.0-P-35.7	48.8	19,263	0.0469	0.0469			
	352 to 589	35.7-P-39.6	51.4	31,455	0.0494	0.0494			
	589 to 767	39.6-P-42.3	46.6	39,759	0.0448	0.0448			
	767 to 872	42.3-C-42.3	49.0	44,910	0.0470	0.0470			
	872 to 902	42.3-V-20.0	-105.8	41,734	—	—			
	902 to 1,109	20.0-P-25.7	54.6	53,042	0.0524	0.0524			
	1,109 to 1,316	25.7-P-29.1	49.4	63,257	0.0470	0.0470			
N2-J	-38 to 80	15.4-AH-38.3	81.5	9,616	0.0800	0.0800	44.1	0.0528	—
	80 to 469	38.3-P-42.4	49.5	28,865	0.0484	0.0484			
	469 to 1,065	42.4-C-42.3	47.8	57,403	0.0468	0.0468			
	1,065 to 1,541	42.3-C-42.1	46.1	79,369	0.0448	0.0448			
	1,541 to 2,016	42.1-C-42.3	45.5	100,984	0.0440	0.0440			
	2,016 to 2,548	42.3-C-41.9	46.3	125,630	0.0446	0.0446			

*P   Passive pressurization
V   Vented
A   Active pressurization with GH_2
AH   Active pressurization with GHe
C   Held constant

LOCKHEED MISSILES & SPACE COMPANY

7.1.3 Martin Sidewall Heating Tests

These tests were conducted by the Aerospace Division of the Martin-Marietta Corporation in a 4-ft.-i.d. dewar which was 80 in. in length. The inner tank was supported vertically by four legs and horizontally by tie rods connected to the upper and lower domes. An array of quartz lamps mounted in the annulus provided variable heating rates to a 54-in. long cylindrical section of the inner tank. The domes of the inner tank were covered with multilayer insulation to shield against radiation from the outer tank. The range of heat fluxes for these tests was from 0.1 to 1.2 Btu/ft^2-sec; the variation was obtained by changing the circuit configuration of the lamp array.

The liquid temperatures were measured with carbon thermistors, each with its own bridge circuit and voltage source. A differential pressure slant tube manometer was used to monitor the liquid level within ± 0.5 in. The locations of the thermistors and the tank arrangement are shown in Fig. 7-3.

The conditions of interest included one passively pressurized run, one run actively pressurized with GH_2, and 11 runs pressurized with GHe. In all runs, the power to the lamps was turned on at time zero. For the actively pressurized runs, pressurization was initiated 30 sec before the lamps were turned on, and the tank pressure was maintained constant by manually controlling the addition of pressurant, or venting, as required. A list of the test conditions considered here is presented in Table 7-3. The test program also included runs with draining and with shaking of the test vessel; these runs will not be discussed here.

The heat flux to the liquid was determined in two ways: (1) the two lowest heat-flux calibrations were obtained from measurements of the boiloff rates from essentially saturated liquid, and (2) the two highest heat-flux calibrations were obtained from calculations of the enthalpy gain of the liquid for two of the actual test runs. A fifth calibration curve was obtained by interpolation. These calibration curves are shown in Fig. 7-4. Details of the test apparatus and procedure and plots of the data are presented in Ref. 12.
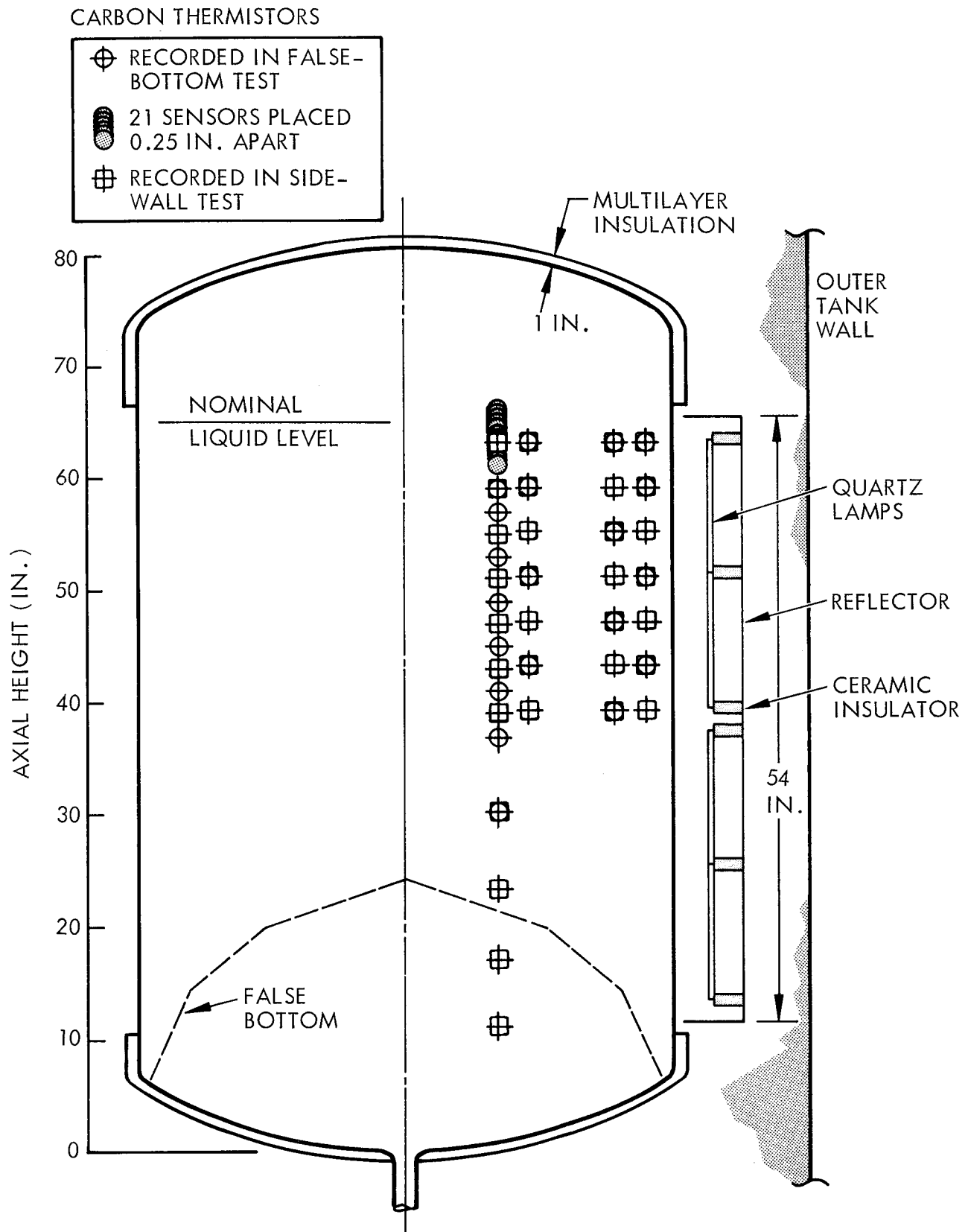
Fig. 7-3 Test Tank and Instrumentation — Martin

7-9

Table 7-3

STRATIFICATION TEST CONDITIONS – SIDEWALL HEATING (MARTIN)

Run No.	Time Interval (sec)	Pressurization* Mode (psia)	Energy Balance Results				Calibration Data		
			Net Heat Rate (Btu/sec)	Net Energy (Btu)	Heat Flux Sidewall (Btu/ft²-sec)	Heat Flux Bottom (Btu/ft²-sec)	Gross Heat Rate (Btu/sec)	Heat Flux Sidewall (Btu/ft²-sec)	Heat Flux Bottom (Btu/ft²-sec)
M-1	-30 to 0	12.7-AH-52.9	5.3	159	0.091	0.014	0.2	0	0.014
	0 to 60	52.9-P-55.7	29.8	1,347	0.531	↓	27.1	0.483	↓
	60 to 120	55.7-P-68.1	35.7	4,090	0.637		39.0	0.696	
	120 to 180	68.1-P-92.7	46.2	6,862	0.825		34.0	0.606	
M-1A	-30 to 0	11.6-AH-51.6	3.0	89	0.050	0.014	0.2	0	0.014
	0 to 60	51.6-C-51.6	29.6	1,866	0.527	↓	25.7	0.458	↓
	60 to 120	51.6-C-51.6	33.2	3,858	0.592		37.0	0.660	
	120 to 180	51.6-C-51.6	35.3	5,976	0.630		32.3	0.576	
M-2	-30 to 0	12.7-AH-23.6	1.8	54	0.028	0.014	0.2	0	0.014
	0 to 30	23.6-C-23.6	20.6	673	0.366	↓	20.6	0.366	↓
	30 to 60	23.6-C-23.6	30.1	1,575	0.536		33.4	0.596	
M-3	-30 to 0	11.9-AH-33.8	2.1	63	0.034	0.014	0.2	0	0.014
	0 to 60	33.8-C-33.8	20.0	1,264	0.355	↓	27.1	0.483	↓
	60 to 120	33.8-C-33.8	28.9	2,999	0.515		39.0	0.696	
	120 to 180	33.8-C-33.8	9.1	3,547	0.159		34.0	0.606	
M-4	-30 to 0	11.9-AH-71.8	5.6	168	0.101	0.014	0.2	0	0.014
	0 to 60	71.8-C-71.8	17.2	1,199	0.318	↓	25.9	0.483	↓
	60 to 120	71.8-C-71.8	30.3	3,019	0.558		37.8	0.696	
	120 to 204	71.8-C-71.8	43.5	6,680	0.776		34.0	0.606	
M-5	-30 to 0	11.9-A-48.8	-1.0	-30	—	0.014	0.2	0	0.014
	0 to 60	48.8-C-48.8	20.6	1,207	0.411	↓	24.1	0.483	↓
	60 to 120	48.8-C-48.8	28.7	2,929	0.564		35.4	0.696	
	120 to 180	48.8-C-48.8	37.8	5,200	0.715		32.0	0.606	
M-7	0 to 60	12.7-P-22.6	20.9	1,257	0.374	0.014	26.9	0.483	0.014
	60 to 120	22.6-P-35.6	31.6	3,153	0.563	↓	39.0	0.696	↓
	120 to 180	35.6-P-56.4	37.4	5,399	0.667		34.0	0.606	
	180 to 240	56.4-P-86.1	41.2	7,873	0.735		33.4	0.596	
M-8	-30 to 0	12.7-AH-51.8	5.9	177	0.102	0.014	0.2	0	0.014
	0 to 120	51.8-C-51.8	5.2	797	0.089	↓	6.3	0.110	↓
	120 to 240	51.8-C-51.8	9.0	1,875	0.157		11.0	0.193	
	240 to 360	51.8-C-51.8	8.8	2,936	0.154		13.5	0.238	
	360 to 480	51.8-C-51.8	9.2	4,039	0.161		14.0	0.248	
M-10A	-30 to 0	11.7-AH-51.1	5.7	170	0.104	0.014	0.2	0	0.014
	0 to 60	51.1-C-51.1	9.1	717	0.168		8.3	0.154	
	60 to 120	51.1-C-51.1	9.0	1,259	0.165		12.0	0.221	
	120 to 180	51.1-C-51.1	15.9	2,211	0.292		15.5	0.284	
	180 to 240	51.1-C-51.1	12.0	2,932	0.217		18.5	0.336	
	240 to 300	51.1-C-51.1	15.8	3,880	0.284	↓	20.6	0.371	↓
	300 to 360	51.1-C-51.1	14.1	4,724	0.250		21.3	0.382	
M-11	-30 to 0	12.7-AH-51.8	2.8	84	0.051	0.014	0.2	0	0.014
	0 to 60	51.8-C-51.8	15.3	1,004	0.296		13.7	0.266	
	60 to 120	51.8-C-51.8	17.9	2,076	0.342		22.8	0.437	
	120 to 180	51.8-C-51.8	23.6	3,493	0.445	↓	28.3	0.535	↓
	180 to 242	51.8-C-51.8	18.2	4,620	0.337		27.0	0.504	
M-12	-30 to 0	15.8-AH-57.3	2.3	68	0.037	0.014	0.2	0	0.014
	0 to 30	57.3-C-57.3	38.4	1,220	0.685		41.8	0.748	
	30 to 60	57.3-C-57.3	58.0	2,960	1.037		73.5	1.316	
	60 to 90	57.3-C-57.3	60.0	4,760	1.072	↓	61.8	1.107	↓
	90 to 120	57.3-C-57.3	50.8	6,283	0.909		57.6	1.030	
M-24	-30 to 0	11.5-AH-31.6	1.1	32	0.018	0.014	0.2	0	0.014
	0 to 60	31.6-C-31.6	6.3	408	0.113	↓	8.5	0.154	↓
	60 to 120	31.6-C-31.6	11.0	1,069	0.199		12.2	0.221	
M-25	-30 to 0	11.5-AH-31.6	-0.2	-7	—	0.014	0.2	0	0.014
	0 to 60	31.6-C-31.6	4.6	272	0.082		4.8	0.087	
	60 to 120	31.6-C-31.6	5.7	611	0.103		7.2	0.132	
	120 to 180	31.6-C-31.6	7.6	1,068	0.138	↓	9.6	0.176	↓
	180 to 240	31.6-C-31.6	10.6	1,704	0.192		11.6	0.212	

*AH   Active pressurization with GHe
P   Passive pressurization
C   Held constant
A   Active pressurization with GH$_2$
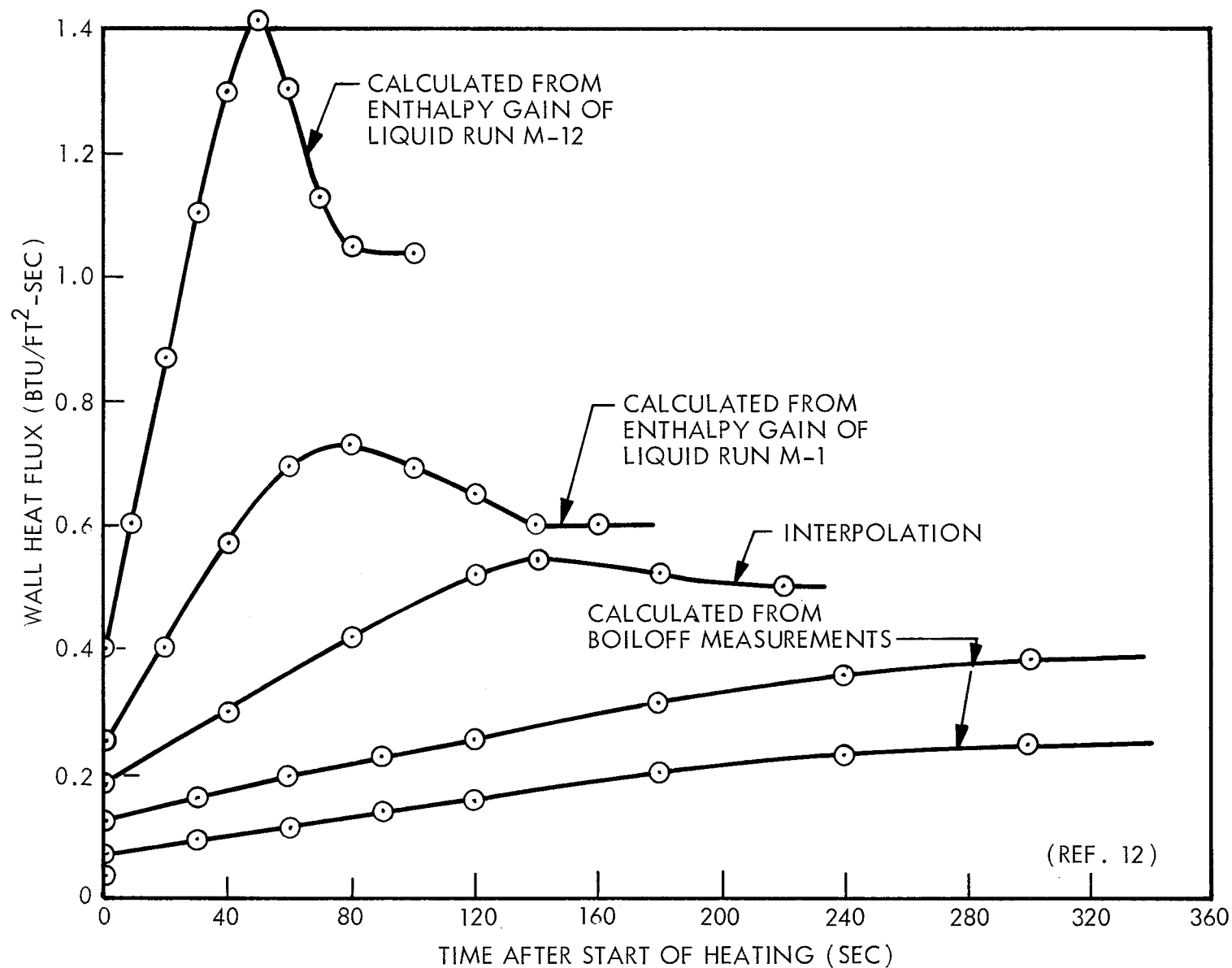
Fig. 7-4 Heat Flux Vs. Time for Martin Liquid-Hydrogen Stratification Tests

7.1.4 Martin Bottom Heating Tests

These tests were conducted using the same facility, test tank, and instrumentation described above for the sidewall heating tests (Subsection 7.1.3), except for the following changes. A false bottom with a wire resistance heater was installed in the tank, as shown in Fig. 7-3. This bottom heater received power from a Variac voltage-control system. In Runs MB-1 through MB-12 the sidewall heat-flux calibrations from the earlier tests were used, although a 240-v rather than a 480-v power source was employed. The lamps were turned on simultaneously with the closing of the vent valve and the initiation of pressurization, instead of pressurizing prior to the start of heating. Runs MB-13 through MB-20 used a 240-v Variac voltage control for the sidewall heating lamps in order to achieve the low heating rates desired. There was no calibration of the sidewall heating for these tests, although several methods were suggested for estimating them based on assumed efficiencies and reradiation terms. These runs incorporated a preheating period during which the heat chamber was allowed to approach its steady thermal operating condition before pressurization was initiated at time zero. Table 7-4 lists the nominal test conditions. Details of the test procedures and a tabulation of the data are presented in Refs. 13 and 14.

7.2 MASS AND ENERGY BALANCES

A computer program was written to calculate the net heat transfer to the liquid during a thermal stratification test. This program was intended to be used to evaluate the accuracy and repeatability of the test results and boundary conditions. For most of the tests, the results indicated poor accuracy of the calibrations, so that the boundary conditions used in the correlations have been based on the net energy stored in the liquid as calculated by the energy balance program. A brief description of this calculation routine is presented, and the results of its application to the cryogenic stratification data are discussed.

Table 7-4

STRATIFICATION TEST CONDITIONS – BOTTOM HEATING (MARTIN)

Run No.	Time Interval (sec)	Pressurization* Mode (psia)	Energy Balance Results — Net Heat Rate (Btu/sec)	Net Energy (Btu)	Heat Flux Sidewall (Btu/ft²-sec)	Heat Flux Bottom (Btu/ft²-sec)	Gross Heat Rate (Btu/sec)	Calibration Data — Heat Flux Sidewall (Btu/ft²-sec)	Calibration Data — Heat Flux Bottom (Btu/ft²-sec)
MB-1	0 to 60	12,3-AH-42,3	7.02	421	0.125	0.014 →	4.95	0.087	0.014 →
	60 to 120	42,3-C-42,3	6.61	818	0.116		7.45	0.132	
	120 to 240	42,3-C-42,3	12.13	2,276	0.213		10.98	0.193	
MB-2	0 to 60	12,0-AH-42,0	10.60	636	0.184	0.019 →	5.16	0.087	0.019 →
	60 to 120	42,0-C-42,0	5.75	981	0.097		7.66	0.132	
	120 to 240	42,0-C-42,0	11.46	2,356	0.200		11.07	0.193	
MB-3	0 to 60	12,4-AH-42,4	7.59	455	0.135	0.024 →	5.01	0.087	0.024 →
	60 to 120	42,4-C-42,4	8.25	950	0.146		7.47	0.132	
	120 to 240	42,4-C-42,4	12.65	2,468	0.224		10.96	0.193	
MB-4	0 to 60	12,8-AH-42,8	8.27	496	0.185	0.044 →	5.56	0.087	0.044 →
	60 to 120	42,8-C-42,8	10.27	1,112	0.170		8.09	0.132	
	120 to 240	42,8-C-42,8	12.38	2,599	0.208		11.50	0.193	
MB-9	0 to 120	12,0-AH-42,0	2.40	288	0.0406	0.0140 →	1.80	0.029	0.0140 →
	120 to 240	42,0-C-42,0	2.61	601	0.0444		3.18	0.055	
	240 to 360	42,0-C-42,0	3.03	965	0.0519		3.96	0.069	
MB-10	0 to 120	12,0-AH-42,0	2.48	297	0.0402	0.0191 →	1.90	0.029	0.0191 →
	120 to 240	42,0-C-42,0	2.59	608	0.0420		3.28	0.055	
	240 to 360	42,0-C-42,0	3.13	984	0.0518		4.07	0.069	
MB-11	0 to 120	12,2-AH-42,2	2.60	312	0.0394	0.0243 →	2.04	0.029	0.0243 →
	120 to 240	42,2-C-42,2	2.86	656	0.0439		3.36	0.055	
	240 to 360	42,2-C-42,2	3.95	1,130	0.0634		4.28	0.069	
MB-12	0 to 120	12,1-AH-42,1	3.23	388	0.0442	0.0439 →	2.40	0.029	0.0439 →
	120 to 240	42,1-C-42,1	3.28	781	0.0451		3.83	0.055	
	240 to 360	42,1-C-42,1	3.65	1,219	0.0517		4.65	0.069	
MB-13	0 to 120	12,8-AH-42,8	5.11	614	0.0875	0.0140 →	2.97 →	0.049 →	0.0140 →
	120 to 360	42,8-C-42,8	3.48	1,450	0.0581				
	360 to 600	42,8-C-42,8	3.69	2,336	0.0620				
MB-14	0 to 120	12,4-AH-42,4	5.11	614	0.0858	0.0191 →	3.17 →	0.051 →	0.0191 →
	120 to 360	42,4-C-42,4	3.12	1,362	0.0501				
	360 to 600	42,4-C-42,4	3.16	2,119	0.0508				
MB-15	0 to 120	12,5-AH-42,5	5.01	601	0.0830	0.0243 →	3.32 →	0.052 →	0.0243 →
	120 to 360	42,5-C-42,5	3.03	1,329	0.0469				
	360 to 600	42,5-C-42,5	3.39	2,142	0.0533				
MB-16	0 to 120	12,4-AH-24,9-P-18,9	5.08	610	0.0774	0.0439 →	3.55 →	0.050 →	0.0439 →
		18,9-P-22,2							
		22,2-P-26,1							
MB-17	0 to 120	12,4-AH-42,4	2.70	324	0.0442	0.0140 →	1.31 →	0.021 →	0.0140 →
	120 to 360	42,4-C-42,4	1.70	733	0.0262				
	360 to 600	42,4-C-42,4	1.44	1,079	0.0216				
MB-18	0 to 120	12,4-AH-42,4	2.30	277	0.0354	0.0191 →	1.50 →	0.021 →	0.0191 →
	120 to 360	42,4-C-42,4	1.45	625	0.0201				
	360 to 600	42,4-C-42,4	1.69	1,031	0.0244				
MB-19	0 to 120	12,4-AH-42,4	2.01	241	0.0286	0.0243 →	1.53 →	0.020 →	0.0243 →
	120 to 360	42,4-C-42,4	1.64	635	0.0219				
	360 to 600	42,4-C-42,4	1.40	972	0.0176				
MB-20	0 to 120	12,6-AH-42,6	1.65	198	--	0.0439 →	0.77 →	0 →	0.0439 →
	120 to 360	42,6-C-42,6	1.22	490	--				
	360 to 600	42,6-C-42,6	1.27	794	--				

*AH Active pressurization with GHe
C Held constant
P Passive pressurization

7.2.1 Computer Program

The tank is divided into as many layers as there are liquid temperature sensors, so that each measured temperature represents the mean temperature of a layer. The liquid surface is assumed to be at the saturation temperature corresponding to the measured tank pressure. To accommodate this condition, an additional layer is formed which represents the volume between the highest wetted sensor and the liquid surface. The temperature of this layer is equal to the average between the sensor and surface (saturation) temperatures.

The thermodynamic properties of the liquid are input as functions of temperature and pressure; the variations in these quantities are significant for LH_2. The mass M of each layer is calculated as follows from the temperature- and pressure-dependent specific volume:

$$M = V/v \qquad (7.1)$$

where V is the fixed volume represented by a sensor. The net heat transfer to the layer during a given time interval is calculated from the first law of thermodynamics,

$$dq = dh - \frac{v}{J} dp \qquad (7.2)$$

the thermodynamic equation relating enthalpy and specific volume,

$$\left(\frac{\partial h}{\partial p}\right)_T = \frac{v}{J} - \frac{T}{J}\left(\frac{\partial v}{\partial T}\right)_p \qquad (7.3)$$

and the definitions of the specific heat at constant pressure c_p and the coefficient of thermal expansion β

$$c_p \equiv \left(\frac{\partial h}{\partial T}\right)_p \qquad (7.4)$$

$$\beta \equiv \frac{1}{v}\left(\frac{\partial v}{\partial T}\right)_p \tag{7.5}$$

Equation (7.2) may be re-written

$$dq = \left(\frac{\partial h}{\partial T}\right)_p dT + \left[\left(\frac{\partial h}{\partial p}\right)_T - \frac{v}{J}\right] dp \tag{7.6}$$

Substitution of Eqs. (7.3), (7.4), and (7.5) into (7.6) yields

$$dq = c_p dT - \frac{\beta v T}{J} dp \tag{7.7}$$

The energy balance program uses Eq. (7.7), integrated in finite difference form, with Eq. (7.1) to calculate the net heat transfer.

$$Q_m = \sum^n \left\{ \frac{V_n}{v_{m,n}} \sum^m \left[c_p (T_{m,n} - T_{m-1,n}) - \frac{\beta v T}{J} (p_m - p_{m-1}) \right] \right\} \tag{7.8}$$

where m denotes a time and n a layer.

The liquid level is determined from mass and energy balances on the liquid. This may be accomplished in two ways, as follows:

- If the heat rate to the liquid is known accurately from an independent measurement or calibration, the decrease in liquid mass due to vaporization ΔM_m is related to the difference between the boundary heat rate q_w and the calculated net heat transfer Q_m by the equation:

$$\sum^m q_{w,m} A_{w,m} \left(t_m - t_{m-1}\right) = Q_m + \Delta M_m \Big\{ \lambda + c_p \left(T_{sat} - T_N\right)$$

$$+ \sum^m \left[c_p \left(T_{m,N} - T_{m-1,N}\right) - \frac{\beta v T}{J} \left(p_m - p_{m-1}\right) \right] \Big\}$$

$$(7.9)$$

where T_{sat} denotes the saturation temperature and N denotes the top layer of liquid, from which ΔM is removed. If the heat rate to the liquid is a function of the wetted wall area, this is also taken into account in the energy balance leading to the calculation of liquid level.

- If the boundary heat rate is not accurately known, the liquid level is calculated on the basis of an assumption that the change in liquid volume due to mass transfer is negligible; i.e., the volume change is due to liquid expansion only. This is a good assumption for LH_2 in most cases where the liquid is not saturated.

7.2.2 Application to Data

The results of applying the energy balance program to the data are presented in Tables 7-1 through 7-4. For each test series, the net heat-transfer rate to the liquid as calculated by the program (assuming negligible mass transfer for the calculation of liquid level) is shown as a function of time interval. The corresponding sidewall and bottom heat fluxes during that time interval are also shown. The way in which the heat rates were divided into sidewall and bottom heat fluxes was based on the specific test circumstances, which will be subsequently discussed in greater detail. The time-integrated average values of these heat fluxes were subsequently used in the correlation of the data with the integral analysis.

Calibrated or estimated values of the gross heat-flux boundary conditions also are presented in these tables. In order for these values to be consistent with the energy balance results, they should be equal to or greater than the net heat-flux values obtained from the energy balance, except during periods of active pressurization. This is because the difference between the gross and net heat rates should be due primarily to mass transfer from the liquid to the ullage.

Lockheed Data. The conditions and energy balance results from the Lockheed 40-in. -
diam. tank tests are presented in Table 7-1. Only the temperatures measured on the
tank centerline were used in the computer program. The temperatures at the other
radial locations were found to display no consistent trend, and in any case differed by
only a small amount ($\sim 0.2°R$) from the central probe measurements. The assumption
of no radial temperature gradients appears to be valid for this test.

It is seen from Table 7-1 that the gross heat rates obtained from the calibration data
are consistently greater than the net heat rates obtained from the energy balances on
the test data, except for the early periods during active pressurization or initial pas-
sive pressurization. As mentioned previously, the passive pressurization for this test
series was probably largely due to mass transfer from the fill line. This conclusion
is supported by the fact that the time required to pressurize to 35 psia was the same
for Runs L-1 and L-9 although the gross heat rates were different by a factor of more
than five.

For the high heat-flux and passive pressurization runs (L-1 and L-6), the net heat
rate is seen to be about 50 percent greater during the first 60 sec than at the end of the
runs when a steady value has been reached. This steady value is about 90 percent of
the calibrated gross heat rate. The high heat-flux and active pressurization runs
(L-2 and L-7) indicate a net heat rate during pressurization that is twice as great as
the steady value, which is in turn about 85 percent of the calibrated gross heat rate.

The data from the low heat-flux runs (L-9 and L-10) show the same trend, although the
results at early times are of questionable accuracy due to the small bulk temperature
increases ($\sim 0.1°R$) involved. It is significant to note that, for both of these runs, the
bulk temperature rise of approximately $0.2°R$ at 300 sec is caused primarily by
isentropic compression of the liquid rather than by heat addition. If the second term
on the right hand side of Eq. (7.7) had been neglected, the calculated heat transfer to
the liquid would have been more than twice as great.

The value of net sidewall heat flux was obtained by assuming that the calibrated value
of uniform wall heat flux applies to the tank bottom area and that the balance of the

7-17

net heating to the liquid enters uniformly through the sidewall. The bottom of the sidewall is considered to be located at the effective starting point of the free-convection boundary layer which travels up the wall. For this tank, the starting point was estimated to be at the bottom of the cylindrical section (X = 15 in.). The values of heat flux obtained in this way are shown in Table 7-1 and were used as the boundary conditions for the integral analysis with which the temperature data are compared in Subsection 7.3.2.

MSFC Data. The test conditions and energy balance results for the full-scale S-IV tank tests are shown in Table 7-2. Only those temperatures nearest the tank center-line and the temperature nearest the tank bottom at X = 32 in. (Fig. 7-2) were used in the energy balance calculation. The temperature data were shifted so that all the sensors indicated the same initial temperature before the vent was closed; this procedure eliminated much of the scatter from the axial temperature profiles. The average of the initially wetted sensors was taken to be the true initial temperature.

Calibration data were obtained from steady boiloff runs conducted before each stratification run in the second test series; vented vapor flow rates were obtained using a venturi flow-metering section with a flow coefficient near unity. The incompressible continuity and energy equations, which were used since the measured pressure differential in the venturi was quite small (less than 3 percent of the absolute pressure), were combined to yield

$$\frac{dM}{dt} = A_2 \sqrt{\frac{2g_c}{1 - (A_2/A_1)^2}} \sqrt{\frac{p_1 - p_2}{v}} \qquad (7.10)$$

where subscripts 1 and 2 denote the upstream and throat locations, respectively. As in the Lockheed tests, the gross heat rate was obtained from

$$\frac{dQ}{dt} = \lambda \frac{dM}{dt} \qquad (7.11)$$

7-18

LOCKHEED MISSILES & SPACE COMPANY

The calibrated gross heat rates shown in Table 7-2 are the average values from the preceding boiloff test (Runs N2-A, C, E, G, and I). The energy balance net heat rates are consistently greater than the calibrated values, which is not consistent with the Lockheed results or with the expected condition that net vaporization would require a gross heat rate to the liquid greater than the net retained energy. The net heat rates during active pressurization and the initial period of passive pressurization are consistently greater than the steady values observed later in each run. This addition of energy to the liquid from the pressurant was also observed in the Lockheed data. It is also noted that the net retained energy is consistently and significantly greater for the second series of tests than for the first. This has been tentatively attributed to differences in atmospheric conditions between the two test series; the measured tank outer-wall temperatures were higher during the later tests. Using these wall temperatures, and assuming an effective thermal conductivity of 0.04 Btu/ft-hr-$^{\circ}$R for the 0.75 in.-thick insulation, yields the approximate values of calibrated sidewall heat flux shown in Table 7-2 for both series of tests. The sidewall and bottom heat fluxes were assumed to be equal for the purpose of applying the integral analysis. This assumption yields sidewall heat fluxes which are consistent with the calibrated values previously described, as they are somewhat lower than the calibrated values after initial pressurization.

Martin Sidewall Heating Data. Table 7-3 lists the test conditions and energy balance results for the Martin sidewall heating stratification tests. The time before time zero represents the period of active pressurization before the heat lamps were turned on. The net energy added to the liquid during this time interval represents energy from the pressurant gas and from the ambient heat leak only. The calculation of this energy addition accounts for the temperature rise of the liquid caused by compression, as explained in Subsection 7.2.1. The magnitude of the energy transfer from the ullage appears generally to be directly related to the pressure rise during active pressurization with helium. The only run actively pressurized with hydrogen (Run M-5) did not indicate a net increase in liquid energy; the reason for this is not clear. The net sidewall heat flux was obtained by subtracting the estimated bottom heat leak of 0.24 Btu/sec from the net heat rate and dividing by the wetted sidewall area. The flux thus

7-19

includes the ullage energy transfer. Temperatures used in the energy balance calculation were the average values at each height where more than one radial temperature was measured.

The calibrated heat rates were obtained from the curves presented in Ref. 12 and shown in Fig. 7-4. However, it was assumed that the measured heat rates included the bottom heat leak of 0.24 Btu/sec, which was subtracted before obtaining the side-wall heat flux shown in Table 7-3. The energy balance results should be in agreement with the calibrated heat rates for Runs M-1 and M-12 since, according to Ref. 12, the calibrations for the two highest heating conditions were obtained by calculating the enthalpy gain of the liquid for those runs. The reasons for the discrepancies are not evident. The calibrated heat flux for Run M-1A is lower than that for Runs M-1 through M-7 since it was conducted after some lamps had been removed from the heat chamber.

Runs M-8, M-10A, M-24, and M-25 represent the two lowest heat-flux conditions. The energy balance results appear to be generally consistent with the calibrated heat rates obtained by measuring steady boiloff flow rates; i.e., the net energy retained by the liquid in these runs is consistently less than the calibrated value due to vaporization.

Martin Bottom Heating Data. The results of the energy balance program are presented in Table 7-4. The "calibration" heat rate data were not obtained by experimental measurement but based on either assumed efficiencies or previous calibrations of a similar but not identical power supply. For all runs, it was assumed that the bottom heater was 100 percent efficient in converting electrical power to heat transfer to the liquid. The ambient heat leak of 0.24 Btu/sec was added to this calculation to obtain the total bottom heat rate.

The sidewall heat-flux calibrations for Runs MB-1 through MB-4 were obtained by using the calibration data for the lowest heat-flux condition in the sidewall heating tests. The "calibrated" values for the lower heating level of Runs MB-9 through MB-12 were obtained by extrapolating the two lowest calibrations from the sidewall heating tests. The lamps were assumed 100 percent efficient when powered by the Variac power supply for Runs MB-13 through MB-19. A correction to these heat rates was suggested in Ref. 14 and applied to obtain different calibrations in Ref. 15. However,

7-20

the results were not significantly different for Runs MB-13 through MB-16, and were improbable for Runs MB-17 through MB-19, since they indicated greater heating rates than if efficiencies of 100 percent were assumed.

The energy balance calculations used only the temperatures measured near the tank centerline; radial gradients were of a random nature. Because there were no temperature measurements below an axial height of 30 in. in this test series (37 in. for Runs MB-1 through MB-12), the measured temperature profiles were extrapolated to obtain values to be used in the energy balance calculation. For this reason, the energy balance results are not as reliable.

The net sidewall heat fluxes were based on the assumption that the bottom heat rate calibrations were accurate. In Runs MB-1 through MB-4, the sidewall heat flux calibrations appear to be too low at later times, in contrast with Runs M-8 and M-25 of the sidewall heating test, which was supposed to have had the same sidewall heat-flux boundary condition. This could be due to the uncertainty in the energy balance results and/or the change in the heat-chamber power supply. The data of Runs MB-9 through MB-12 are consistent, however, since the calibrated heat rates are less than the energy balance heat rates only during the first time interval when active pressurization added energy to the liquid.

The comparison between the calibrations and energy balance data for Runs MB-13 through MB-20 is not consistent because (1) the energy retained did not increase from run to run as the bottom heating was increased (with sidewall heating constant), and (2) the net heat rates were generally greater than the calibrated values after initial pressurization, even though 100 percent efficiencies were assumed for both the bottom and sidewall heaters. These discrepancies may be due in part to experimental errors in the temperature measurements, or to the lack of measurements near the false bottom. The only consistent results were the larger heat rates during pressurization. Run MB-20 suggests that the ambient heat leak may be much larger than the value of 0.24 Btu/sec reported in Ref. 16.

7.3 CORRELATION OF STRATIFICATION DATA

The LH_2 stratification data described in the preceding sections have been correlated with the integral analysis developed at LMSC during the present study. The test correlations fall into two groups based on whether or not boiling was thought to be occurring in the free-convection boundary layer on the tank wall below the stratified layer. A brief literature survey was undertaken in order to estimate the inception point of nucleate boiling in LH_2 and the associated boiling heat-transfer coefficients which are necessary for applying the integral analysis to the boiling boundary layer.

7.3.1 Correlation Methods

The following analytical approaches were employed to perform the test correlations.

Integral Analysis Without Boiling. The Model I analysis of liquid stratification in a right circular cylindrical tank with sidewall and bottom heating (Subsection 2.1.1) was modified to allow the approximate treatment of tanks with non-flat bottoms and with heated wall lengths not equal to the height of the liquid. This modification changes Eq. (2.3) for the thermal stratified layer depth to

$$\frac{\Delta_2(t)}{H} = \frac{1}{2}\left\{\frac{H'}{H} + \frac{\left[(1-I)\left(\frac{q'_B H}{k}\right) + 2\left(\frac{H}{R}\right)\left(\frac{q_w H}{k}\right)\right]\phi_H}{I\,Pr\,(T_S - T_0)}\right\}$$

$$-\frac{1}{2}\left\{\left[\frac{H'}{H} + \frac{\left[(1-I)\left(\frac{q'_B H}{k}\right) + 2\left(\frac{H}{R}\right)\left(\frac{q_w H}{k}\right)\right]\phi_H}{I\,Pr\,(T_S - T_0)}\right]^2 - \frac{8\left(\frac{H}{R}\right)\left(\frac{q_w H}{k}\right)\left(\frac{H'}{H}\right)\phi_H}{I\,Pr\,(T_S - T_0)}\right\}^{1/2}$$

$$(7.12)$$

where H is the heated length, H' and R are the dimensions of an equivalent cylinder with the original tank sidewall area and volume, and q'_B is a modified bottom heat flux which, when multiplied by the equivalent cylinder bottom area πR^2, results

in the original tank bottom heat rate. For times before the mass stratified layer Δ_1 has reached the bottom of the heated length H , Eq. (2.5) for the surface temperature rise remains the same, which results in

$$\frac{\Delta_2 \, (t)}{H} = \frac{1}{2} \left\{ \frac{H'}{H} + \alpha \, \frac{\Delta_1}{H} - \sqrt{\left[\frac{H'}{H} + \alpha \, \frac{\Delta_1}{H} \right]^2 - \frac{4\Delta_1 H'}{H^2}} \right\} \qquad (7.13)$$

where

$$\alpha = 1 + \frac{q'_B \, (1 - I)}{2q_w \left(\frac{H}{R} \right)} \qquad (7.14)$$

For times after the mass stratified layer has reached the bottom of the heated length, Eq. (2.12) for the surface temperature rise with a turbulent boundary layer remains the same, while Eq. (2.8) for the bottom temperature rise becomes

$$\frac{T_B - T_0}{\left(\frac{q_w H}{k} \right)} = \frac{\phi_H}{\left(\frac{q_w}{q'_B} \right) Pr \left[\left(\frac{H'}{H} \right) - \left(\frac{\Delta_2}{H} \right) \right]} \qquad (7.15)$$

These equations were applied to all of the nonboiling data, with a value of I chosen to agree most consistently with the experimental results. The Model II analysis (Subsection 2.1.2) is not considered here since it was found to provide poorer agreement with the noncryogenic as well as cryogenic experimental data.

Some runs in the Martin sidewall heating tests, conducted with the ullage pressure held constant, were continued long enough so that the predicted surface temperature exceeded the imposed surface boundary condition that $T_{surface} = T_{saturation} = T_S$. When this situation occurred, the fixed saturation temperature was used in Eq. (7.12) instead of the value obtained from either Eq. (2.5) or Eq. (2.12). These predictions are labeled "$T_{surf} = T_{sat}$".

Liquid Hydrogen Boiling Correlations. A limited literature survey was undertaken to obtain nucleate boiling heat-transfer coefficients and to determine the inception point of the nucleate boiling regime. The wide disparity among the data considered presented a problem in choosing a single correlation to be used in the analysis of the stratification data. Three different nucleate boiling relations, which bracket the experimental data, therefore were chosen to be used with the analysis of the boiling boundary layer effects on stratification, described in Subsection 6.1.2. These boiling curves are shown in Fig. 7-5; the data on which they are based were obtained from Refs. 17 through 22 and are discussed more thoroughly in Ref. 23. A comprehensive literature survey of cryogenic boiling data and correlation methods was subsequently published in Ref. 24, in which more definitive information was not reported.

In addition to the curves shown in Fig. 7-5, an expression defining a transitional heat-transfer coefficient was used to provide a smooth change from the subcooled, nonboiling, free-convection, heat-transfer coefficient to the subcooled nucleate boiling coefficient. These transitional curves are used for $0 < T_{w_c} - T_{sat} < \Delta T_{crit}$ and are simply the weighted average of the boiling and nonboiling heat-transfer coefficients.

$$h_{TR} = h_c + \left(h_b - h_c\right)\frac{T_{w_c} - T_{sat}}{\Delta T_{crit}} \qquad (7.16)$$

where

$$h_c = \frac{q_w}{\left(T_{w_c} - T_B\right)} \qquad (7.17)$$

$$h_b = \frac{q_w}{\left(T_{w_b} - T_{sat}\right)} \qquad (7.18)$$

7-24

$q_w \propto (T_{w_b} - T_{SAT})^{2.2}$; BASED ON FORSTER-ZUBER THEORY (REF.21)

$q_w \propto (T_{w_b} - T_{SAT})^{3.2}$; BASED ON McNELLY CORRELATION (REF. 22)

$q_w \propto (T_{w_b} - T_{SAT})^{4.8}$

p = 4 ATM

p = 1 ATM

PRESSURE DEPENDENCE BASED ON DATA OF CLASS, ET AL. (REF. 17)

TURBULENT FREE CONVECTION CORRELATION OF McADAMS, 1 ATM (REF. 25)

HEAT FLUX (BTU/FT²-HR)

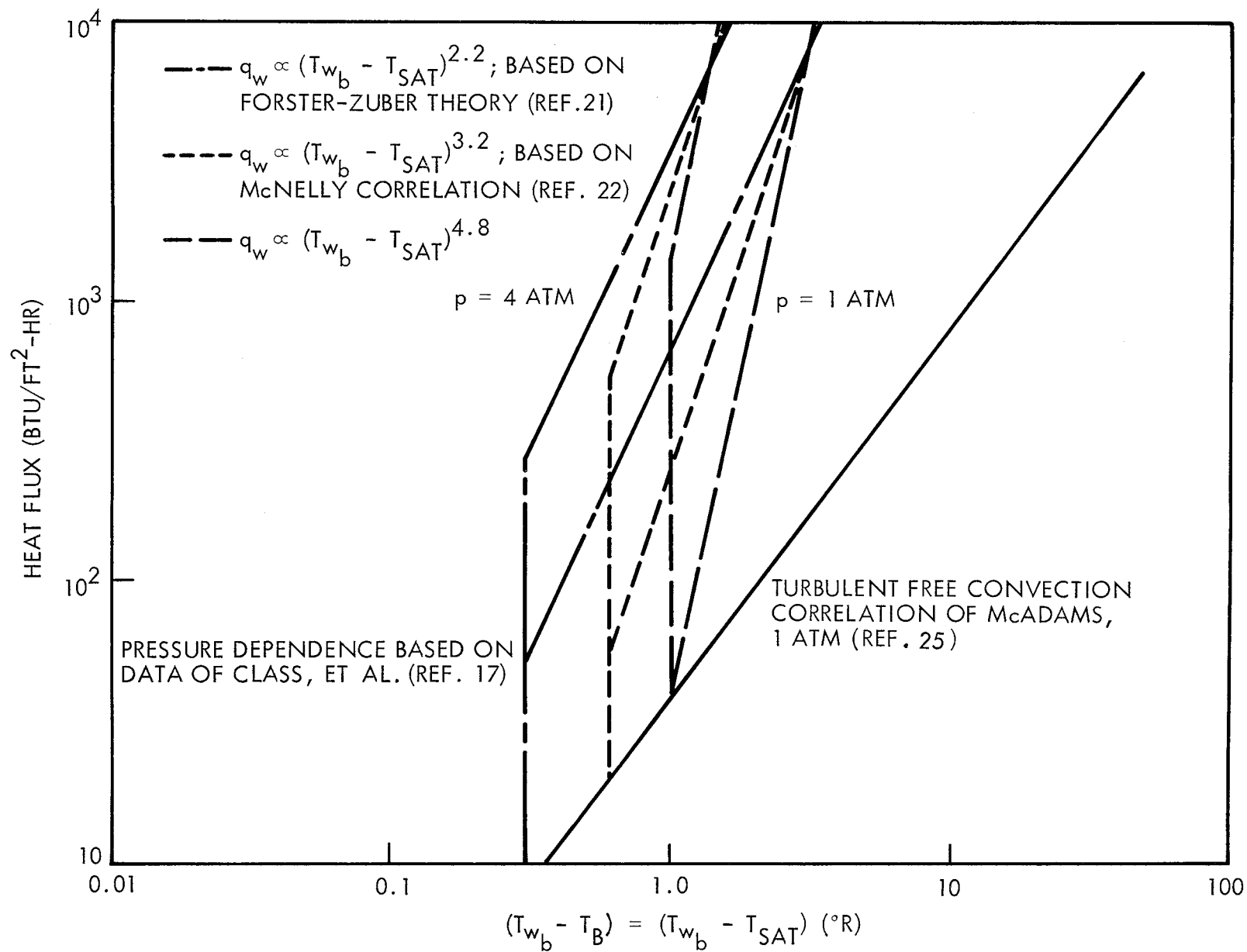$(T_{w_b} - T_B) = (T_{w_b} - T_{SAT})$ (°R)

Fig. 7-5 Liquid-Hydrogen Boiling Heat-Transfer Relations Assumed for Prediction of Stratified Layer Growth

and ΔT_{crit} is the critical superheat required for the initiation of nucleate boiling according to the three curves chosen in Fig. 7-5 (0.3, 0.6, or 1.0°R). The free-convection wall temperature below the stratified layer T_{w_c} was calculated from McAdams' correlation (Ref. 25) which may be written

$$T_{w_c} = T_B + 4.62 \, \frac{q_w H}{k} \left(Gr_H^* \, Pr \right)^{-1/4} \tag{7.19}$$

and which is independent of run length. This equation is also represented in Fig. 7-5 for LH_2 at 1 atm. The bulk (bottom) temperature T_B is obtained from the nonboiling integral analysis, and the saturation temperature T_{sat} is obtained from the measured tank pressure.

Integral Analysis with Boiling. Equations have been developed in Subsection 6.1.2 for predicting the hydrodynamic stratified layer thickness for a tank with nucleate boiling in the free-convection boundary layer. For cases where boiling has been calculated to exist in the unstratified liquid, Eq. (6.34) was used to obtain the mass stratified layer growth. It is realized that this simplified version of the more general relation, Eq. (6.33), may be somewhat in error for liquid hydrogen, but data have not been found which provide the necessary information on void fraction. In any case, the time required to stratify the tank is so small that a difference of a factor of two or three would not significantly change the results.

Because boiling causes the mass stratified layer to reach the tank bottom ($\Delta_1/H = 0.95$) so quickly, a problem is encountered in calculating the surface temperature.* Equation (2.12) for the surface temperature rise after the mass stratified layer has reached the tank bottom is based on data obtained under nonboiling conditions. It was found that this correlation does not apply when boiling causes a very rapid stratified layer growth.

---

*Surface temperature as used in this section means the maximum temperature in the bulk temperature profile, excluding surface mass and energy transfer effects which are imposed by fixed ullage conditions and which affect only a thin liquid layer at the surface.

An alternate method for correlating the surface temperature is to use the equation which would have applied had the liquid been sufficiently subcooled to prevent boiling, and to set (Δ_1/H) equal to the boiling value. This method is called the "modified boiling" correlation; in most cases, the surface temperature would be determined from Eq. (2.5) with $(\Delta_1/H) = 1$. Equation (7.13) thus would become

$$\frac{\Delta_2(t)}{H} = \frac{1}{2}\left[\frac{H'}{H} + \alpha - \sqrt{\left(\frac{H'}{H} + \alpha\right)^2 - 4\frac{H'}{H}}\right] \tag{7.20}$$

where α is the same as in Eq. (7.14). The equation for the bottom temperature rise, Eq. (7.15), remains the same. As in the nonboiling correlations, the predicted surface temperature is restricted to a value no higher than the known saturation temperature. The correlation is labeled "$T_{surf} = T_{sat}$" when this restriction is imposed.

In all the correlations, boiling and nonboiling, the temperature profiles were calculated from the equation

$$\frac{T - T_B}{T_S - T_B} = \left(1 - \frac{z}{\Delta_2}\right)^{(1/I) - 1} \tag{7.21}$$

where z is the axial distance from the liquid surface. There is no restriction in the integral analysis that requires use of this particular profile; any shape may be used that satisfies the conditions that $T = T_S$ at $z = 0$, $T = T_B$ at $z = \Delta_2$, and

$$\int_0^1 \left(\frac{T - T_B}{T_S - T_B}\right) d\left(\frac{z}{\Delta_2}\right) = I .$$

7.3.2 Correlation Results

In this section the correlations between the experimental LH_2 stratification data and the integral analysis are presented and discussed. Not every test run will be discussed in detail; only typical data and those runs which illustrate a specific point will be

considered. In each case, the values of heat flux shown on the accompanying figures represent the average from the start of the test; thus they will be different from the values shown in the tables for specific time intervals. The Grashof number values indicated on the figures are average values. Solid symbols represent the saturation temperature (based on the measured tank total pressure) located at the liquid surface, as calculated by the energy balance program, assuming no mass transfer.

Lockheed Data. Typical stratification temperature data are compared with the integral technique bottom heating correlation in Figs. 7-6 through 7-8. The passively pressurized runs not shown give substantially the same results; the passive pressurization* was rapid enough to prevent boiling in the boundary layer shortly after the start of each run. An energy integral of 0.4 was found to correlate the data most consistently. The large temperature gradients at the liquid surface are believed to be caused by energy transfer from the ullage. An initial layer of condensed pressurant, as implied by the energy balance results, could explain these large gradients. Better correlation could be obtained early in the run if the effective starting point of the free-convection boundary layer was assumed to be above the bottom of the cylindrical portion of the tank wall. However, independent data to justify such an assumption are not available. It is possible that turbulence created by the bulk boiling prior to pressurization may have caused a significant transient in the formation of a stable boundary layer on the tank wall. The agreement of the analysis with the data is seen to be better at later times when the effect of such a transient would be less noticeable. In Fig. 7-8, it is significant to note that, of the bulk temperature rise of 0.19° R at 300 sec, 0.13° is caused by compression of the liquid, and only 0.06° R by heat addition.

From the noncryogenic fluid results discussed in Subsection 2.2.2, it is indicated, for modified Grashof numbers greater than 10^{13} and for a bottom heat flux equal to the sidewall heat flux, that the energy integral may be lower than the value of 0.6 determined for cases without bottom heating (Fig. 2-5). This was confirmed by the cryogenic stratification data which indicated an energy integral of 0.4.

---

*It should be remembered that the passive pressurization of this tank is believed to have been controlled by mass and heat transfer from outside the tank, rather than from the liquid in the tank.
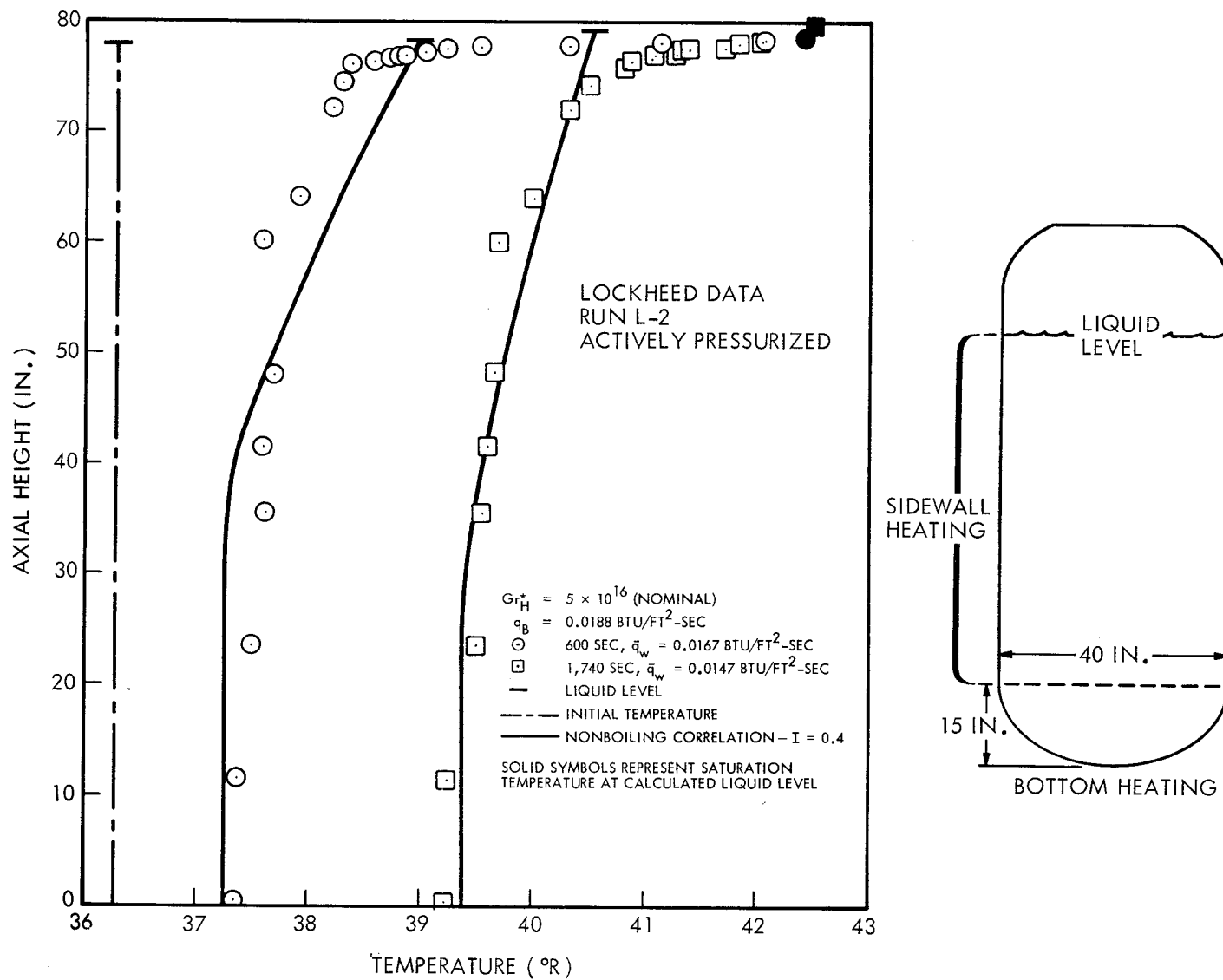
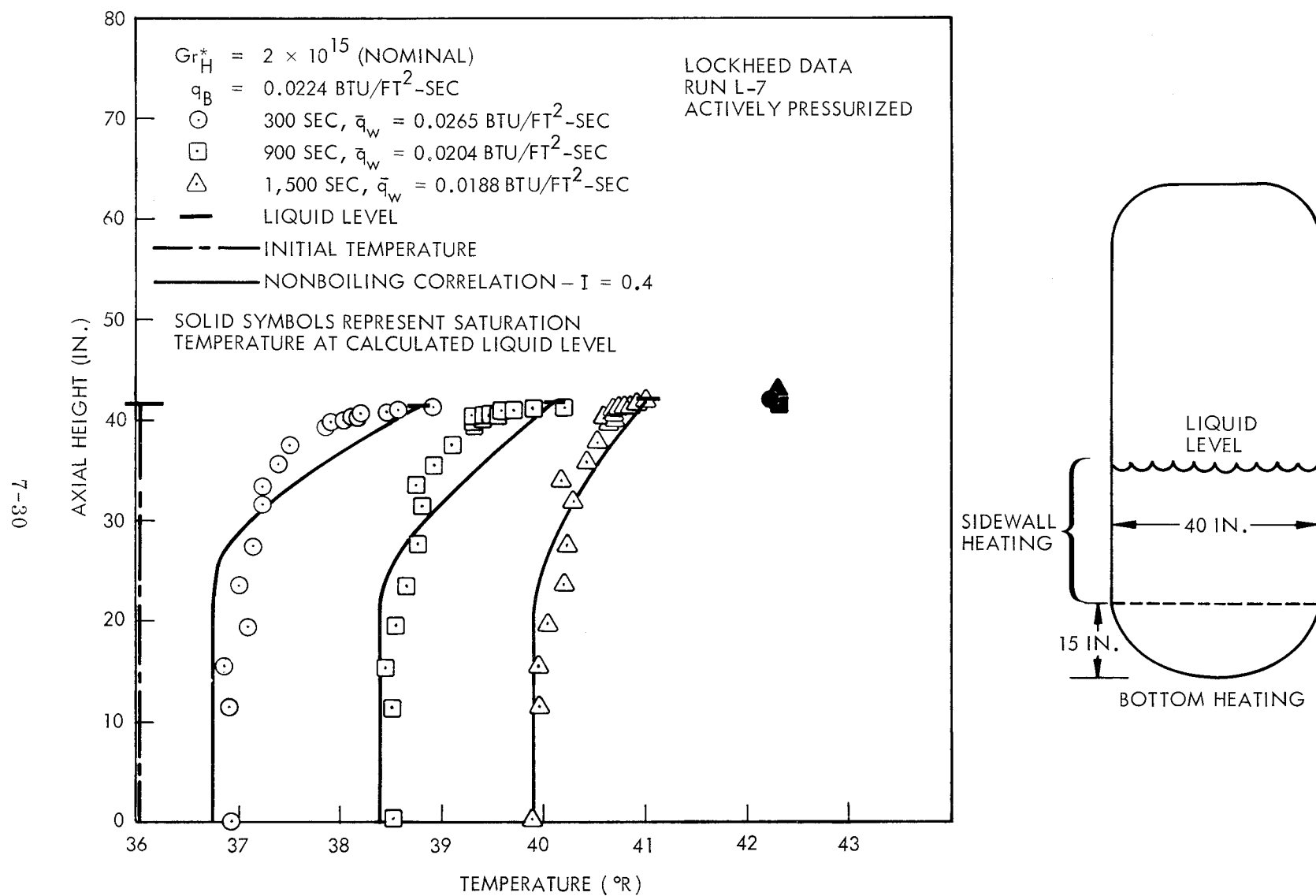Fig. 7-6 Temperature Stratification Correlation for Liquid Hydrogen

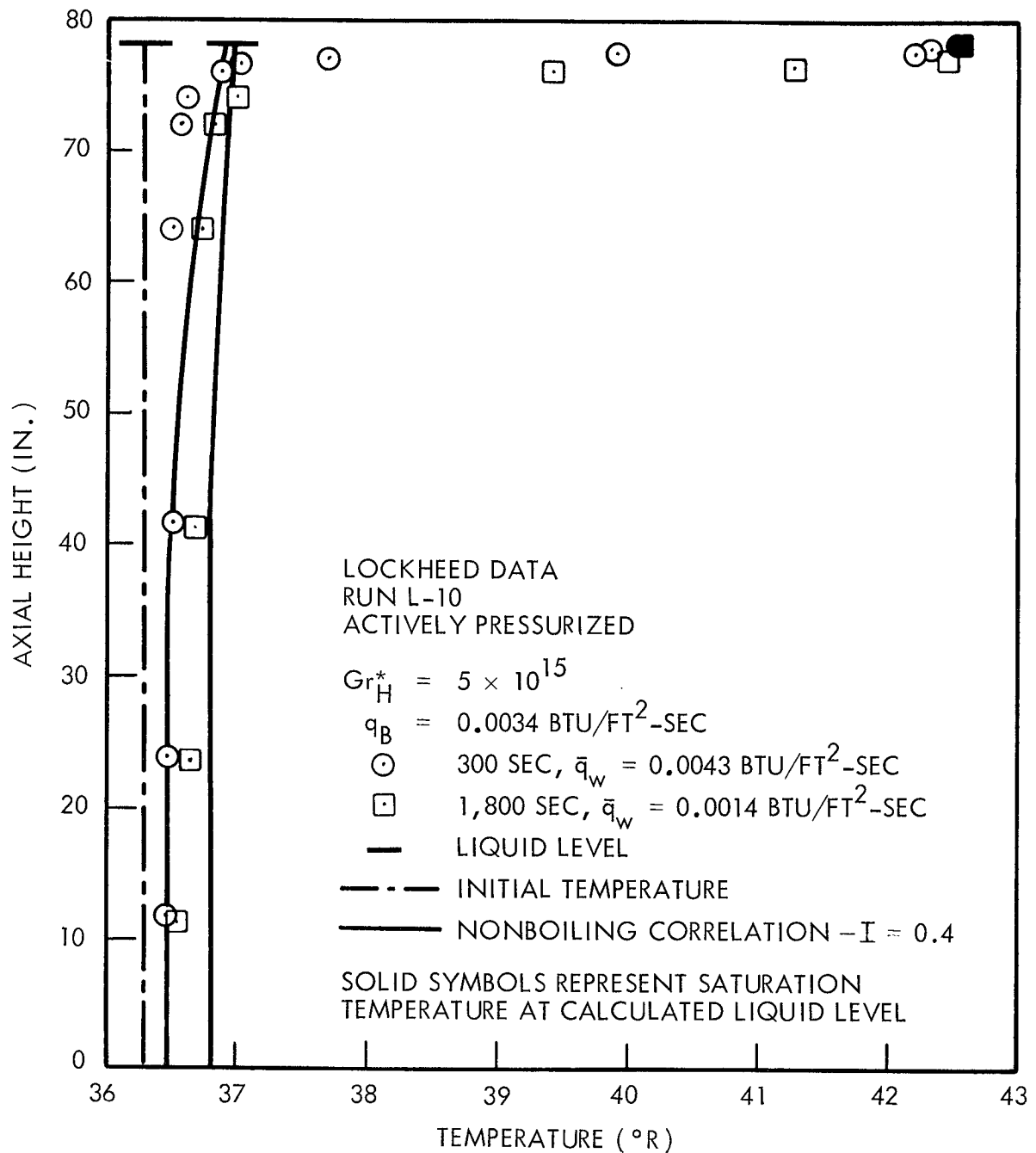Fig. 7-7 Temperature Stratification Correlation for Liquid Hydrogen

Fig. 7-8 Temperature Stratification Correlation for Liquid Hydrogen

7-31

MSFC Data. Data from the full-scale S-IV tank tests are shown in Figs. 7-9 through
7-11. Excellent agreement with the integral correlation is obtained if the bottom heat
flux is assumed to be equal to the sidewall heat flux, and an energy integral of 0.4 is
used. The data have been adjusted to yield uniform initial temperatures, as described
in Subsection 7.2.2. These three runs are typical of those listed in Table 7-2. As in
the Lockheed tests, only a thin layer of liquid at the surface is affected by mass and
energy exchange with the ullage, and boiling below the stratified layer was suppressed
shortly after the start of each run. It is not known to what extent the passively pres-
surized runs may have been controlled by energy transfer from sources other than the
liquid. No appreciable difference in liquid temperatures was observed between hydro-
gen-, helium-, and passively-pressurized runs. The S-IV tank data further support
the lower values of the energy integral indicated for stratification with approximately
equal bottom and sidewall heat fluxes.

Martin Sidewall Heating Data. Typical results from the Martin stratification tests
without bottom heating are presented in Figs. 7-12 through 7-18. Runs M-1 and M-1A
(Figs. 7-12 and 7-13) show good agreement with the modified boiling correlation with
$I = 0.6$ or 0.7 until the surface temperature is restricted by the ullage conditions.
After that time, with $T_{surf} = T_{sat}$, the energy integral increases with time to
approach a value of unity. Runs M-2 through M-5 are suspected of having erroneous
temperature measurements at two locations, and are therefore not presented here.
They also would generally agree with the modified boiling correlation if the two ques-
tionable temperature measurements in these runs were corrected.

Figures 7-14 through 7-17 show the degree of correlation obtained as the heat flux is
increased from the minimum level to the maximum level for this test program. Runs
M-8 and M-10A show good agreement with the nonboiling correlation and $I = 0.7$;
Runs M-11 and M-12 are in agreement with the modified boiling correlation until
$T_{surf} = T_{sat}$. The maximum calculated wall superheat for Run M-10A was $0.11°$ R
at 360 sec, and the minimum for Run M-11 was $2.98°$ R at 60 sec. This implies that
the inception point for nucleate boiling is somewhere between these two values. As a
further check, Run M-4 indicated agreement with the nonboiling correlation at 60 sec
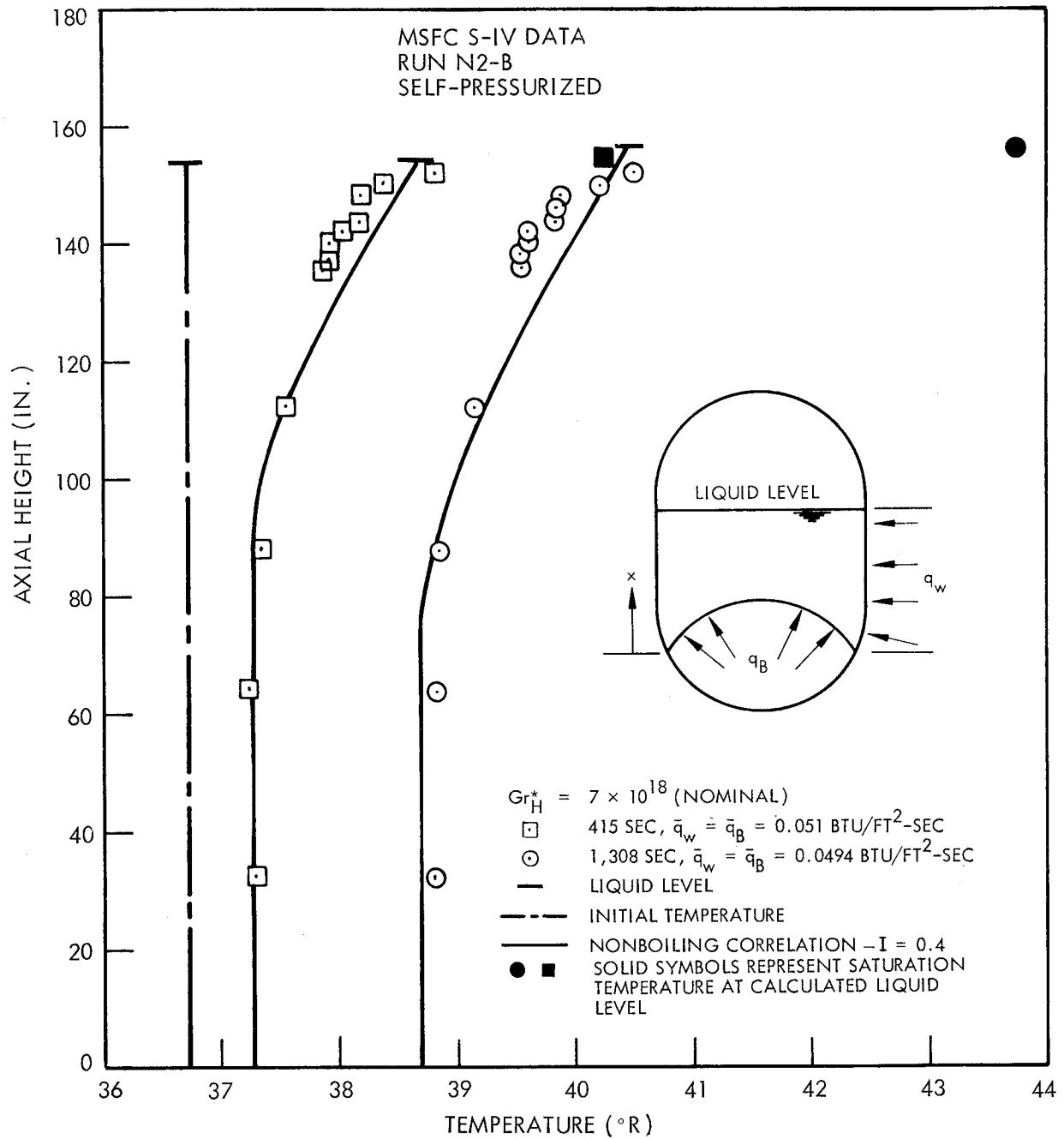
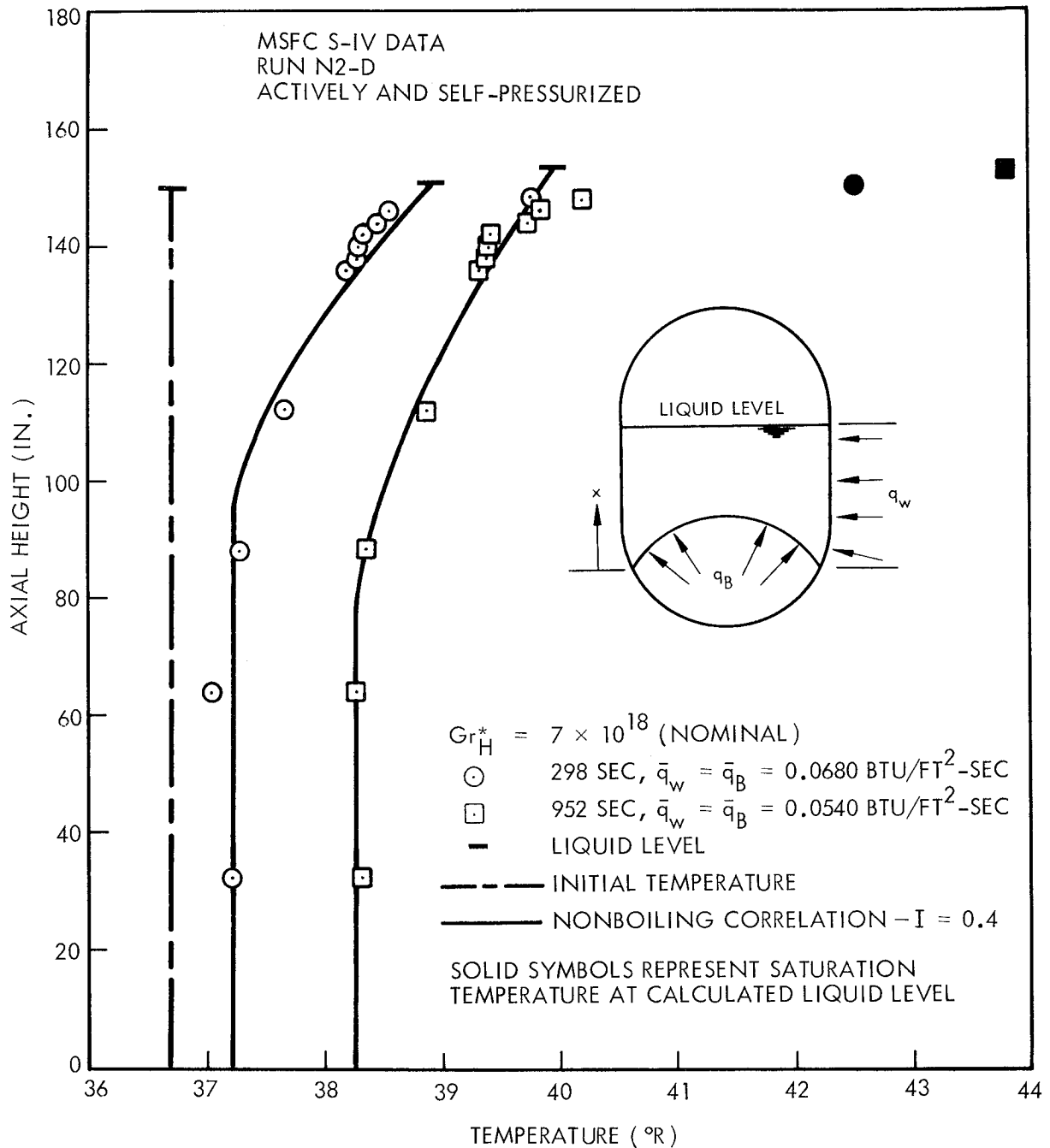Fig. 7-9 Temperature Stratification Correlation for Liquid Hydrogen

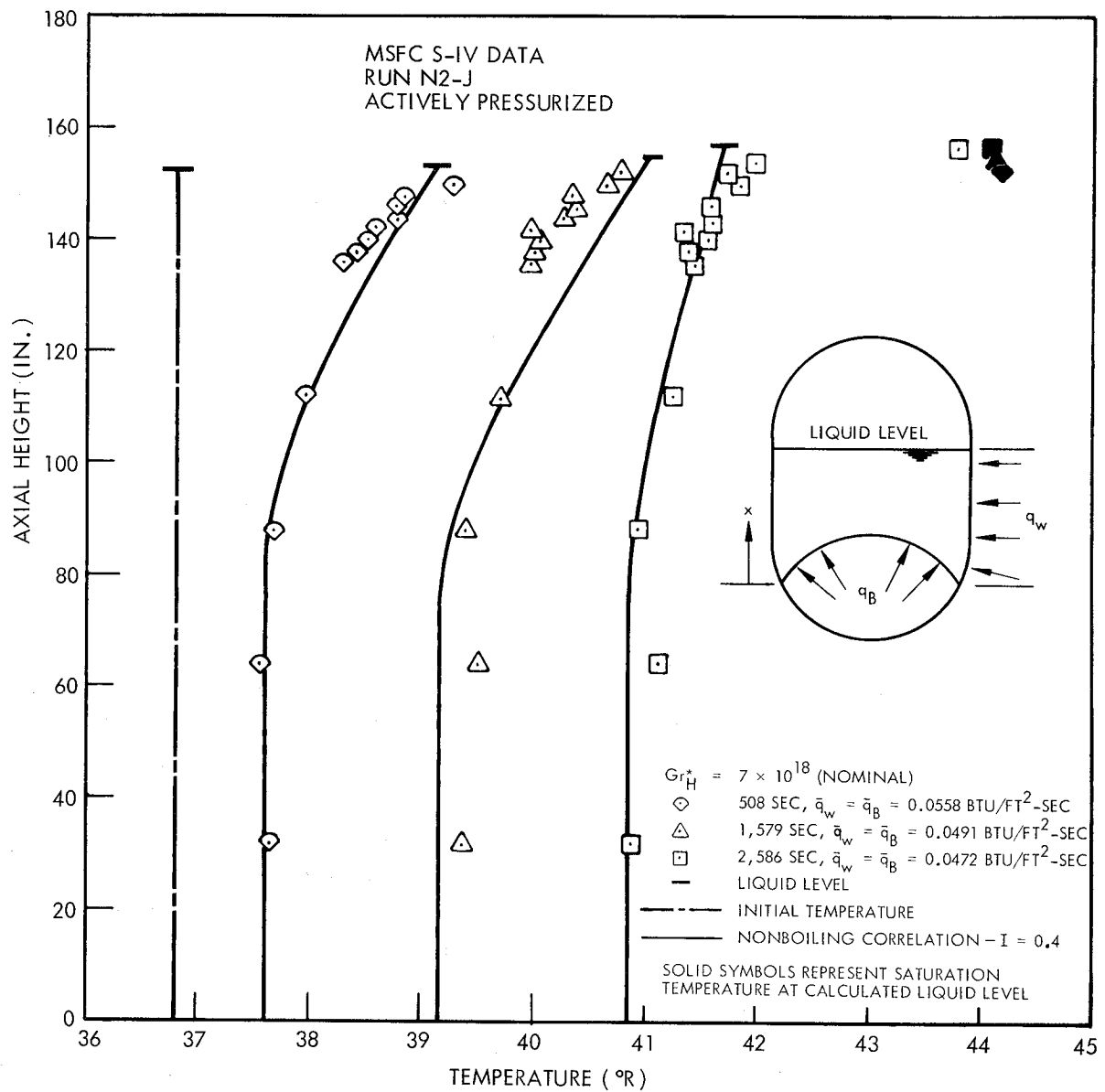Fig. 7-10 Temperature Stratification Correlation for Liquid Hydrogen

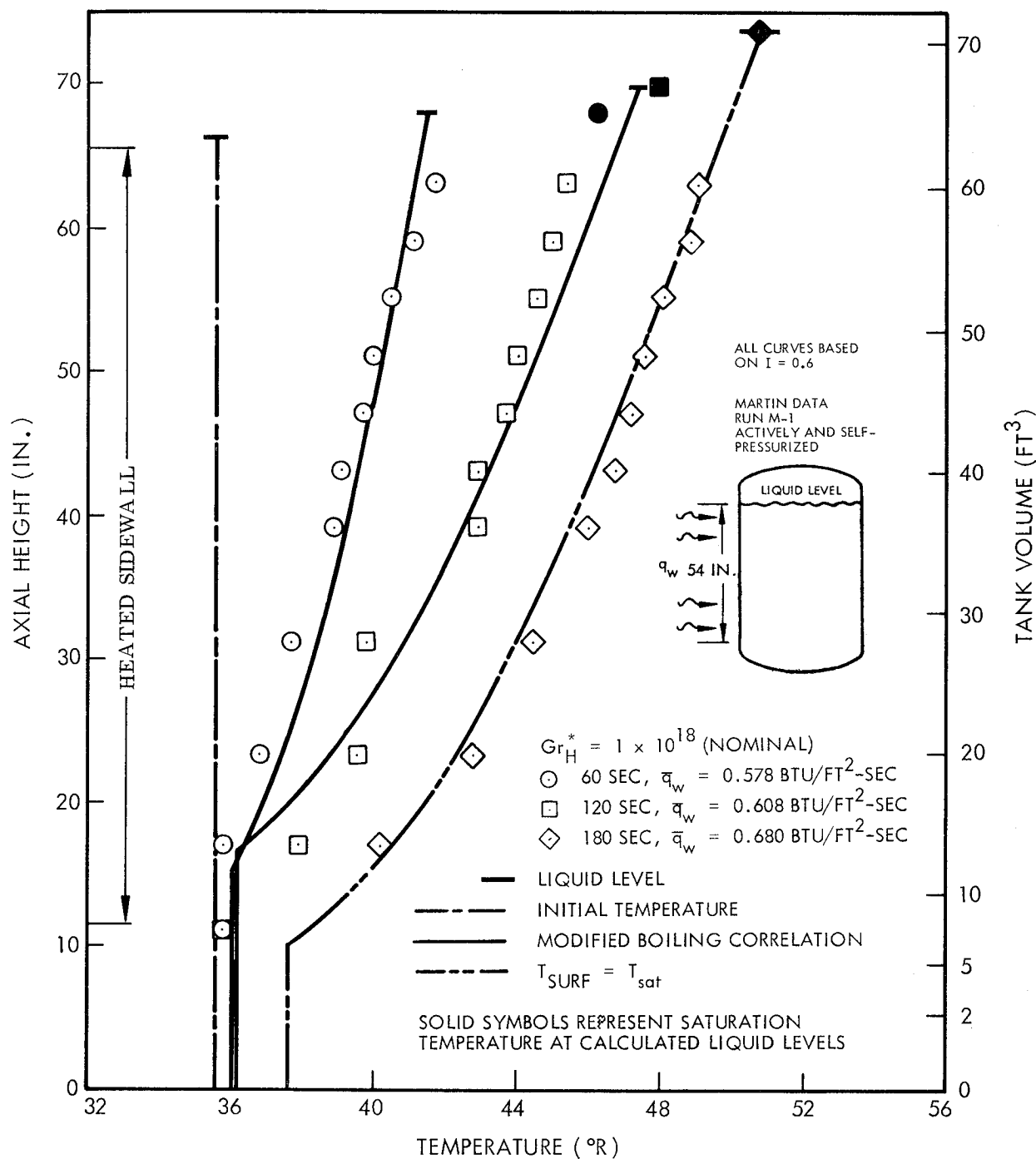Fig. 7-11 Temperature Stratification Correlation for Liquid Hydrogen

Fig. 7-12 Temperature Stratification Correlation for Liquid Hydrogen — No Bottom Heating
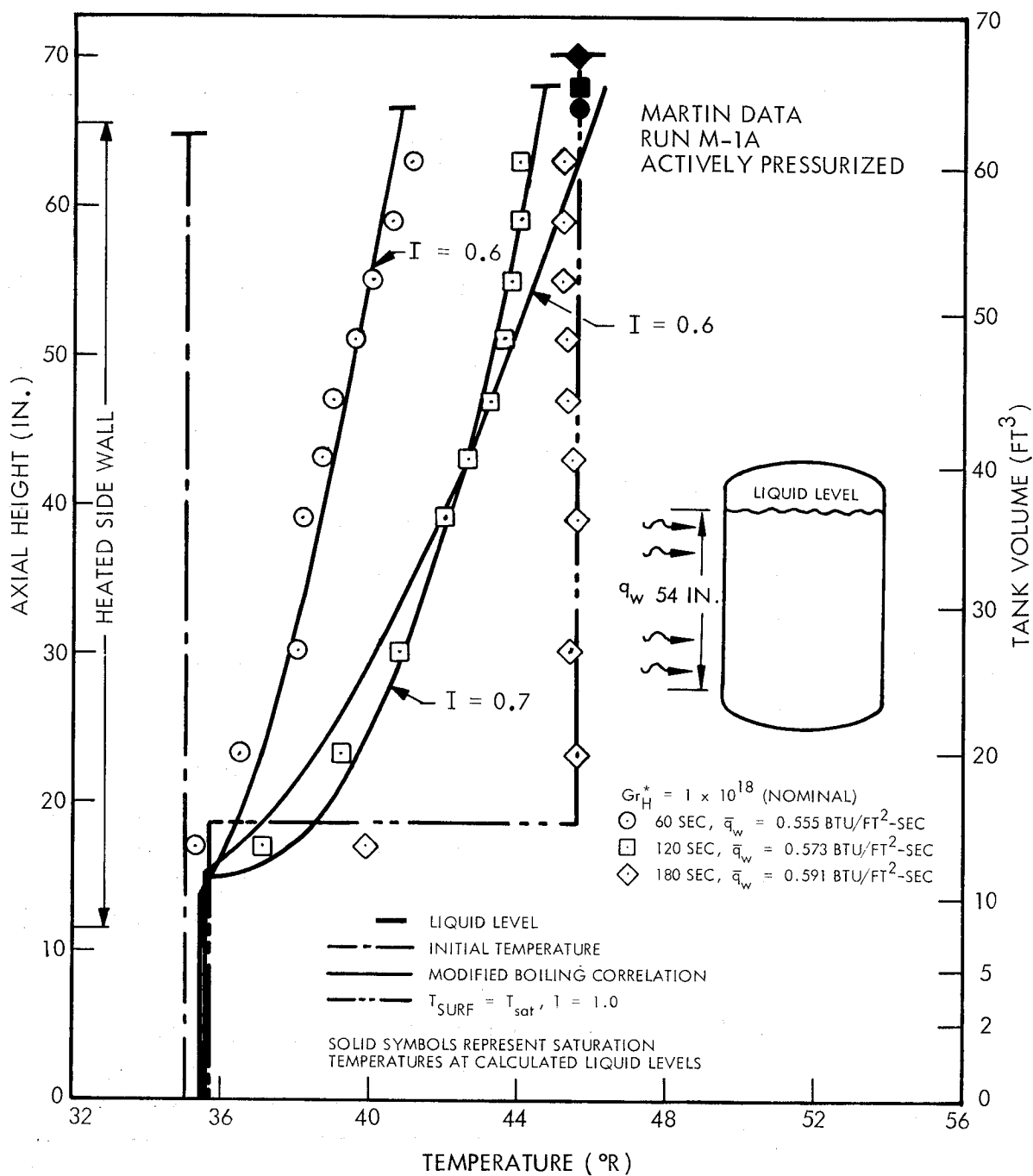
LOCKHEED MISSILES & SPACE COMPANY

Fig. 7-13 Temperature Stratification Correlation for Liquid Hydrogen—
No Bottom Heating

Fig. 7-14 Temperature Stratification Correlation for Liquid Hydrogen — No Bottom Heating
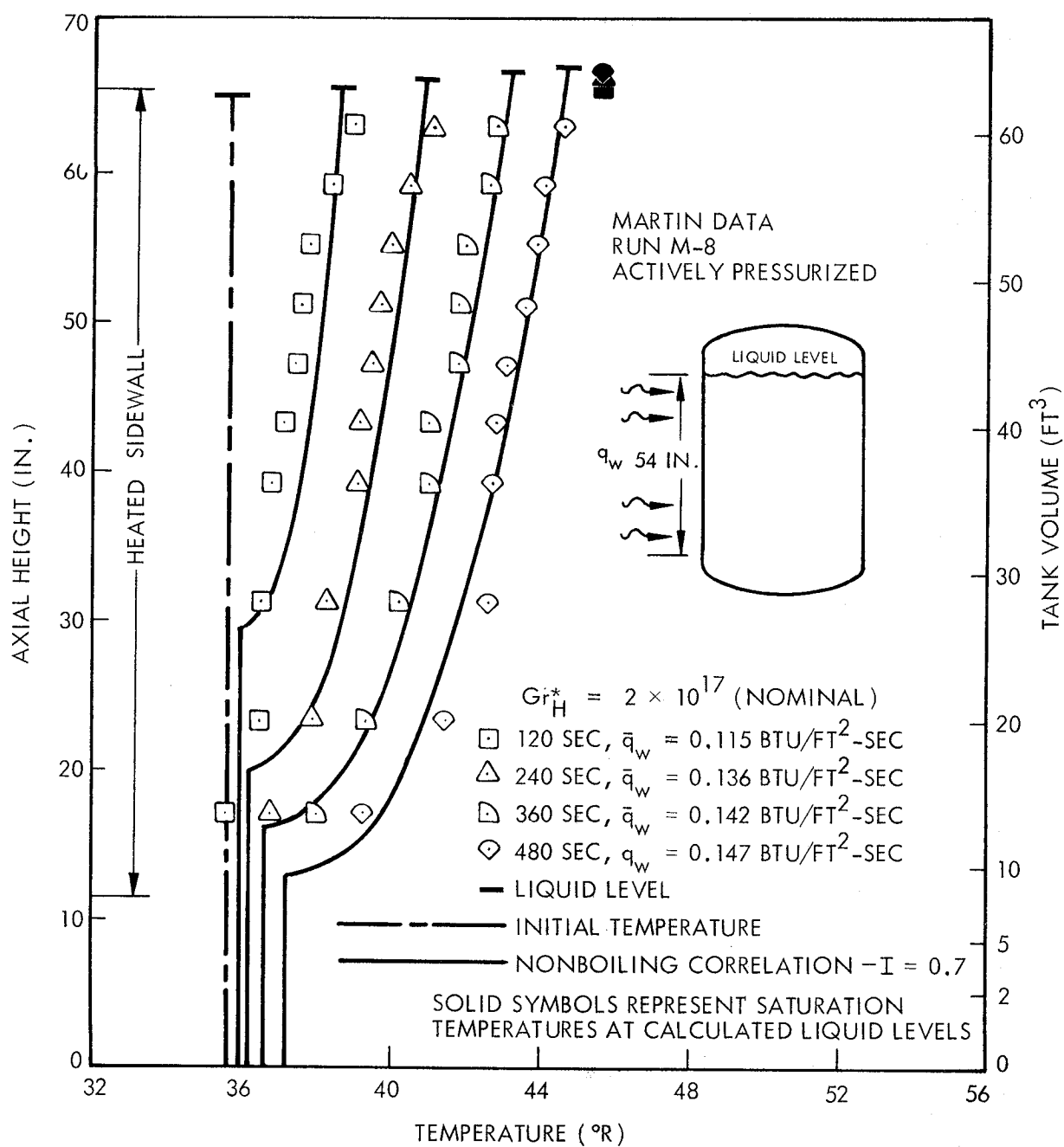
7-38

Fig. 7-15 Temperature Stratification Correlation for Liquid Hydrogen —
No Bottom Heating

LOCKHEED MISSILES & SPACE COMPANY

Fig. 7-16 Temperature Stratification Correlation for Liquid Hydrogen —
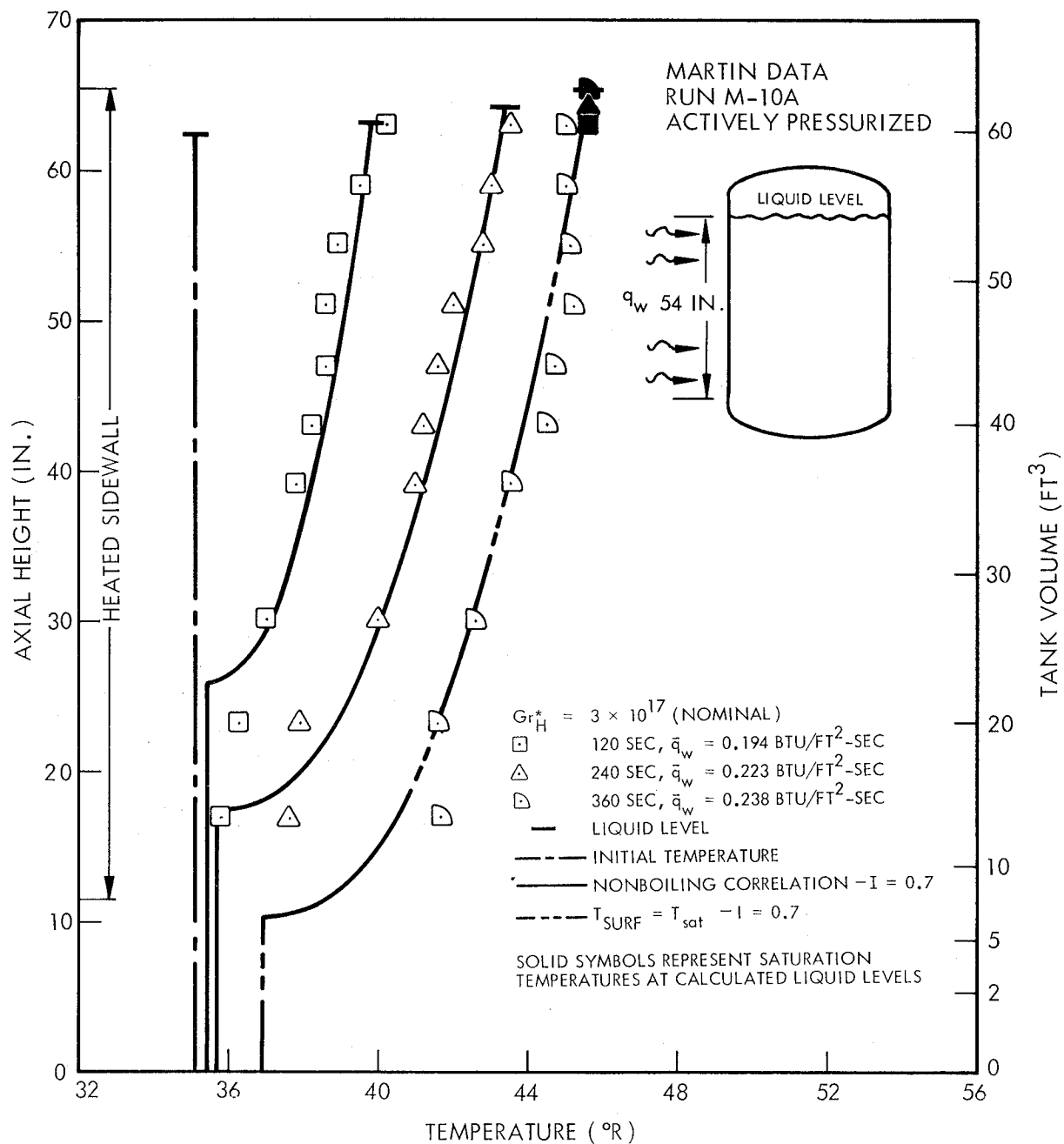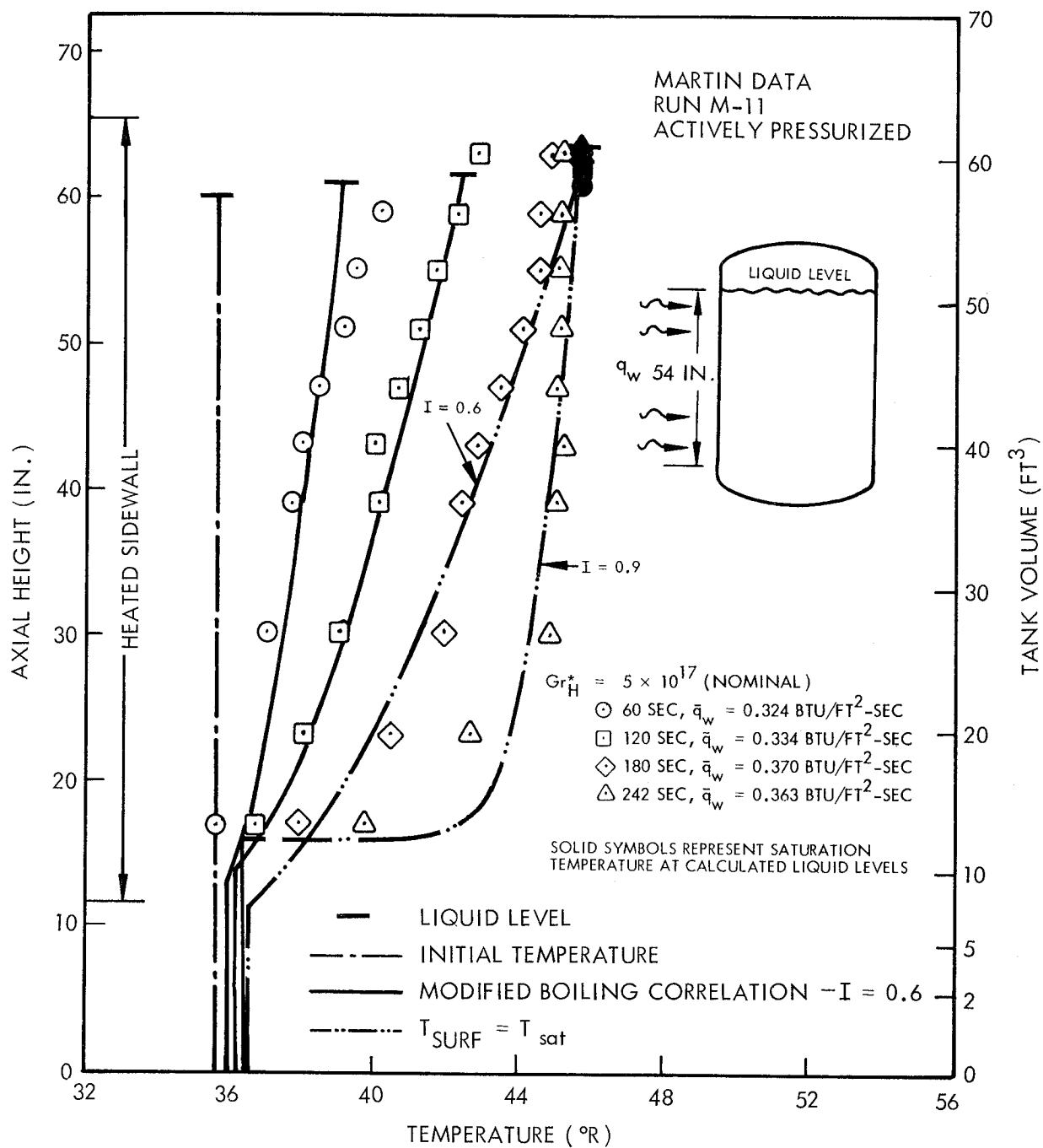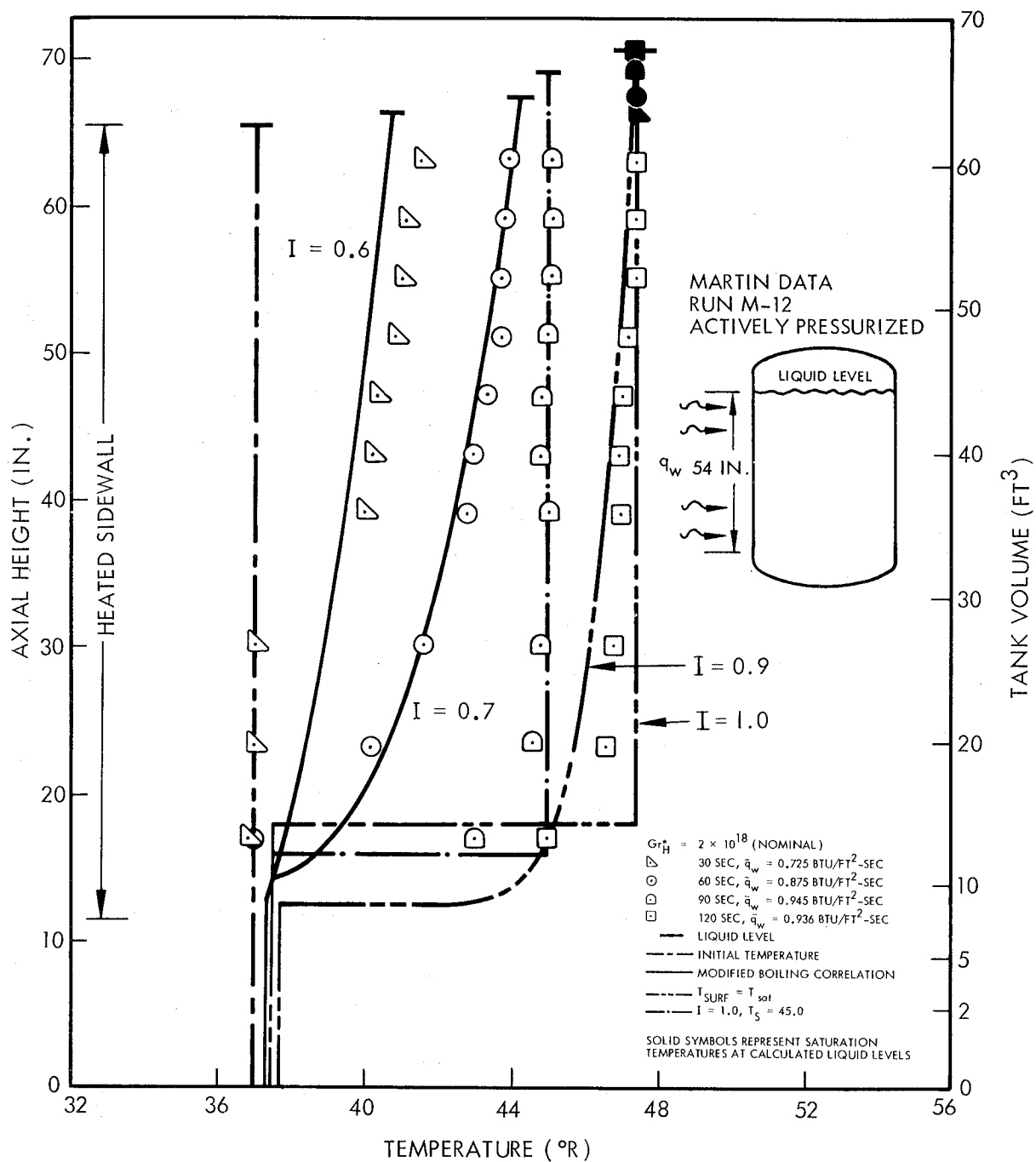No Bottom Heating

7-40

Fig. 7-17 Temperature Stratification Correlation for Liquid Hydrogen — No Bottom Heating
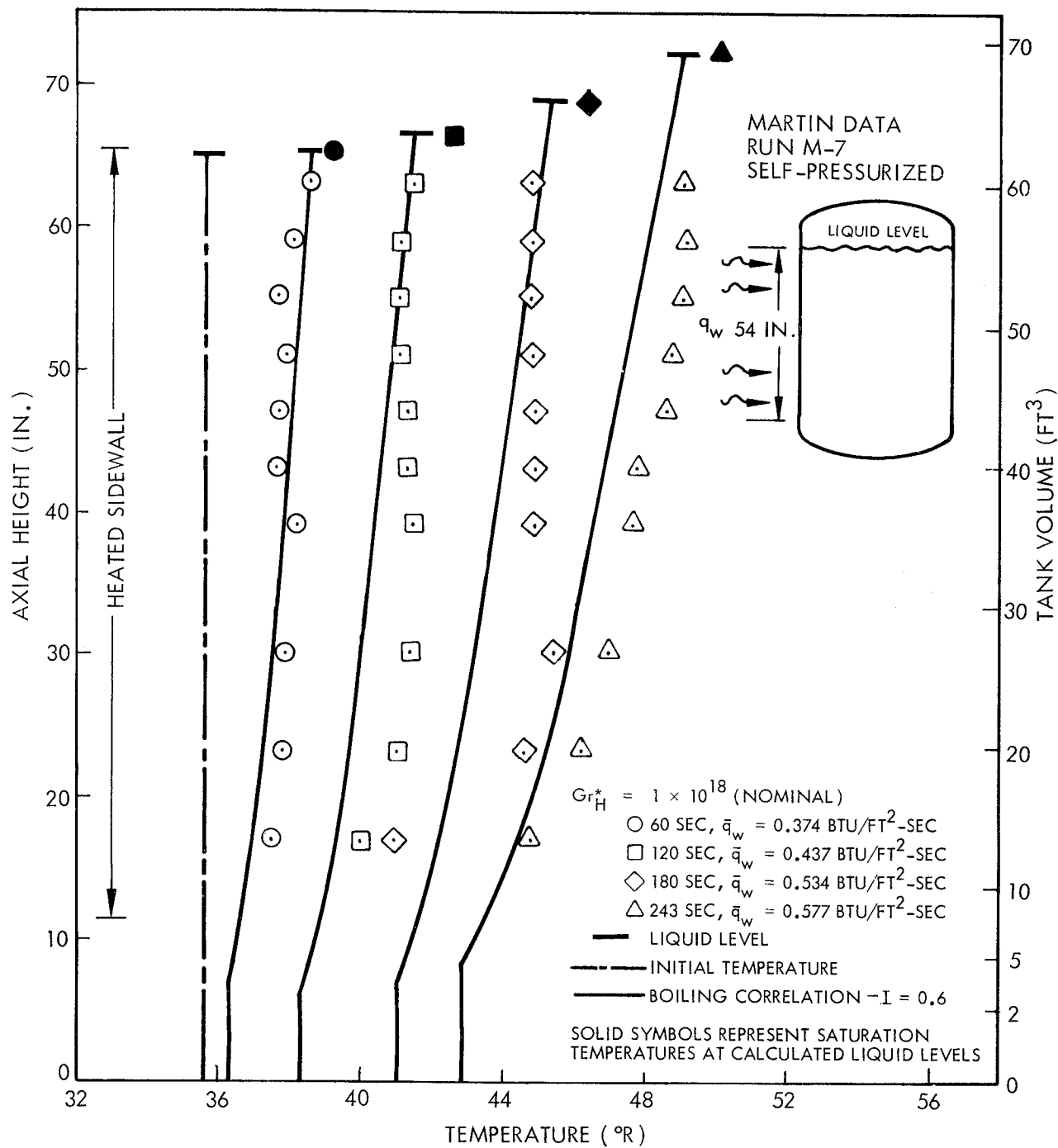
Fig. 7-18 Temperature Stratification Correlation for Liquid Hydrogen —
No Bottom Heating

with 1.03° R superheat, and a bracketing of the data by the nonboiling and modified boiling correlations at 120 sec with 3.07° R superheat. The data from that run are questionable, however, as previously mentioned. It should be pointed out that there is no experimental verification of these calculated wall temperatures, and that the net heat rates used may result in significantly lower boundary-layer temperature differences than if the gross sidewall heat rates had been known accurately and used.

It is suspected that, for the high heat flux applied in Run M-12, it was difficult to maintain a constant tank pressure manually because of the large boiloff rates. The data at 90 and 120 sec show all the characteristics of the liquid being almost completely saturated, as in Run M-1A at 180 sec, except for the difference between the uniform temperature in the liquid and the saturation temperature at 90 sec. If the saturation temperature at 90 sec was 45° R, instead of the nominally reported 47.4° R, good agreement would be obtained with $I = 0.9$ or $I = 1.0$, which would be consistent with other runs in this test series. The apparent disagreement between the data and the modified boiling correlation at 30 sec in Run M-12 is similar to the results obtained in Runs M-2 through M-5, in which the measurements at axial heights of 23.5 in. and 30 in. were suspected of being in error.

Run M-7 (Fig. 7-18) was the only entirely self-pressurized run in this group of tests, and the data appear to be well correlated with the unmodified boiling curve with $I = 0.6$. The apparent lack of an energy balance is caused by the assumption in the energy balance program that the bottom temperature rise was small; this assumption was justified in other runs where a measurement closer to the tank bottom was obtained. (See Fig. 7-12.) It is suspected that this assumption is also valid for Run M-7, in which case a large value of I (0.9 or 1.0) and a means of evaluating the surface (saturation) temperature would be required to correlate the data.

Martin Bottom Heating Data. The Martin stratification tests with the inverted false bottom may be divided into four groups, based on the four basic sidewall heating conditions. The bottom heating rates were varied within each group of tests, and all tests but one were pressurized with GHe to 30 psig.

Figures 7-19 and 7-20 show the excellent agreement obtained with I = 0.6 between the data and the nonboiling correlation in the first group of tests. In Run MB-4 at 240 sec, the modified boiling correlation is seen to be nearly the same as the nonboiling correlation with 1.02° R superheat calculated at the wall.

Typical data from the next two groups are shown in Figs. 7-21 and 7-22. The agreement is not as good, using I = 0.6, for the reduced heating levels indicated in these figures; however, a smaller value of I does not improve the correlation, as shown in Fig. 7-22. It appears that a better correlation might be obtained with I = 0.4 if the bottom heating was in fact larger than the assumed calibrated value.

Figure 7-23 shows essentially the same degree of agreement between the data and the nonboiling correlation at the lowest sidewall heating level. The large effect of energy transfer from the ullage is evident.

The only self-pressurized run with bottom heating, Run MB-16 (Fig. 7-24), agreed most consistently with the modified boiling correlation. At 120 sec, the boiling and modified boiling correlations were the same since the mass stratified layer had not reached the tank bottom at these low heat rates. At 600 sec, the modified boiling correlation was the same as the nonboiling correlation, since the stratified layer had reached the tank bottom for the nonboiling case; the boiling correlation gives a completely mixed liquid. It is interesting to note that this is the only run in which the choice of the nucleate boiling correlation (Fig. 7-5) makes any appreciable difference in the boiling or modified boiling stratification correlation.

In the Martin bottom heating tests, the ratio of bottom to sidewall heat flux was less than one, and the energy integral values of 0.6, as indicated by the data, are consistent with the correlation of I based on noncryogenic fluids without bottom heating.
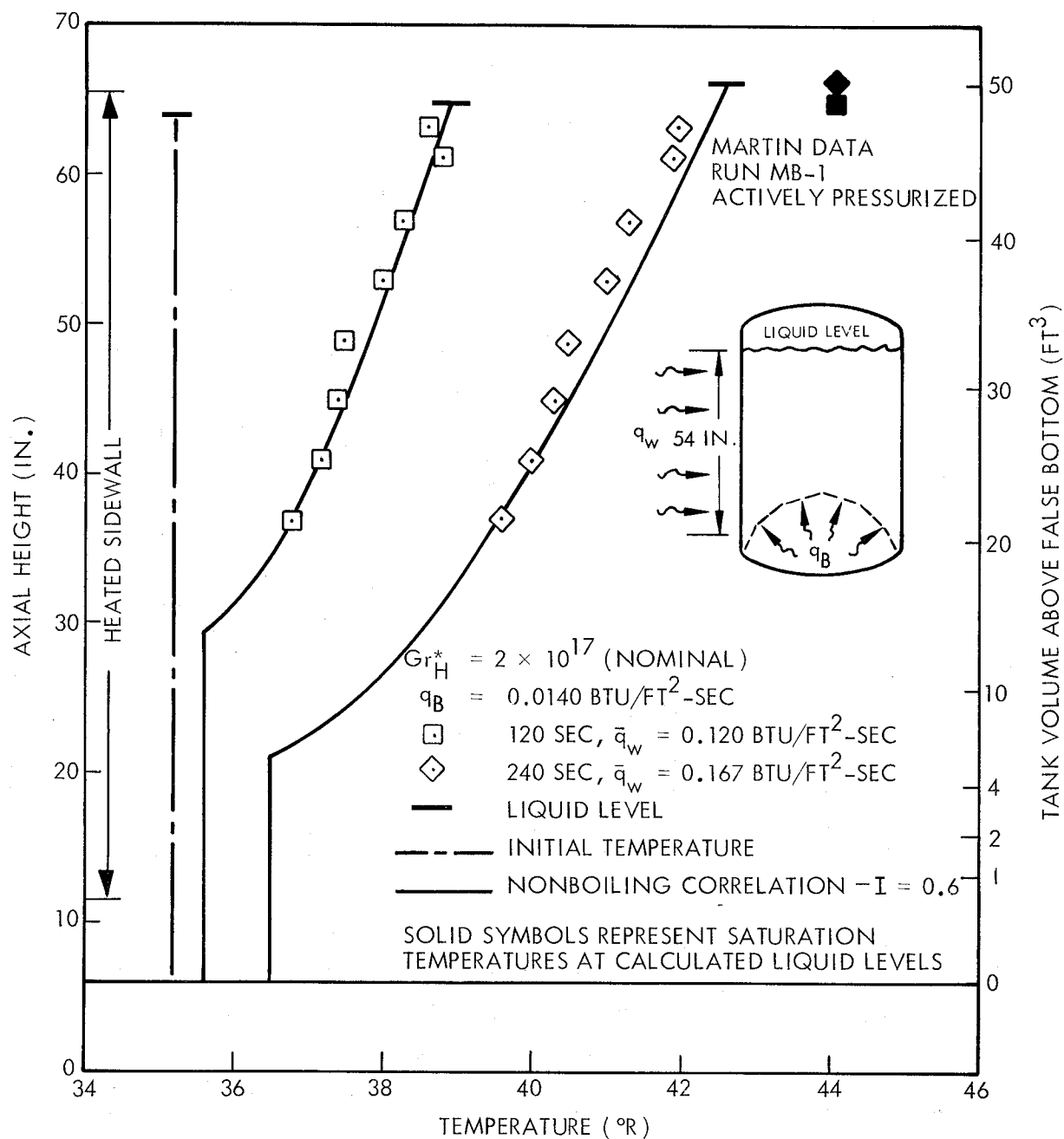
Fig. 7-19 Temperature Stratification Correlation for Liquid Hydrogen —
Bottom Heating

Fig. 7-20 Temperature Stratification Correlation for Liquid Hydrogen—
Bottom Heating

Fig. 7-21 Temperature Stratification Correlation for Liquid Hydrogen — Bottom Heating
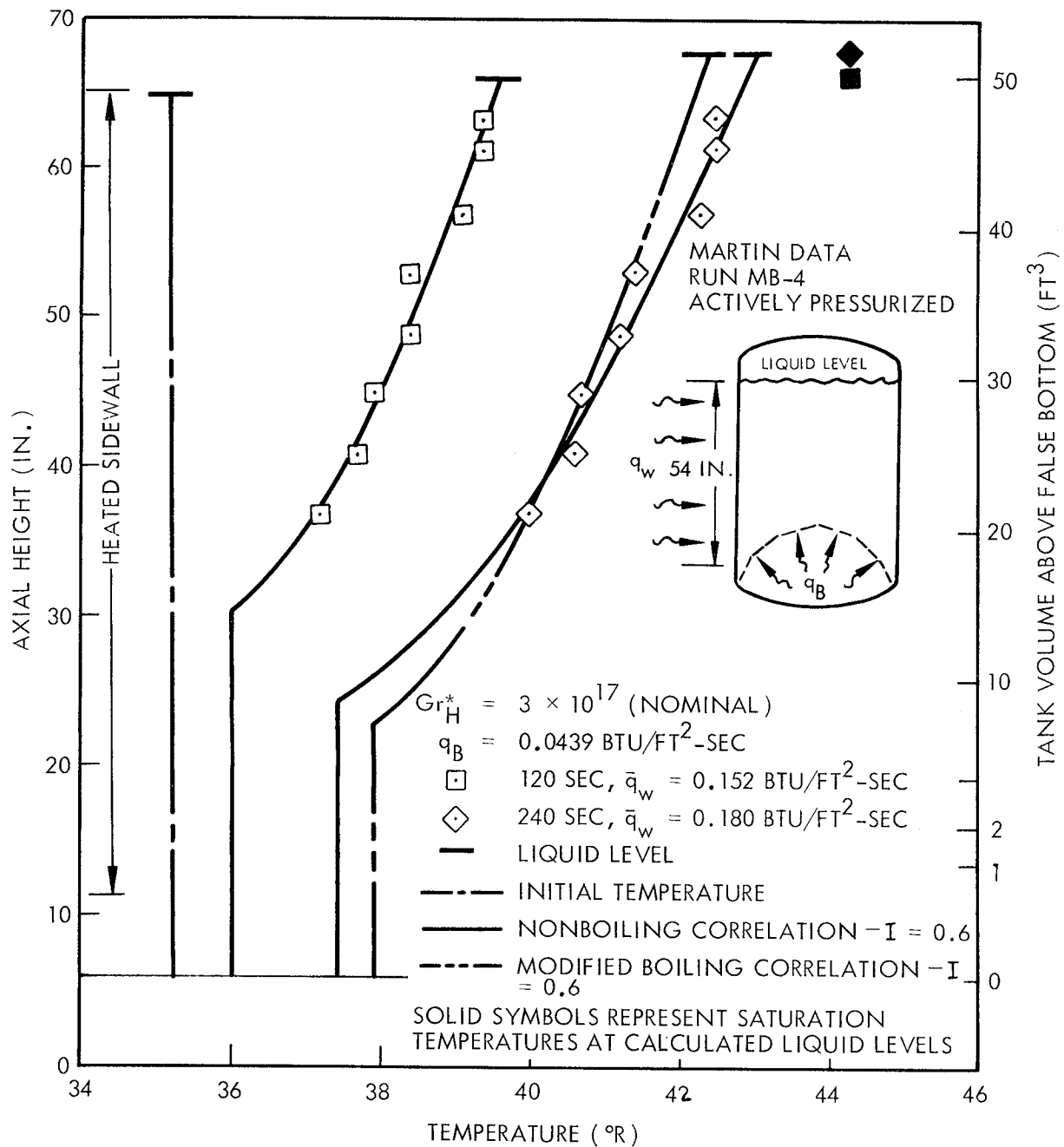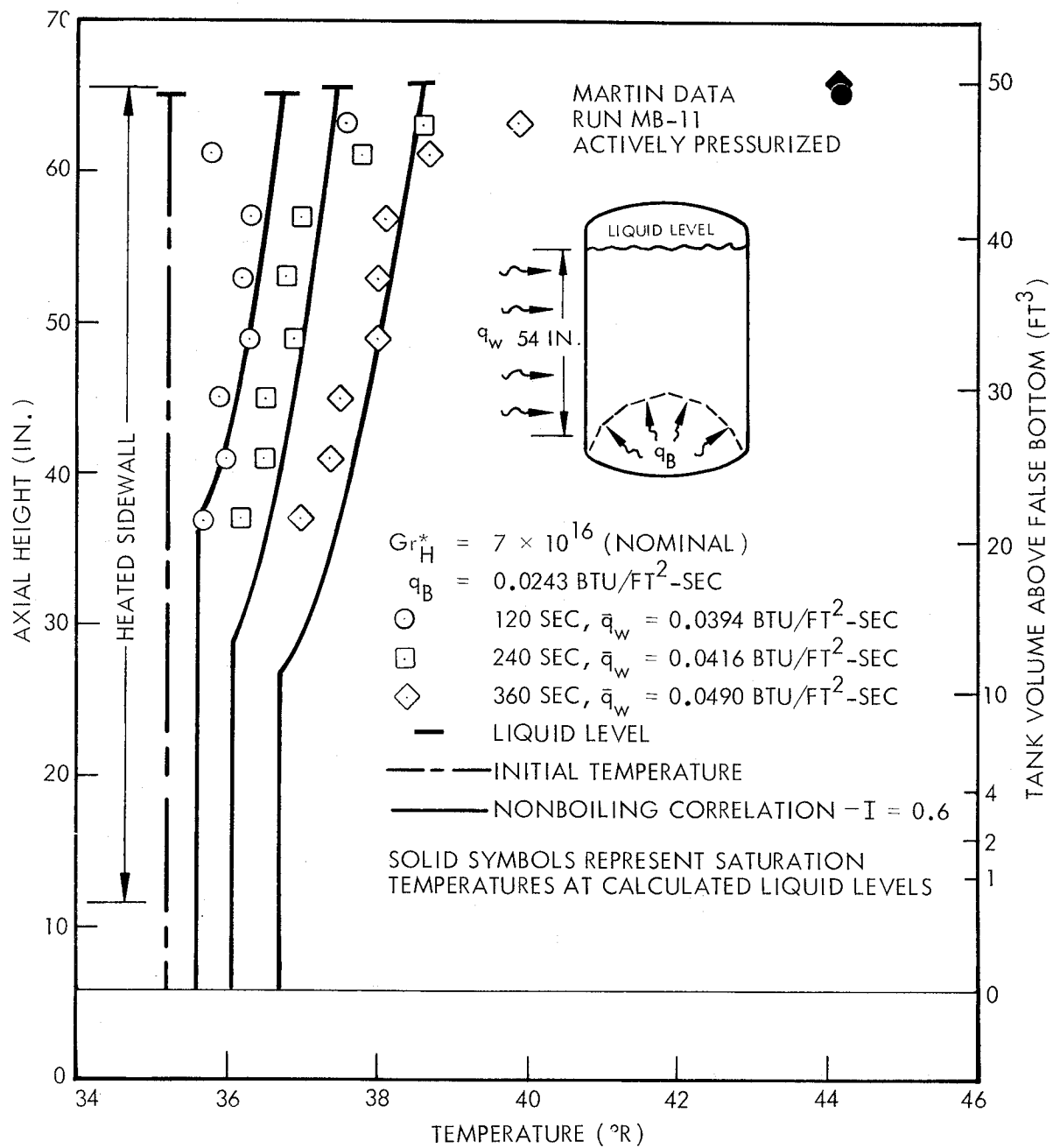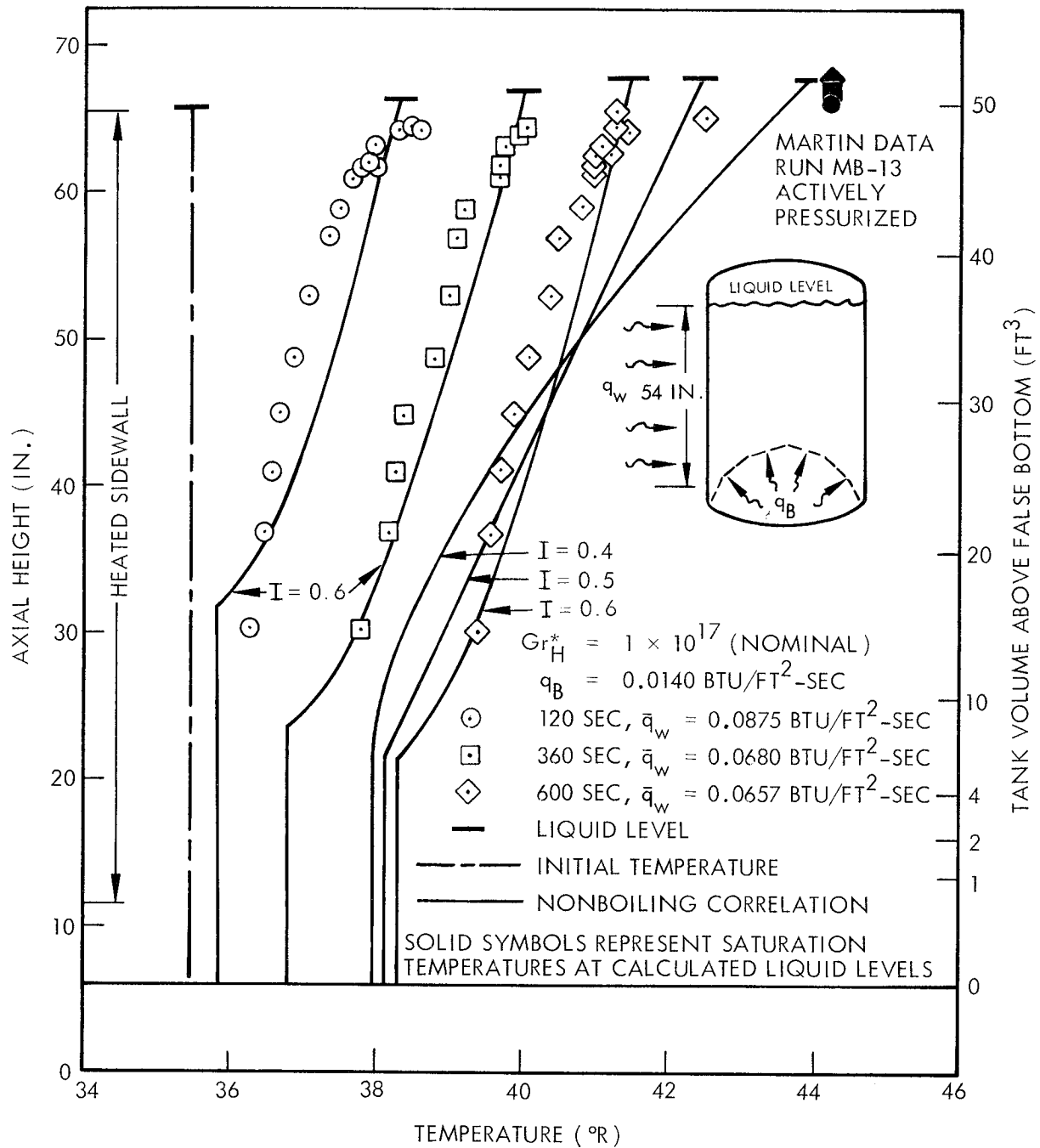
Fig. 7-22 Temperature Stratification Correlation for Liquid Hydrogen −
Bottom Heating
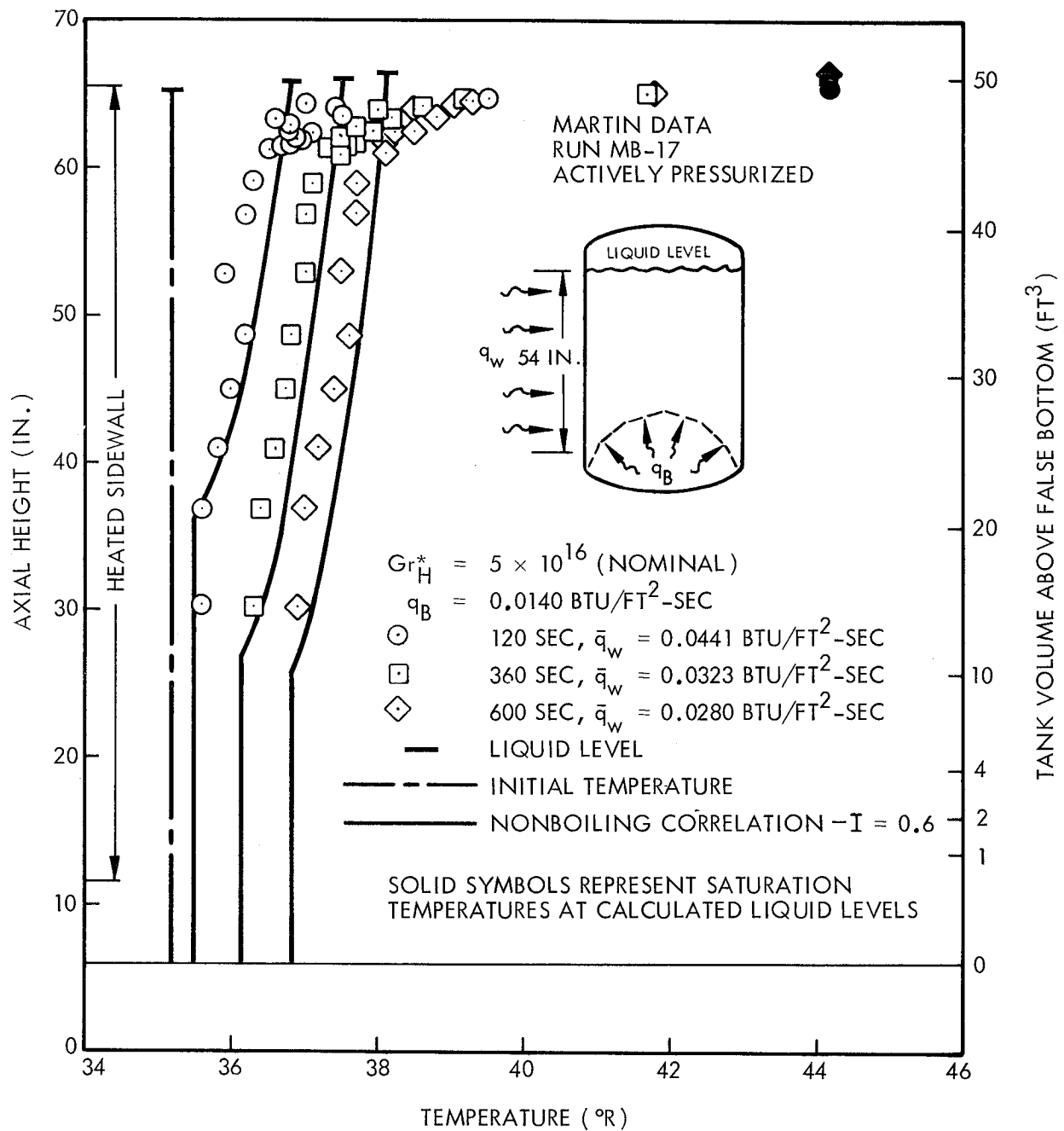
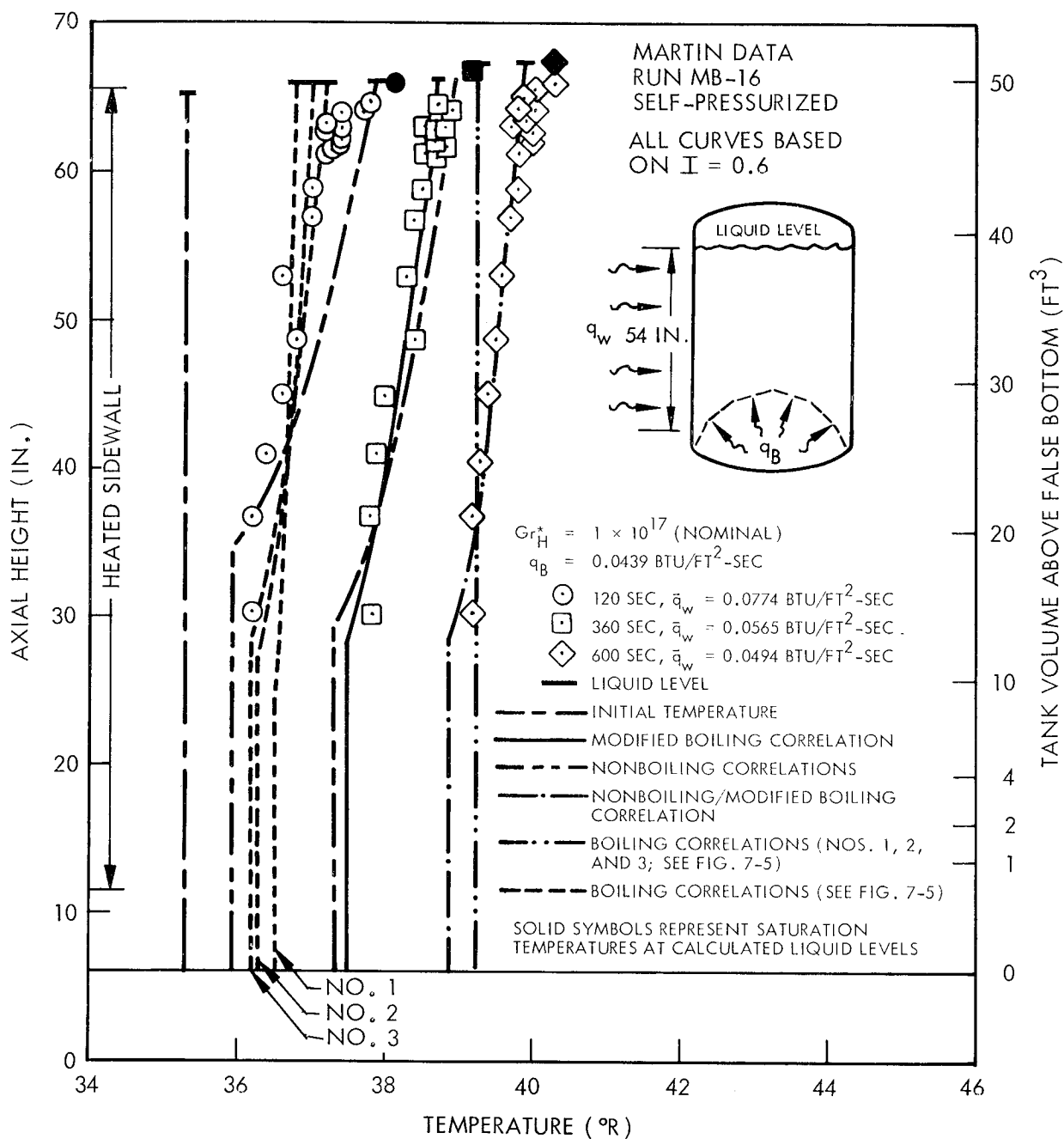Fig. 7-23 Temperature Stratification Correlation for Liquid Hydrogen —
Bottom Heating

7-49

Fig. 7-24 Temperature Stratification Correlation for Liquid Hydrogen—
Bottom Heating

7-50

Section 8

CONCLUSIONS

It has been shown that the integral technique analysis for predicting stratification, developed in Phase I of the study for uniform sidewall heating boundary conditions, can be extended to combined uniform sidewall and bottom heating boundary conditions as well as to asymmetric sidewall heating conditions with or without bottom heating.

Of the two models proposed for stratification with bottom heating, the experimental data obtained supported Model I which is based on the assumption that bottom heating does not influence liquid surface temperatures since the heat entering through the tank bottom is uniformly distributed below the thermal stratified layer. The experimental data also confirmed that the dimensionless temperature profiles in the thermal stratified layer are time-invariant, and that the values of the energy integral are in agreement, for modified Grashof numbers up to 10^{13}, with the correlation obtained from the data with uniform sidewall heating only. For modified Grashof numbers greater than 10^{13}, experimental stratification data with bottom heating indicated a value for the energy integral less than the value of 0.6 which was obtained without bottom heating.

With asymmetric sidewall heating, the measured temperature gradients in the stratified layer were found to be radially uniform in spite of the asymmetric boundary condition. Utilizing this fact and representing the sidewall heat flux boundary condition by equivalent finite sectors with uniform heat flux, the application of the integral technique resulted in predictions which were in very good agreement with the data, using values of the energy integral given by the correlation for uniform sidewall heating.

An analysis comparing the rate at which fluid from the boundary layer at the wall spreads near the liquid surface with the rate at which the stratified layer grows indicated that, even for large tanks, temperatures in the stratified layer would be radially uniform.

LOCKHEED MISSILES & SPACE COMPANY

The integral technique analysis for predicting stratification with asymmetric sidewall heating is therefore generally applicable.

The energy integral, which has been correlated as a function of modified Grashof number for a range from 10^8 to 10^{15}, has been shown to be independent of aspect ratio (liquid height to tank radius) in addition to being independent of Prandtl number.

The analytical model for liquid-ullage coupling, based on the integral technique stratification solution, is a promising approach to the problem of predicting stratification and ullage conditions for a liquid near saturation. This model will be fully evaluated with the results of an experimental program now in progress.

The solution obtained for a boiling free-convection boundary layer, which indicated an increased mass flow rate with boiling, was confirmed by experimental data. The increase in stratified layer growth with boiling predicted by the integral technique was also confirmed by experimental data.

The analysis of the cryogenic stratification data indicated uncertainties in the boundary conditions. Considering this limitation, good correlation of the experimental data was obtained with the integral technique analysis.

In actively pressurized tests, which provided the majority of the data, only a thin layer of liquid at the surface is affected by energy transfer with the ullage.

For actively pressurized tests with sufficient subcooling to suppress nucleate boiling in the free-convection boundary layer below the stratified layer, the data obtained were correlated quite well with energy integral values of 0.6 or 0.7 when the bottom heat flux was less than the sidewall heat flux. When the bottom heat flux was equal to or greater than the sidewall heat flux, good correlation was obtained with energy integral values of 0.4.

For actively pressurized tests with nucleate boiling in the free-convection boundary layer below the stratified layer, and in which the bottom heat flux was less than the

sidewall heat flux, the modified application of the boiling boundary layer analysis to the integral analysis provided good correlation of the data with energy integral values of 0.6.

If the maximum liquid temperature is limited by the constant ullage pressure in actively pressurized tests, the energy integral increases with time and approaches unity.

Only limited data were available for stratification under self-pressurizing conditions. Inconsistencies in these data prevent any general conclusions.

A single nucleate boiling heat-transfer coefficient correlation for LH_2 could not be selected on the basis of the available data. It appears that the inception of subcooled nucleate boiling occurs in a range of 1° to 3°F of superheat at the wall. The survey of data on subcooled nucleate boiling in LH_2 has indicated that experimental studies are required to determine more closely the inception point for bubble formation, the void fraction in the boundary layer, and the motion and collapse of the bubbles in the boundary layer. These factors are important in applying the boiling boundary-layer analysis to the prediction of stratification.

Section 9

REFERENCES

1. Lockheed Missiles & Space Company, <u>Analytical and Experimental Study of Liquid Orientation and Stratification in Standard and Reduced Gravity Fields</u>, 2-05-64-1, Sunnyvale, Calif., Jul 1964, (Contract NAS 8-11525)

2. -----, <u>Spreading of Liquids at Free Surface Supported by Buoyancy Forces</u>, by J. H. Chin, TIAD 524, Nov 1962

3. -----, <u>Theoretical and Experimental Studies of Zero-G Heat Transfer Modes</u>, Monthly Progress Report for the Period 1 September 1963 to 29 September 1963, Contract NAS 8-11525, Sunnyvale, Calif., 8 Oct 1963

4. -----, <u>Theoretical and Experimental Studies of Zero-G Heat Transfer Modes</u>, Monthly Progress Report for the Period 1 December 1963 to 29 December 1963, Contract NAS 8-11525, Sunnyvale, Calif., 7 Jan 1964

5. -----, <u>Theoretical and Experimental Studies of Zero-G Heat Transfer Modes</u>, Monthly Progress Report for the Period 1 November 1964 to 29 November 1964, Contract NAS 8-11525, Sunnyvale, Calif., 4 Dec 1964

6. -----, <u>Theoretical and Experimental Studies of Zero-G Heat Transfer Modes</u>, Monthly Progress Report for the Period 2 May 1965 to 30 May 1965, Contract NAS 8-11525, Sunnyvale, Calif., 7 Jun 1965

7. National Advisory Committee on Aeronautics, <u>Analysis of Turbulent Free Convection Boundary Layer on Flat Plate</u>, by E. R. G. Eckert and T. W. Jackson, NACA Report 1015, 1951

8. E. M. Sparrow and J. L. Gregg, "Laminar Free Convection from a Vertical Plate with Uniform Surface Heat Flux," <u>Trans. ASME</u>, Vol. 78, Feb 1956, pp. 435-440

9.   W. Rohsenow, "A Method of Correlating Heat Transfer Data for Surface Boiling of Liquids," _Trans. ASME_, Vol. 74, Aug 1952, pp. 969-976

10. National Advisory Committee on Aeronautics, _Laminar Free Convection on a Vertical Plate with Prescribed Non-Uniform Wall Heat Flux or Prescribed Non-Uniform Wall Temperature_, by E. M. Sparrow, NACA TN 3508, Jul 1955

11. Lockheed Missiles & Space Company, _RIFT Cryogenics Fluid Flow, 40-Inch Tank Gross Flow Tests, Final Report_, Report No. NSP-63-79, 12 Jun 1963

12. Martin Company, _Analytical and Experimental Determination of Liquid Hydrogen Temperature Stratification, Final Report_, NASA-CR-63-5, Apr 1963

13. -----, _Study of Cryogenic Propellants Stratification Reduction_, Monthly Progress Report for November 1963, NASA-CR-63-187, Dec 1963

14. -----, _Study of Cryogenic Propellants Stratification Reduction_, Third Quarterly Progress Report, January through March 1964, NASA-CR-64-7 (Issue 4), Apr 1964

15. Lockheed Missiles & Space Company, _Theoretical and Experimental Studies of Zero-G Heat Transfer Modes_, Monthly Progress Report for the Period 28 February 1965 to 28 March 1965, Contract NAS 8-11525, Sunnyvale, Calif., 1 Apr 1965

16. Martin Company, _Study of Cryogenic Propellants Stratification Reduction_, Monthly Progress Report for January 1964, NASA-CR-64-7 (Issue 2), Feb 1964

17. C. R. Class, et al., _Pool Boiling Heat Transfer to a Cryogenic Liquid_, WADC TR-58-528, Oct 1958

18. L. Weil and A. Lacaze, "Echanges de Chaleur dans L'Hydrogène Bouillant Sous Pressions Atmosphérique," _Soc. Française de Phys., Procés-Verbaux et Res. des Commun._ No. 9, 1951, p. 890

19. D. E. Drayer and K. D. Timmerhaus, "An Experimental Investigation of the Individual Boiling and Condensing Heat-Transfer Coefficients for Hydrogen," _Advances in Cryogenic Engineering_, Vol. 7, 1962, p. 401

20. J. E. Sherley, "Nucleate Boiling Heat-Transfer Data for Liquid Hydrogen at Standard and Zero Gravity," <u>Advances in Cryogenic Engineering,</u> Vol. 8, 1963, p. 495

21. H. K. Forster and N. Zuber, "Dynamics of Vapor Bubbles and Boiling Heat Transfer," <u>AIChE J.</u>, Vol. 1, 1955, p. 531

22. M. J. McNelly, "A Correlation of Rates of Heat Transfer to Nucleate Boiling Liquids," <u>J. Imp. Coll. Chem. Eng. Soc.</u>, Vol. 7, 1953, p. 18

23. Lockheed Missiles & Space Company, <u>Theoretical and Experimental Studies of Zero-G Heat Transfer Modes</u>, Monthly Progress Report for the Period 31 January 1965 to 28 February 1965, Contract NAS 8-11525, Sunnyvale, Calif., 1 Mar 1965

24. J. D. Seader, W. S. Miller, and L. A. Kalvinskas, <u>Boiling Heat Transfer for Cryogenics</u>, NASA Contractor Report CR-243, Jun 1963

25. W. H. McAdams, <u>Heat Transmission</u>, 3rd Ed., New York, McGraw-Hill, 1954, p. 172